

# ABSTRACT

Title of the dissertation: **TOPOLOGICAL PHOTONICS  
AND EXPERIMENTAL TECHNIQUES  
IN QUANTUM OPTICS**

Venkata Vikram Orre  
Doctor of Philosophy, 2019

Proposal directed by: **Professor Mohammad Hafezi**  
Department of ECE

Topological photonics is the study of how the geometries and topologies of devices can be used to manipulate the behavior of photons. Many topological models exhibit edge states, a defining feature of these models, which travel around the perimeter of the lattice and are not affected by disorder. These edge states can help create scalable delay lines, quantum sources of light, and lasers all of which are robust against fabrication-induced disorder and bends in photonic structures. This research proposal is structured into two parts.

In the first half of this thesis, we investigate a topological model and study some of its quantum applications. First, we realize the anomalous quantum Hall effect in a photonic platform using a 2D array of ring resonators with zero flux threading the lattice. The lattice implements a Haldane model by using the next-nearest couplings in lattice to simulate a nonzero local gauge flux while having a net flux of zero. The lattice hosts edge states, which are imaged through a CCD camera and show robustness against missing site-defects,  $90^\circ$  bends and fabrication-induced

disorder. We also demonstrate a topological non-trivial to trivial phase transition by simply detuning the ring resonances. Next, we show degenerate photon pair creation in an anomalous quantum Hall device using a dual-pump spontaneous four-wave mixing process. The linear dispersion in the edge band results in an efficient phase matching and shows up as maximum counts in spectral correlations. The flatness of edge band also allows us to tune the bandwidth of the quantum source by changing the pump frequencies. Furthermore, we verify the indistinguishability of the photons using a Hong-Ou-Mandel (HOM) experiment. Finally, we simulate the transport of time-bin entangled photons in an integer quantum Hall device. The edge states preserve the temporal correlations and are robust against fabrication-induced disorder. In contrast, the bulk states in the device exhibit localization, which is manifested in bunching/anti-bunching behavior.

In the second part, we explore a few experimental quantum optics techniques developed as a part of investigating quantum transport in topological devices. We demonstrate two experimental techniques:

1. We use an EOM-based time-lens technique to resolve temporal correlations of time-bin entangled photons, which would have been otherwise inaccessible due to the limited temporal resolution of single photon detectors. Our time-lens also maps temporal correlations to spectral correlations and provides a way of manipulating frequency-bin entangled photons.
2. We show frequency-resolved interference of two and three photons distinguishable in time, which would not have interfered in a standard Hong-Ou-Mandel (HOM) setup. Our setup can be extended to implement temporal boson sampling using

phase modulators. Furthermore, we demonstrate time-reversed HOM-like interference using time-bin entangled photon pairs and show that the spectral correlations are sensitive to phase between photons.

Lastly, we demonstrate some miscellaneous experimental techniques, such as the design of the electronics used for time-lens, optimal spontaneous parametric down conversion parameters, measuring joint spectral intensity using a chirped bragg grating, and simultaneous measurement of Hong-Ou-Mandel interference for different frequencies.

# TOPOLOGICAL PHOTONICS AND EXPERIMENTAL TECHNIQUES IN QUANTUM OPTICS

by

Venkata Vikram Orre

Dissertation submitted to the Faculty of the Graduate School of the  
University of Maryland, College Park in partial fulfillment  
of the requirements for the degree of  
Doctor of Philosophy  
2019

Advisory Committee:

Professor Mohammad Hafezi, Chair/Advisor

Professor Thomas Murphy

Professor Steven Anlage

Professor Thomas Antonsen

Professor Yanne K. Chembo



© Copyright by  
Venkata Vikram Orre  
2019

Dedicated to Adria.

## Acknowledgments

This dissertation would not have been possible without the support of many individuals. I want to thank my advisor, Prof. Mohammad Hafezi, for taking me on as a student and providing endless support throughout this process. This included both academic advising, as well as research directions and financial support. Mohammad has always been a kind advisor and I count myself lucky to have had his guidance. I especially want to thank him for his patience with me over the last 5 years.

I would also like thank Dr. Sunil Mittal, who I worked with day-to-day in the lab. From writing to understanding basic physics concepts, I owe the knowledge I have gained through this process to Sunil. He taught me how to operate optical instruments, machining, develop interfaces using NI Labview, and debug issues. Thank you Sunil for taking the time to teach me countless skills.

Dr. Alessandro Restelli also deserves thanks for helping me design and understand the electronics used in our experiments. I would also like to thank Dr. Elizabeth Goldschmidt for her helpful discussions and troubleshooting experimental problems.

For the completion of this dissertation, I would also like to thank the other members of my committee: Professor Thomas Murphy, Professor Steven Anlage, Professor Thomas Antonsen, and Professor Yanne K. Chembo. I appreciate their valuable time and feedback in this final stage.

The staff at JQI, ECE, and IREAP were also helpful in providing administra-

tive support.

I also appreciate my friends at JQI: Natalya and Dima, Swarnav, Long, Sarthak, Monica, Beth, Bin and many others for their friendship and for sharing their food and company with me at our many potlucks over the years. I also want to give a special shout-out to my friends still living in India who I continue to keep in touch with.

Finally, I want to thank my family for their support. My partner, Adria, has been a driving force in completing my Ph.D. Without her, this thesis would not have been possible. She made sure that I was on track and did not give up. I would especially like to thank her for providing company both while I was working on weekends and during our many adventures.

To everyone not mentioned here, thank you!

## Previously Published Work

Some of the research leading to this thesis has appeared previously in the following publications.

Parts of Chapter 2 have appeared in:

“Photonic Anomalous Quantum Hall Effect”, Sunil Mittal, Venkata Vikram Orre, Daniel Leykam, YD Chong, and Mohammad Hafezi, *Phys. Rev. Lett.*, **123**, 043201 (2019).

Parts of Chapter 3 have appeared in:

“Tunable quantum interference using a topological source of indistinguishable photon pairs”, Venkata Vikram Orre\*, Sunil Mittal\*, Elizabeth Goldschmidt and Mohammad Hafezi, *Manuscript in progress* (2020).

Parts of Chapter 4 have appeared in:

“Topologically robust transport of entangled photons in a 2D photonic system”, Sunil Mittal, Venkata Vikram Orre, and Mohammad Hafezi, *Optics Express*, **24**, 15631–15641 (2016).

Parts of Chapter 5 have appeared in:

“Temporal and spectral manipulations of correlated photons using a time lens”, Sunil Mittal, Venkata Vikram Orre, Alessandro Restelli, Reza Salem, Elizabeth Goldschmidt and Mohammad Hafezi, *Phys. Rev. A*, **4**, 043807 (2017).

Parts of Chapter 6 have appeared in:

“Interference of Temporally Distinguishable Photons Using Frequency-Resolved Detection ”, Venkata Vikram Orre, Elizabeth Goldschmidt, Mohammad Hafezi, and Sunil Mittal, *Phys. Rev. Lett.*, **123**, 123603 (2019).

# Contents

<i>Previously Published Work</i> . . . . .	v
<i>List of Figures</i> . . . . .	ix
<i>List of Abbreviations</i> . . . . .	x
1. <i>Introduction</i> . . . . .	1
1.1 Motivation . . . . .	1
1.2 Summary of Work . . . . .	3
2. <i>Anomalous Quantum Hall Effect</i> . . . . .	6
2.1 Introduction . . . . .	6
2.2 Ring resonator . . . . .	7
2.3 Theory of Anomalous Hall effect . . . . .	8
2.4 Device . . . . .	9
2.5 Edge states . . . . .	11
2.6 Trivial System . . . . .	13
2.7 Topological trivial and non-trivial boundary . . . . .	15
2.8 Summary . . . . .	16
3. <i>Tunable quantum interference using a topological source of indistinguishable photon pairs</i> . . . . .	18
3.1 Introduction . . . . .	18
3.2 Theory of dual-pump SFWM . . . . .	20
3.3 Experimental Setup . . . . .	24
3.4 Characterisation of the quantum source . . . . .	26
3.5 Spectral Correlations in an Anomalous Hall Device . . . . .	27
3.6 HOM experiment . . . . .	29
3.7 Energy-time entanglement . . . . .	33
3.8 Comparison with 1D CROW devices . . . . .	35
3.9 Summary . . . . .	40
4. <i>Two-photon transport in the quantum Hall systems</i> . . . . .	41
4.1 Introduction . . . . .	41
4.2 Qubits . . . . .	41
4.3 Entanglement . . . . .	43

4.4	Integer Quantum Hall Effect . . . . .	45
4.5	Theory of entangled photons in the 2D lattice . . . . .	47
4.6	Simulation Results of transport properties . . . . .	49
4.7	Transport in presence of disorder . . . . .	52
4.8	Summary and experimental Progress . . . . .	54
5.	<i>Temporal and Spectral manipulation of correlated photons using Time-lens</i> . . . . .	56
5.1	Introduction . . . . .	56
5.2	Time-lens setup . . . . .	57
5.3	Temporal Magnification of photons . . . . .	61
5.4	Temporal Correlations of photons . . . . .	62
5.5	Spectral Correlation Measurements . . . . .	66
5.6	Coherence of Time-lens . . . . .	66
5.7	Summary . . . . .	69
6.	<i>Interference of temporally distinguishable photons using frequency-resolved detection</i> . . . . .	70
6.1	Introduction . . . . .	70
6.2	Two-photon frequency-resolved detection . . . . .	72
6.2.1	JSI and Pulse-width of generated photons . . . . .	75
6.2.2	Two-photon Frequency-resolved Interference Results . . . . .	76
6.2.3	Fringe Visibility . . . . .	78
6.3	Three-photon frequency-resolved detection . . . . .	79
6.3.1	Three-photon Frequency-resolved Interference Results . . . . .	79
6.3.2	Reduced three-photon interference . . . . .	82
6.3.3	Miscellaneous probability contributions in three-photon interference . . . . .	85
6.3.4	Photon generation rates . . . . .	86
6.4	Entangled two-photon Frequency resolved detection . . . . .	86
6.4.1	Generation of polarization and time-bin entangled photons . . . . .	88
6.4.2	Entangled photons Frequency-resolved Interference Results . . . . .	90
6.5	Summary . . . . .	91
7.	<i>Miscellaneous Experimental Techniques</i> . . . . .	93
7.1	Signal Recovery and Amplifier for Time-lens . . . . .	93
7.1.1	Introduction . . . . .	93
7.1.2	Setup . . . . .	94
7.1.3	Signal Recovery Board . . . . .	97
7.1.4	Amplifier . . . . .	99
7.1.5	Labview Control . . . . .	102
7.2	Spontaneous Parametric Down conversion Photon Pair Generation in a non-linear crystal . . . . .	104
7.2.1	Theory of Spontaneous Parametric Down conversion . . . . .	104
7.2.2	Design Parameters . . . . .	105
7.3	Joint Spectral Intensity measurement using a chirped bragg grating . . . . .	107

7.4 Simultaneous measurement of Hong-Ou-Mandel dip for different frequencies . . . . .	109
8. <i>Conclusions and Outlook</i> . . . . .	112
8.1 Temporal Boson Sampling . . . . .	114
8.2 Two-photon experiment in Topological Devices . . . . .	115
<i>Appendix A. Device parameters</i> . . . . .	117
<i>Appendix B. Simulation of delay and transmission spectra in an anomalous Hall device</i> . . . . .	120
<i>Appendix C. Arduino code for Teensy operation</i> . . . . .	124



## List of Figures

2.1	Schematic of an anomalous quantum Hall device using ring resonators	10
2.2	Imaging and Transmission of topologically non-trivial lattice . . . . .	12
2.3	Imaging and Transmission of topologically trivial lattice . . . . .	14
2.4	Topological trivial and non-trivial boundary . . . . .	17
3.1	Experimental setup of DP-SFWM . . . . .	21
3.2	Quantum source characterisation . . . . .	25
3.3	Measured JSI of signal photons on an anomalous Hall device . . . . .	28
3.4	HOM in an anomalous Hall device . . . . .	30
3.5	Franson Interferometer . . . . .	34
3.6	Transmission and delay spectra in anomalous Hall vs 1D CROW devices	36
3.7	Comparison of spectral correlations in anomalous Hall vs 1D CROW devices . . . . .	37
3.8	(a-b,c-d) Transmission and output spectrum of two different anomalous Hall devices. Insets show corresponding JSI's when the pumps are excited at $[\omega_{p_1} - \omega_{0p_1}, \omega_{p_2} - \omega_{0p_2}] = [0J, 0J], [0.8J, 0J], [0.8J, 0.8J]$ .	38
3.9	(a-b) Transmission and output spectrum of a 1D CROW device. Insets show JSI's when the pumps are excited at $[\omega_{p_1} - \omega_{0p_1}, \omega_{p_2} - \omega_{0p_2}] = [0J, 0J], [0.8J, 0J], [0.8J, 0.8J]$ . . . . .	39
4.1	Time-bin qubit setup . . . . .	43
4.2	Structure of IQHE device. . . . .	46
4.3	Temporal Correlations after transport through the edge bands . . . . .	50
4.4	Temporal Correlations after transport through the bulk band . . . . .	51
4.5	Temporal Correlations in presence of disorder . . . . .	53
4.6	Probability of bunching and Similarity in presence of disorder . . . . .	55
5.1	Experimental setup of time-lens . . . . .	58
5.2	Output delays as a function of input delays . . . . .	60
5.3	Temporal correlations with and without the time-lens . . . . .	63
5.4	Spectral correlations after the time-lens . . . . .	67
5.5	Coherence of the time-lens . . . . .	68
6.1	Experimental setup to observe two-photon frequency-resolved interference . . . . .	73
6.2	Characterization of the input photons . . . . .	74
6.3	Two-photon spectral correlations as a function of delay . . . . .	77

6.4	CAR correlations and corresponding fringe separation . . . . .	79
6.5	Experimental setup and Three-photon frequency-resolved correlations . . . . .	81
6.6	Integrated three-photon correlation function . . . . .	84
6.7	Three-photon correlations with and without miscellaneous probabil- ity terms . . . . .	86
6.8	Photon generation rates . . . . .	87
6.9	Setup and results to verify entanglement . . . . .	89
6.10	Spectral correlations for time-bin entangled photon pairs . . . . .	90
7.1	Block diagram to generate RF wave . . . . .	94
7.2	Board diagram of signal recovery and amplifier . . . . .	96
7.3	Schematic of signal recovery PCB . . . . .	98
7.4	Schematic of Amplifier and pictures of the pcb's . . . . .	101
7.5	Schematic of driving circuits for Amplifier . . . . .	102
7.6	Labview Interface . . . . .	103
7.7	Simulated and Measured JSI for SPDC . . . . .	105
7.8	Experimental setup for SPDC . . . . .	106
7.9	Experimental setup to measure JSI . . . . .	108
7.10	Experimental setup and results for simultaneous measurement of HOM for different frequencies . . . . .	110
A.1	Schematic of silicon waveguide and anomalous Hall device . . . . .	118
B.1	Schematic of an anomalous Hall device . . . . .	121

## List of Abbreviations

1D	One-Dimensional
2D	Two-Dimensional
BJT	Bipolar Junction Transistor
BS	Beam-splitter
BPF	Bandpass Filter
CAR	Coincidences to Accidental Ratio
CBG	Chirped-Bragg Grating
CCD	Charge-Coupled Device
CCW	Counter Clockwise
CMOS	Complementary metal-oxide-semiconductor
CROW	Coupled-Resonator Optical Waveguide
CW	Clockwise
DP SFWM	Dual-Pump Spontaneous Four-Wave Mixing
EOM	Electro-Optic Modulator
EDFA	Erbium-Doped Fiber Amplifier
FWHM	Full-Width at Half-Maximum
GDD	Group Delay Dispersion
HOM	Hong-Ou-Mandel
HWP	Half-Wave Plate
H	Horizontally
IQHE	Integer Quantum Hall Effect
JSI	Joint Spectral Intensity
JTI	Joint Temporal Intensity
ND-SFWM	Non-degenerate Spontaneous Four-Wave Mixing
P-MOS	P-type Metal-Oxide-Semiconductor
PBS	Polarization Beam-splitter
PC	Polarization Controller

PCB	Printed Circuit Board
PD	Photo-diode
PLL	Phase-Locked Loop
PPKTP	Periodically-polled potassium titanyl phosphate
RF/rf	Radio Frequency
SFWM	Spontaneous Four-Wave Mixing
SOI	Silicon-On-Insulator
SPDC	Spontaneous Parametric Down-Conversion
SPI	Serial Peripheral Interface
SMBS	Spatial mode boson sampling
SNSPD	Super conducting Nanowire Single-Photon Detector
TCSPC	Time-Correlated Single Photon Counting
TE	Transverse Electric
TIA	Time Interval Analyzer
V	Vertically

## Chapter 1: Introduction

### *1.1 Motivation*

The discovery of integer quantum Hall effect forever changed the landscape of condensed matter systems [1]. The phenomena of quantized Hall conductance as a function of applied magnetic field was observed in a two-dimensional gas at low temperature and could not be explained by classical physics. This was surprising, since the impurity of samples and other interactions should effect the conductance. The origin for the quantization was later explained by the presence of Landau levels and the quantization value was the result of the current travelling through robust unidirectional chiral edge states [2, 3]. The conduction in the Landau levels filled below the fermi level contributed to the integer in the quantization value and was also shown to be related to the topological invariance of the system [3]. These edge states were unidirectional, immune to disorder induced localization, and hence were not affected by any local effects in the system such as impurities.

It took nearly two decades to realize the first experimental demonstration of quantum Hall effect in photonics using a magneto-optical photonic crystal in the microwave regime [4]. However, this implementation in the optical domain was difficult due to lack of strong magneto-optical response materials. The proposed

solution [5–8] instead, is to have photons experience an artificial/synthetic magnetic field. The first of such experiments were performed in [9, 10], which demonstrated the presence of edge states in the system. Since then, many experiments have shown edge states using various photonic systems [11–13].

There is a growing demand for on-chip integrated photonic technologies for use in commercial applications such as routing, sensing and quantum communications. However, fabrication disorder affects the photonic devices and hinders their scalability. For example, an array of ring resonators designed to act as a broadband flat filter would have bands with peaks and troughs varying from device to device, due to disorder. By using the robustness of these topological edge states, one can create scalable devices which are robust to fabrication disorder. The motivation for our research is explore how these topological devices could potentially be used for quantum communications and quantum information.

Our topological system consists of an 2D array coupled ring resonators where the synthetic magnetic field is simulated by controlling the hopping phase and coupling between the site rings. The site rings are connected using link rings which are frequency detuned by a phase  $\pi$  from the site rings. The link rings effectively as waveguides between sites and are used to control the hopping strength and phase between the photons. The devices are fabricated using silicon-on-insulator (SOI) platform which could be produced in existing commercial CMOS foundries. Integer quantum Hall effect (IQHE) has already been demonstrated in this platform and the corresponding edge states were shown to be robust against disorder [9, 14]. In this thesis, we use the same architecture to implement another topological model,

anomalous Hall effect, and study two applications such as creating a robust tunable quantum light source and using the edge states for quantum communications. As a part of this, we developed two experimental techniques—time-lens and frequency-resolved detection—which could be useful in the field of quantum optics and quantum communications.

## 1.2 *Summary of Work*

In Chapter 2, we realize a photonic analogue of anomalous Hall effect with 2D array of ring resonators by exploiting the next-nearest couplings in the lattice. We image the edge states in the system using a charge-coupled device (CCD) camera and show that they are robust against  $90^\circ$  bends, missing site-defects and fabrication-induced disorder. Unlike the IQHE device, the anomalous device is translationally invariant and hence a topological transition can be induced by simply detuning the site rings. We show a topologically trivial to non-trivial transition by detuning the rings. This design could potentially be used to make robust reconfigurable photonic devices in areas of routing and switching.

In Chapter 3, we use the anomalous Hall device to produce degenerate photon pairs using dual-pump spontaneous four-wave mixing (DP SFWM). We show that the linear dispersion of the edge states provides an efficient phase matching condition for DP SFWM and produces maximum spectral correlations in the edge band. The linear dispersion also make it possible to tune the bandwidth of the generated photons by changing the pump frequencies. Finally, we verify the indistinguishability of

photons using Hong-Ou-Mandel (HOM) experiment. This work allows exploration of a robust tunable quantum sources on-chip which would be helpful in many applications of quantum information such as coupling light to various optical cavities.

In Chapter 4, we simulate and study the transport of time-bin entangled photons in a IQHE device. We observe that the temporal correlations are preserved when they travel through edge states, where as bulk states exhibit localization and distort the temporal correlations. This work suggests that edge states can be used for quantum communications. During the exploration of this experiment using our devices, we develop two quantum optical techniques which are described below.

In Chapter 5, we realize an electro-optic modulator (EOM) based time-lens technique to resolve temporal and spectral correlations of time-bin entangled photons. The single photon detectors used to detect temporal correlations have a finite jitter and cannot resolve correlations if the photons are separated by less than the detector jitter. We use a time-lens technique to resolve the photons and their temporal correlations for separations of less than detector jitter by magnifying the time by a factor of  $\approx 9.6$ . Furthermore, the generated photons map the temporal correlations to spectral correlations and could be used to manipulate frequency-bin entangled photons. This technique could enable resolving picosecond time scales using existing single photon detectors for use in quantum communications.

In Chapter 6, we realize frequency-resolved interference of two and three photons distinguishable in time. In interference experiments like HOM, any distinguishability between photons wipes out the interference. Using frequency-resolved detection, we show interference between photons which are separated by more than



50 times their pulsewidth. Furthermore, we demonstrate time-reversed HOM-like interference using time-bin entangled photon pairs and show that the spectral correlations are sensitive to the phase between photons. By adding a time-dependent dispersion/phase modulator, our experimental setup can be extended to perform boson sampling in time, which is one of the benchmarks to achieve quantum supremacy.

In Chapter 7, we put together some experimental techniques, such as design of the printed circuit board used in time-lens, optimal SPDC parameters, joint spectral intensity measurement using a chirped bragg grating, and simultaneous measurement of HOM dip for different frequencies.

In Chapter 8, we conclude the thesis and discuss potential future work.

## Chapter 2: Anomalous Quantum Hall Effect

### 2.1 Introduction

Topological photonics have been shown to produce edge states which are robust against disorder. A few possible applications of these edge states include creation of delay lines [5,9,14], lasers [15–17], quantum sources of light [18,19] and reconfigurable pathways on chips [20,21]—all of which are robust against fabrication-induced disorder and bends in the photonic structures. Despite many advances in photonics, there has not yet been a nanophotonic realization of the anomalous quantum Hall phase—a two-dimensional Chern insulator with zero net gauge flux [22,23]. In this chapter, we demonstrate a nanophotonic analogue of the anomalous quantum Hall system using a periodic 2D checkerboard lattice of coupled ring resonators with nearest and next-nearest neighbor couplings [24].

As proposed in Ref. [25], the tight-binding description of the photonic lattice is similar to the Haldane model [22], in that the net gauge flux threading the lattice is zero, but next-nearest neighbor couplings induce non-zero local gauge flux. This effectively breaks time reversal symmetry and creates a topologically nontrivial band gap. We directly image the light intensity distribution in the lattice, revealing topological edge states in this gap that are robust against missing-site defects and

propagate around  $90^\circ$  corners without any scattering into the bulk. Because the overall structure is time-reversal invariant, it hosts a pseudospin degree of freedom associated with the clockwise and the counter-clockwise (time-reversed) propagation of photons in the rings. By selective excitation of the pseudospins, we show that time-reversal invariance is effectively broken within each decoupled pseudospin sector, similar to the Kane-Mele quantum spin Hall model with no Rashba coupling [23], and the edge states associated with the two pseudospins propagate in opposite directions. Furthermore, we demonstrate a transition between topologically nontrivial and trivial phases by detuning the ring resonance frequencies, and observe edge states at an internal boundary between the two phases. We note that the system is periodic and does not require staggering the phases of the couplings, unlike the coupled-resonator system of Refs. [5,9,17] which realizes the integer quantum Hall effect.

## 2.2 *Ring resonator*

A ring resonator is a looped waveguide which resonates similar to an optical cavity. When a field goes through  $n$  times round the ring, it constructively/destructively interferes at specific wavelengths. The resonance condition happens when  $n\lambda = L$ , where  $n$  is an integer,  $\lambda$  is resonant wavelength and  $L$  is the length of the ring. The light in the ring could be coupled in two modes; one propagating clockwise and the other counter clockwise. These two modes could be considered as a pseudospin in integer quantum Hall effect (IQHE) and anomalous quantum Hall

effect system. There exists many longitudinal modes in the resonator, but we design the system such that single-mode approximation theory would be valid in a given free spectral range (FSR). This is done by making the bandwidth much smaller than the FSR, i.e using high quality factor (Q) rings.

### 2.3 *Theory of Anomalous Hall effect*

We construct a 2D array of ring resonators and realize photonic analogue of anomalous Hall effect. Our system consists of superposed square lattice of two different sets of site rings **A** and **B** as shown in Fig. 2.1. The site-rings are coupled to their neighbours and next-nearest neighbours using link rings which are detuned from the site rings by a phase difference of  $\pi$ . The detuning is accomplished by introducing an extra path-length into the link rings. The link rings introduces a direction-dependent hopping phase  $\pm\pi/4$  when photons hop between neighbours and, a phase of zero between next-nearest neighbours. This configuration results in a effective magnetic flux  $\pi$  threading a plaquette (containing two **A** and two **B**) and a net magnetic flux of zero in an unit cell (two plaquettes). This system breaks time-reversal symmetry and gives rises to an anomalous quantum Hall phase without Landau levels [22]. The two modes of clockwise and counter-wise modes in the lattice contribute to pseudospin(up and down) degree of freedom. The two modes realize two different copies of anomalous Hall phase. Since their hopping phases are  $+\pi/4$  and  $-\pi/4$ , the lattice breaks time-reversal symmetry and behaves similar to Kane-Mele model of quantum spin Hall effect [23].

The corresponding hamiltonian for the system is

$$\begin{aligned}
H = & \sum_{\langle i,j \rangle, \sigma} (\omega_0 - M) a_{i,\sigma}^\dagger a_{i,\sigma} + (\omega_0 + M) b_{i,\sigma}^\dagger b_{i,\sigma} \\
& - J \left( a_{j,\sigma}^\dagger a_{i,\sigma} + b_{j,\sigma}^\dagger b_{i,\sigma} + a_{j,\sigma}^\dagger b_{i,\sigma} e^{-i\sigma\phi_{i,j}} + \text{h.c.} \right), \quad (2.1)
\end{aligned}$$

Here,  $a_{i,\sigma}$  and  $b_{i,\sigma}$  are the annihilation operators corresponding to site rings **A** and **B**, respectively, at lattice site index  $i = (x, y)$  and the summation  $\langle i, j \rangle$  is only over nearest and next-nearest neighbours.  $\sigma = \pm 1$  is the pseudospin index for the up/down spins, respectively.  $J$  is the coupling strength between nearest and the next-nearest neighbor sites, and  $\phi_{i,j} = \pm\pi/4$  is the direction-dependent hopping phase between sites **A** and **B**, as shown in Fig. 2.1(a). We introduce a detuning  $M$  between the **A** and **B** site rings. If  $M < 2J$ , the lattice exhibits a robust unidirectional topological edge state in the topological bandgap (Fig. 2.1(c)). In contrast, when  $M > 2J$ , the lattice is topologically trivial and doesn't exhibit any edge states.

## 2.4 Device

We use the silicon-on-insulator (SOI) platform and fabricate the chip using deep-UV projection lithography at a commercial foundry (IMEC, Belgium). Each resonator has a width of 510 nm and 220 nm in height and is designed such that only a single transverse electric (TE) mode propagates through it. The interaction length and gap between the rings determines the coupling between rings. The coupling gap between the rings is designed such that  $J$  is estimated to be 15.6(4) GHz. More specifications on the devices are given in Appendix A. Surface roughness of the

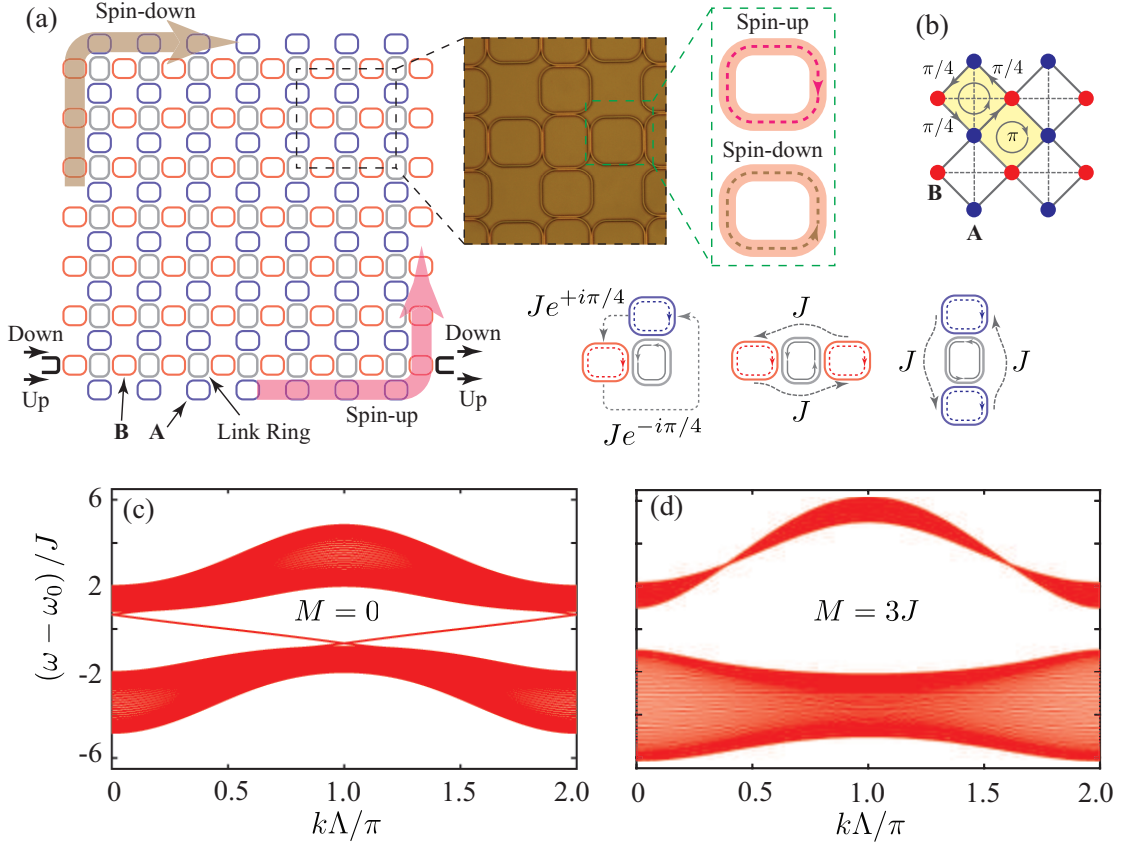


Fig. 2.1: (a) Schematic of the 2D array of ring resonators, with site-rings **A**(blue) and **B**(red) coupled using link-rings (grey). Top-left inset: microscope image of the device. Top-right inset: the two pseudospin degree of freedom, up and down, which correspond to the clockwise and the counterclockwise circulation of photons in the site rings, respectively. Center inset: schematics for nearest-neighbor hopping (left) and next-nearest-neighbor hoppings (center and right) for the pseudospin-up. (b) Schematic of the 2D lattice. Red and blue circles indicate **A** and **B** lattice sites respectively. Solid lines denote nearest-neighbor hoppings between **A** and **B** sites, with hopping phases indicated. Dashes indicate next-nearest neighbor hoppings. The gauge flux is  $\pm\pi$  in a single plaquette, and zero over a unit cell of 2 plaquettes (shaded yellow). (c)-(d) Band diagram of the semi-infinite lattice for  $M = 0$  and  $M = 3J$ , respectively.

waveguides will allow for some light to leak through which is captured through a charged-coupled device (CCD) camera. Light from a continuous wave laser is amplified through a Erbium-doped fiber amplifier (EDFA) and sent through the input port and the corresponding power is detected at the drop port. From the image captured by the CCD camera, we determine the intensity distribution in each of the rings.

## 2.5 *Edge states*

We fabricated an array of 56 **A** and 56 **B** resonators as shown in schematic in Fig. 2.1(a). For this device,  $M = 0$  is chosen which implies that both **A** and **B** rings are identical. Fig. 2.2(a,c) show the simulated transmission spectrum for the pseudo-spin up and pseudo-spin down configuration. The procedure to simulate the spectra is given in Appendix B. We observe the transmission in pseudospin-down is lower as light travels a long path and encounters a higher loss. The simulations do not include disorder which changes the transmission spectrum from device to device. We measure the transmission spectrum for pseudospin-up excitation and observe a band with high transmission around  $\delta\nu \approx 0$  GHz Fig. 2.2(a). The central frequency is calculated by minimizing the variation in transmission and delay spectra in the edge band [9]. Fig. 2.2(b) shows measured spatial intensity over a range of 5 GHz. In Fig. 2.2(e), the light travels along the counter-clockwise direction and is confined to the edge. We also observe that the light travels around two sharp  $90^\circ$  bends without scattering into bulk. This is the edge band of the device. The

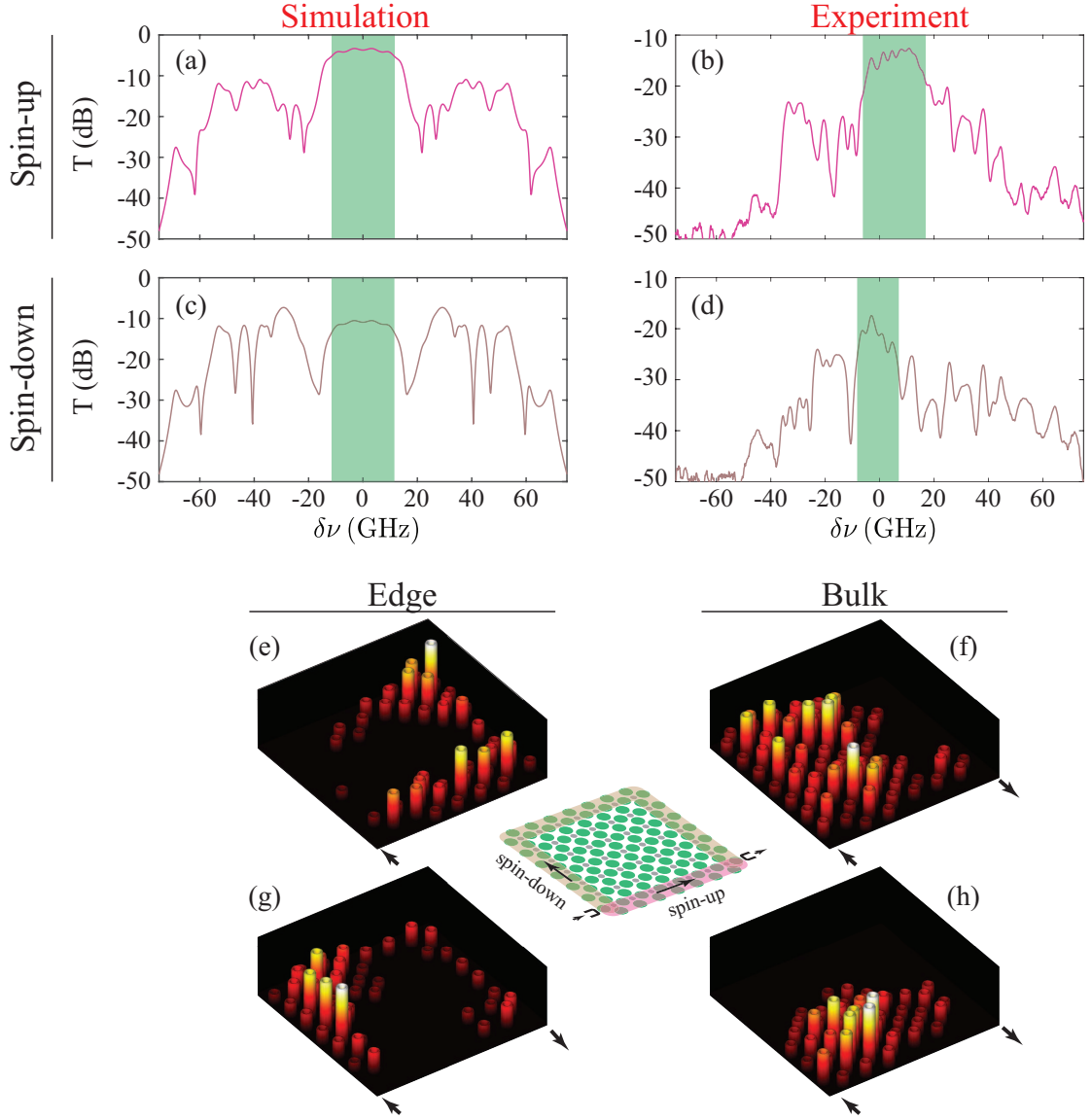


Fig. 2.2: (a-b) Measured and Simulated transmission ( $T$ ) spectrum for the topologically nontrivial lattice ( $M = 0$ ) with the pseudospin-up excitation. The green shaded region shows the band over which topological edge states are observed in direct imaging. (e) The corresponding spatial intensity distribution obtained through direct imaging at  $\delta\nu \approx 0$  (integrated over a frequency range of 5 GHz). (f) Intensity distribution at  $\delta\nu \approx -20$  GHz, showing scattering into the bulk. (c-d),(g-h) The corresponding results for the pseudospin-down excitation.



decrease in intensity along the edge is due to the scattering losses and attenuation in the waveguides. When contrasted with light excited at  $\delta\nu \approx 20$  GHz (away from the edge band), the intensity is distributed through the bulk of the lattice, as shown in Fig. 2.2(c). This is the bulk band of the lattice. The fabricated devices have a disorder of  $2J$  (33 GHz) which is comparable to the bandgap of the device. In spite of this disorder, the lattice exhibits clear edge states showing its robustness against fabrication-induced disorder.

Next, we study the spin-nature of topological edge state by exciting the pseudospin-down configuration. Fig. 2.2(d) shows the resulting transmission spectrum for pseudospin-down and the corresponding intensity distribution at  $\delta\nu \approx 0$  GHz shows a confined edge state travelling in clockwise direction. The transmission in this edge is about 5 dB lower compared to pseudospin-up, since it has to travel a longer path and hence undergoes more scattering loss. As before, exciting at  $\delta\nu \approx 20$  GHz shows light scattering into the bulk. We also observe that the transmission in the bulk is much lower compared to simulation which shows the effect of disorder on the bulk. We see a slight shift between edge band frequencies because pseudospin-up experiences a different disorder compared to pseudospin-down.

## 2.6 Trivial System

Unlike the IQHE device given in [9], the anomalous device is translationally invariant and hence a topological transition can be induced just by detuning the site rings. To show a topological phase transition, we engineer another device with a de-

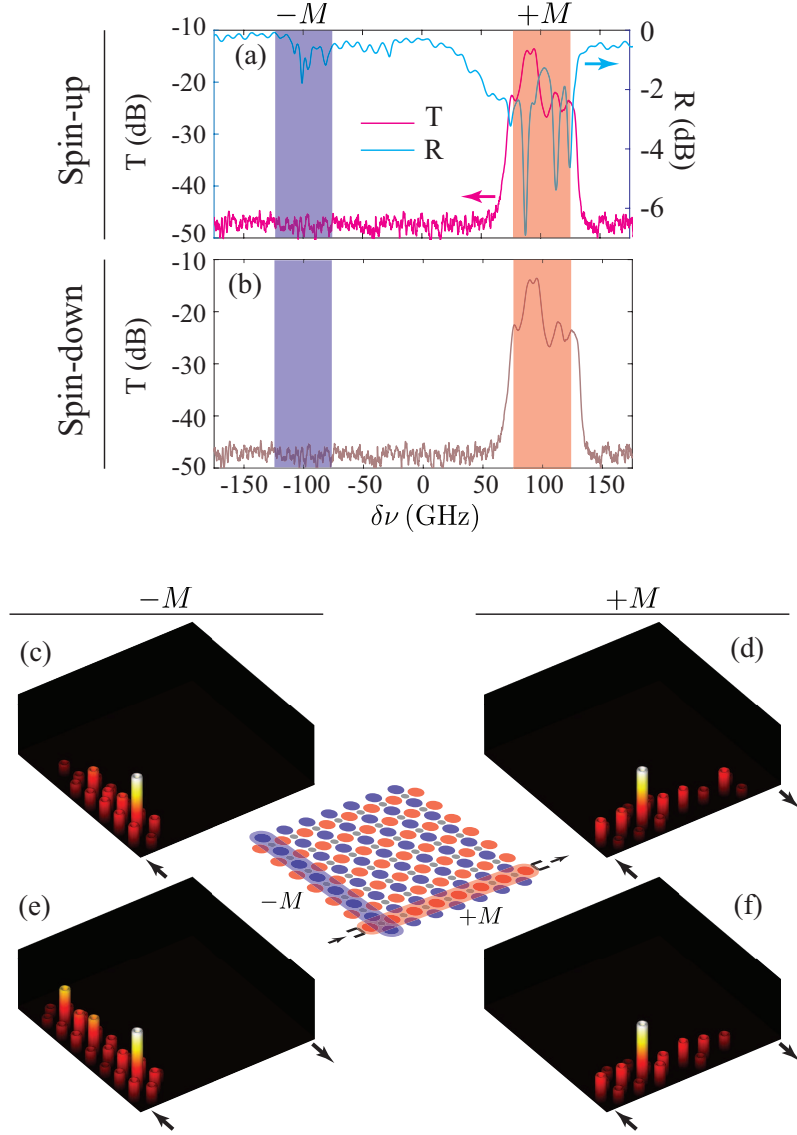


*Fig. 2.3:* (a) Measured transmission (T) and reflection (R) spectrum of a topologically trivial device, with  $M \approx 98 \text{ GHz} \gg 2J$  and pseudospin-up excitation. (c,d) Spatial intensity profiles for  $\delta\nu = +M$  and  $\delta\nu = -M$ , showing excitation of only **B** and **A** rings, respectively. (b) Measured transmission spectrum for the pseudospin-down excitation. (e,f) Spatial intensity distributions also remain almost identical, confirming topologically trivial nature of the lattice.

tuning of  $M > 2J = 98$  GHz. The detuning is achieved by increasing(/decreasing) the length of the site rings **A**(**B**) which effectively shifts the ring resonance frequencies. Fig. 2.3(a) shows the transmission for pseudospin-up and we see negligible transmission at  $\delta\nu \approx 0$  GHz indicating the presence of a bandgap. There is single transmission band at  $\delta\nu \approx M \approx 100$  GHz. The measured intensity distribution shows that a few **B** rings are excited at  $\delta\nu = 100$  GHz (Fig. 2.3(c)). The site **A** rings and **B** rings are weakly coupled due to resonance mismatch. Hence, the transmission at  $\delta\nu = 100$  GHz is negligible but the **A** rings can be seen to be excited from the intensity profile and the reflection spectra (Fig. 2.3(b)). Here, flipping the spin of excitation does not affect the transmission or the intensity profile confirming that lattice is topologically trivial (Fig. 2.3(d)).

## 2.7 Topological trivial and non-trivial boundary

In order to verify that edge states are not artifacts of physical boundary, we fabricated a device with interface between a topologically non-trivial ( $M = 0$  GHz) and a trivial ( $M \approx 98$  GHz) lattice as shown in Fig. 2.4(a). We place an input port on one edge of the non-trivial domain and two output ports at the edges of trivial and non-trivial domains. The measured transmission for two outports are shown in Fig. 2.4(b). At frequencies in the bandgap of the non-trivial domain, we see that the light travels along the clockwise edge of the non-trivial boundary without scattering into the trivial domain. We further see that there is no transmission in the trivial domain. To further test the robustness of edge states, a ring has been

removed along the edge of non-trivial domain as shown in Fig. 2.4(a) and (c). The edge states routes around the missing defect without scattering into bulk.

## 2.8 *Summary*

In this chapter, we have realized a photonic analogue of the anomalous quantum Hall phase using a 2D lattice of ring resonators with net zero flux. We showed that the system exhibits robust edge states that are less susceptible to fabrication-induced order. We also showed a topological non-trivial to trivial phase transition by introducing relative detuning between the site rings. This system could be modified to perform reconfiguration topological phase transitions using metal heaters or electro-optic modulators [26, 27]. This design could be potentially be used to make robust reconfigurable photonic devices in areas of routing and switching.

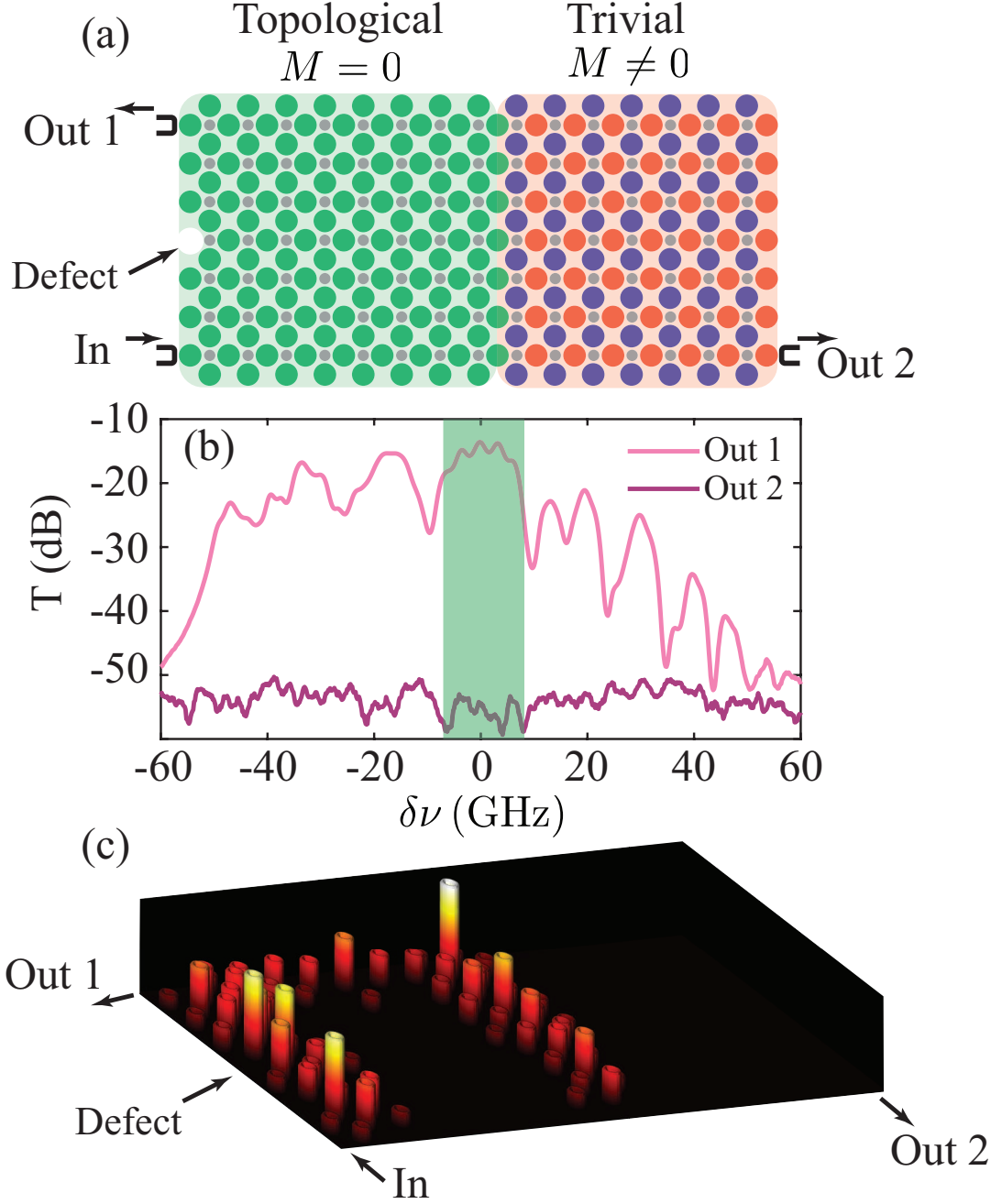


Fig. 2.4: (a) Schematic of device with an interface between topological ( $M = 0$ ) and trivial ( $M > 2J$ ) domains. The topological domain also hosts a defect in the form of a missing site-ring resonator. (b) Measured transmission ( $T$ ) spectrum from input to the two output ports, for the pseudospin-down excitation. (c) Measured spatial intensity profile.

## Chapter 3: Tunable quantum interference using a topological source of indistinguishable photon pairs

### 3.1 Introduction

Indistinguishable photon pairs and their quantum interference is a fundamental resource enabling many quantum applications such as quantum metrology [28, 29], quantum communications [30, 31] and quantum computing [32, 33]. Sources of indistinguishable photon pairs have largely relied on nonlinear processes, such as spontaneous parametric down conversion (SPDC) and spontaneous parametric four-wave mixing (SFWM), in bulk crystals or optical fibers. There is a growing need to generate these photon sources on-chip which can be accomplished by using the  $\chi^3$  non-linearity of silicon. On-chip photon pairs produced through SFWM have an added advantage over SPDC of being easily scalable and not requiring special materials. However, disorder during fabrication processes changes the device functionality and makes the scalability of these devices ineffective. One prominent solution to the problem is to use topological edge states, which were shown to be robust against fabrication-induced disorder. Recently, these edge states have been used to create a topological non-degenerate photon pair source using spontaneous

four-wave mixing in a quantum-spin Hall device [18] and other works [34, 35] have shown quantum interference in topological models. Furthermore, the correlations generated in parametric processes dictate the characteristics of quantum interference between generated photons, and subsequently, their applications in quantum networks and quantum communications [36, 37]. For example, long distance quantum communications and efficient atom (cavity)-photon interfaces require photons with narrow spectral bandwidths whereas quantum-enhanced temporal measurements may require photons with narrow temporal bandwidths [38–40]. This diverse range of applications necessitates generation of photon pairs with tunable spectral and temporal correlations.

In this chapter [19], we report the generation of indistinguishable photon pairs via dual-pump SFWM in a topological photonic system that simulates the anomalous-quantum Hall effect for photons [22, 24, 25]. More importantly, we use the linear dispersion and the spatial confinement of the topological edge states to generate photon pairs with tunable spectral bandwidth. Our system is time-reversal symmetric and supports two pseudo-spins with counter-propagating edge states, similar to the quantum-spin Hall effect. We use these two pseudospins, together with a Sagnac interferometer scheme, to generate path-entangled photon pairs, and subsequently, realize a deterministic quantum beam-splitter to separate the indistinguishable photon pairs via time-reversed HOM interference [41–43]. This allows us to confirm the indistinguishability of signal and idler photons using HOM interference. We also show that the tunability of the spectral bandwidth of the two-photon wavefunction manifests in the temporal width of the HOM interference dip. Next,

we demonstrate that the generated photon pairs are energy-time entangled, as expected for a SFWM process with continuous-wave pump. Finally, we compare the spectral correlations of multiple 2D devices with 1D array of ring resonators and show that the topologically non-trivial devices surpass the performance of topologically trivial devices to produce consistent output spectrum in the edge bands. Our results would pave the way for the realization of topologically robust quantum photonic devices, for example, topological parametric amplifiers and single-mode topologically squeezed light [44, 45].

### 3.2 Theory of dual-pump SFWM

In a dual-pump SFWM process (DP-SFWM), two pump photons  $\omega_{p_1}$  and  $\omega_{p_2}$  annihilate to produce two identical signal and idler photons  $\omega_s, \omega_i$  as shown in Fig. 3.1(a). The output spectrum of the generated signal photons is determined by the energy and momentum equations  $\omega_{p_1} + \omega_{p_2} = \omega_s + \omega_i$  and  $k_{p_1}(\omega_{p_1}) + k_{p_2}(\omega_{p_2}) = k_s(\omega_s) + k_i(\omega_i)$ . It can be seen that output spectrum also depends on the dispersion relation of the medium. By using the linear dispersion of the edge states, we can efficiently generate degenerate photon-pairs in a DP-SFWM process across the edge band.

We use the topological configuration of an anomalous Hall device in Chapter 2, where  $M = 0J$ . This configuration results in a Haldane-like tight-binding Hamiltonian [22, 24, 25],

$$H_L = \sum_{i,j} \omega_0 a_i^\dagger a_i - J \left( \sum_{\langle i,j \rangle} a_j^\dagger a_i e^{-i\phi_{i,j}} + \sum_{\ll i,j \gg} a_j^\dagger a_i + \text{h.c.} \right) \quad (3.1)$$



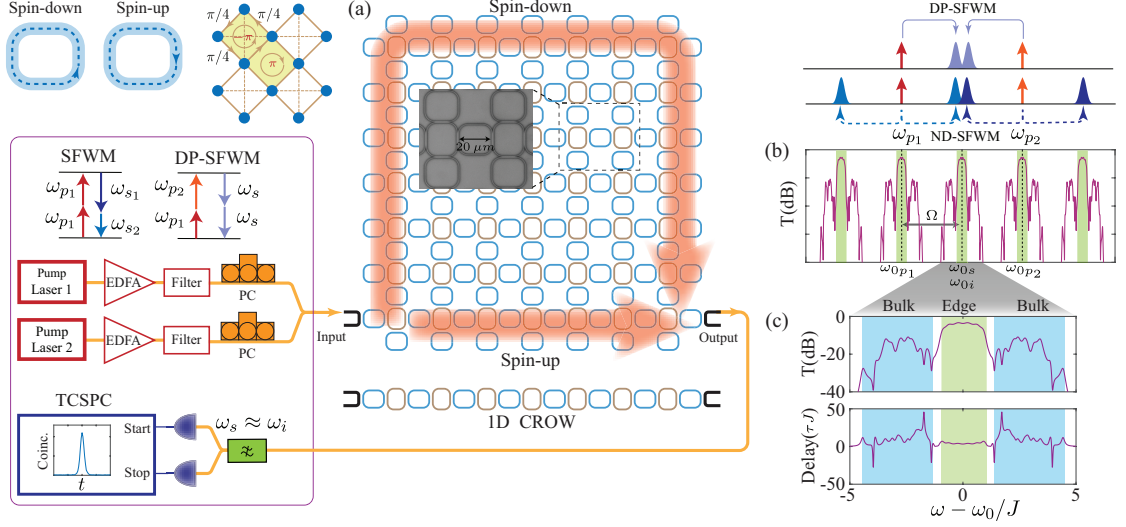


Fig. 3.1: (a) Experimental setup to perform DP-SFWM in an anomalous Hall device (b-c)

Simulated transmission and delay spectrum of device. We pump the lattice using two classical, continuous-wave pump beams in two longitudinal modes of the lattice ( $\omega_{p1}, \omega_{p2}$ ) separated by two free-spectral ranges (FSRs). The corresponding resonance frequencies of pumps, signal and idler are given by  $\omega_{0p1}, \omega_{0p2}, \omega_{0s}$  and  $\omega_{0i}$  respectively. Top-left inset: Pseudo-spin-up/down excitations, Unit cell of the lattice, where the gauge flux is  $\pm\pi$  in a single plaquette, and zero over a unit cell of 2 plaquettes (shaded yellow). Level diagrams for DP-SFWM and ND-SFWM. Top-right inset: The photons from ND-SFWM are filtered out by measuring coincidences and the pump photons are spectrally filtered. Middle inset shows the image of the device obtained using a camera.

Here  $a_i^\dagger (a_i)$  is the creation (annihilation) operator at a lattice site  $i = (x, y)$ . The summations  $\langle i, j \rangle$  and  $\ll i, j \gg$  are over the nearest and the next-nearest neighbor lattice sites, respectively. The phase  $\phi_{i,j} = \pm\pi/4$  for nearest-neighbor hoppings. For a finite lattice, the band gap hosts topological edge states that are confined to the boundary of the lattice. More importantly, the edge states are robust against disorder, for example, against variations in the ring resonance frequencies. The edge states also exhibit a linear dispersion [14, 24, 25]. The band structure of the lattice and the presence of edge states can be probed by measuring the transmission and the delay spectra of the lattice from input to the output port. The simulated transmission and delay spectra for a  $8 \times 8$  lattice are shown in Figs. 3.1(b,c). The linear dispersion of the edge states manifests in the Wigner delay spectrum as a flat profile (Fig. 3.1(c)). In contrast, the Wigner delay in the bulk band varies significantly because in a finite lattice, the bulk bands do not have a well defined momentum. Our system also supports a pseudospin degree of freedom because of the two circulation directions (clockwise and counter-clockwise) in the ring resonators. The two pseudospins are time-reversed partners, and therefore, experience opposite hopping phases and counter propagating edge states.

To generate indistinguishable photon pairs in this lattice, we use the  $\chi^{(3)}$  nonlinearity of silicon and implement dual-pump SFWM. We pump the lattice using two classical, continuous-wave pump beams in two longitudinal modes of the lattice separated by two free-spectral ranges (FSRs, see Fig. 3.1). The DP-SFWM then leads to the generation of indistinguishable photon pairs, called signal and idler, in the longitudinal mode located midway between the two pump modes such that the

energy conservation relation is satisfied. This nonlinear process is described by the Hamiltonian

$$H_{\text{NL}} = \eta \sum_m \left( a_{m,s}^\dagger a_{m,i}^\dagger a_{m,p_1} a_{m,p_2} + a_{m,p_1}^\dagger a_{m,p_2}^\dagger a_{m,s} a_{m,i} \right), \quad (3.2)$$

Here  $\eta$  is the efficiency of the SFWM process, and  $a_{m,\mu}^\dagger$ , with  $\mu = s, i, p_1, p_2$ , is the photon creation operator for signal, idler or pump photons at a lattice site  $m$ . The DP-SFWM adds or removes photons in pairs, and therefore, in the low-loss regime, leads to single-mode squeezed light. We note that each of the two pump beams also generate distinguishable photon pairs via non-degenerate SFWM (ND-SFWM). However, because of the energy conservation ( $2\omega_{p_i} = \omega_s + \omega_i$ ), these photon pairs are generated in longitudinal modes located symmetrically around the respective pump beams. Therefore, we use spectral filtering and time-resolved coincidence measurements between correlated photon pairs generated via DP-SFWM to exclude the noise photons generated by ND-SFWM.

Next, we show the method to simulate the intensity of output photon generation in the anomalous Hall device. We assume that the pump fields are much stronger than the signal and hence use the linear evolution to describe the evolution of the pump fields. Using input-output formalism and rotating wave approximation in [5, 46], we derive the steady state pump fields evolution to be [18],

$$-i\omega_{p_i} a_{m,p_i} = i[H_L, a_{m,p_i}] - \kappa_{in} a_{m,p_i} - (\delta_{m,I} + \delta_{m,O}) \kappa_{ex} a_{m,p_i} - \delta_{m,I} \sqrt{2\kappa_{ex}} a_{in,p_i}, \quad (3.3)$$

Here,  $\kappa_{ex}$  is the coupling strength of the lattice to input/output waveguides,  $\kappa_{in}$  is the loss and  $a_{in,p_i} \in [a_{in,p_1}, a_{in,p_2}]$  are the input pump fields. The input and output

waveguides are coupled to the lattice at sites indexed by  $I, O$ . The steady state signal field evolution given by,

$$-i\omega_\rho a_{m,s/i} = i [H_L + H_{NL}, a_{m,s/i}] - \kappa_{in} a_{m,s/i} - (\delta_{m,I} + \delta_{m,O}) \kappa_{ex} a_{m,s/i} - \delta_{m,I} \sqrt{2\kappa_{ex}} a_{in,s/i}, \quad (3.4)$$

We determine the signal/idler at the output of the lattice by  $a_{out,s/i} = \sqrt{2\kappa_{ex}} a_{O,s/i}$  using the input-output formalism.

### 3.3 Experimental Setup

We use the same topological device as in Chapter 2 for measurements, where the coupling strength  $J \simeq 15.6$  GHz. Figure 3.2(a) shows the measured transmission spectrum of the device for spin-up excitation, with the edge band highlighted in color. The edge states for this excitation take the shorter route from input to the output coupler, as shown in Fig. 3.1(a).

We use tunable continuous-wave lasers and EDFA's to pump the lattice ( $\omega_{p_1}, \omega_{p_2}$ ). The corresponding resonance frequencies of pumps, signal and idler are given by  $\omega_{0p_1}, \omega_{0p_2}, \omega_{0s}$  and  $\omega_{0i}$  respectively. Filters are used to remove the pumps from the photons. A beam-splitter is used with conjunction of a time-correlated single-photon counting (TCSPC) module and two single photon superconducting nano-wire detectors (SNSPDs) to measure the timing of coincidences. The inset in Fig. 3.1(a) shows a typical coincidence histogram where the coincidences are calculated by integrating the points in the full-width at half maximum of the histogram peak.

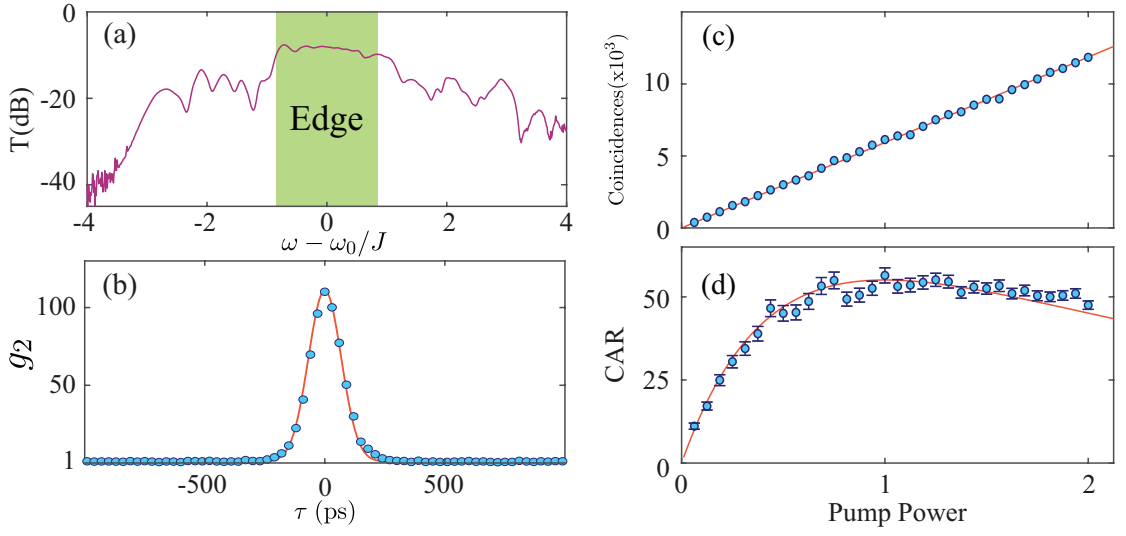


Fig. 3.2: (a) Measure transmission spectrum of device. The shaded region is the edge band. (b) Second order cross correlation as function of time. (c) Coincidences as function of one of the pumps power's, while the other pump power is fixed at 3 mW. (d) CAR as function of one of the pumps power's, while the other pump power is fixed at 3 mW.

### 3.4 Characterisation of the quantum source

In order to characterize the purity of the two photon source, we look at the second order cross-correlation ( $g_2(\tau)$ ) which also measures the amount of bunching between photons. A true two-photon source results in a  $g_2^{cc}(\tau = 0) > 2$ . A coincidence histogram is used to measure  $g_2(\tau)$  as shown in Fig. 3.2(b) when  $P_1 = 1$  mW and  $P_2 = 3$  mW at the input of the lattice. We observe a  $g_2(\tau = 0) \approx 117$  showing that photons are indeed strongly correlated.

We find the signal-to-noise ratio of the photon source by measuring coincidences to accidental ratio (CAR) in the histogram. We integrate  $g_2(\tau)$  around the peak to calculate the actual coincidences and divide it by the mean at  $\tau \gg 0$  which are the noise photons. The resulting ratio gives a CAR of  $\approx 53$  showing that it is a high quality two-photon source. We also verify the behaviour of CAR as an function of one of the pump powers when the other pump is fixed. The theoretical CAR is calculated using

$$CAR = \frac{\eta P_{p_1} P_{p_2}}{(\eta P_{p_1}^2 + \eta P_{p_2}^2 + \eta P_{p_1} P_{p_2})^2}, \quad (3.5)$$

where the  $P_{p_i}$  is the power of the pump i. The theoretical CAR curve increases to a maximum and then falls down as a function of pump power. For low powers, the CAR is limited by noise from SFWM process. Fig. 3.2(d) shows the measured CAR as function of one pump power as the other pump power is fixed at 3 mW and agrees very well with the corresponding theoretical curve. We also verified that coincidences are from DP-SFWM by varying one pump power, while the other pump is fixed at 3mW (Fig. 3.2(c)). The curve follows linearly as expected, since the

coincidences scale as  $P_{p_1}P_{p_2}$ .

### 3.5 Spectral Correlations in an Anomalous Hall Device

To measure the spectral correlations between the two pump fields and the generated photons, we first measure the number of indistinguishable photon pairs generated via DP-SFWM as a function of the two pump frequencies  $(\omega_{p_1}, \omega_{p_2})$ . Fig. 3.3(a) shows the measured number of coincidence counts as a function of the two pump frequencies over an acquisition time of 10 seconds. We observe that the photon generation rate is maximum when both the pump frequencies are in the edge band,  $[-J, J]$ . Furthermore, compared to the bulk band regions, the generation rate is relatively uniform throughout the edge band. We note that because of the presence of four fields in the D-SFWM process ( $\omega_{p_1} + \omega_{p_2} = \omega_s + \omega_i$ ), the current plot does not yield any information about the spectral correlations between generated photons.

Next, we fix the input pump frequencies to be in the middle of the edge band at  $\simeq 0J$ ,  $\omega_{p_1} - \omega_{0p_1} = \omega_{p_2} - \omega_{0p_2} = 0J$  (in respective longitudinal modes) and measure the joint spectral intensity (JSI) between generated signal and idler photons  $[\Gamma(\omega_s, \omega_i)]$ . We use a beam-splitter and two spectrometers to measure the JSI. The measured JSI shows that, with the two pump fields in the edge band, the spectra of generated signal and idler photons is also limited to the edge band. This is because of the linear dispersion of the edge states that leads to efficient phase matching (momentum conservation) when all the four fields are in the edge band, and also because of the confinement of the edge states to the lattice boundary that

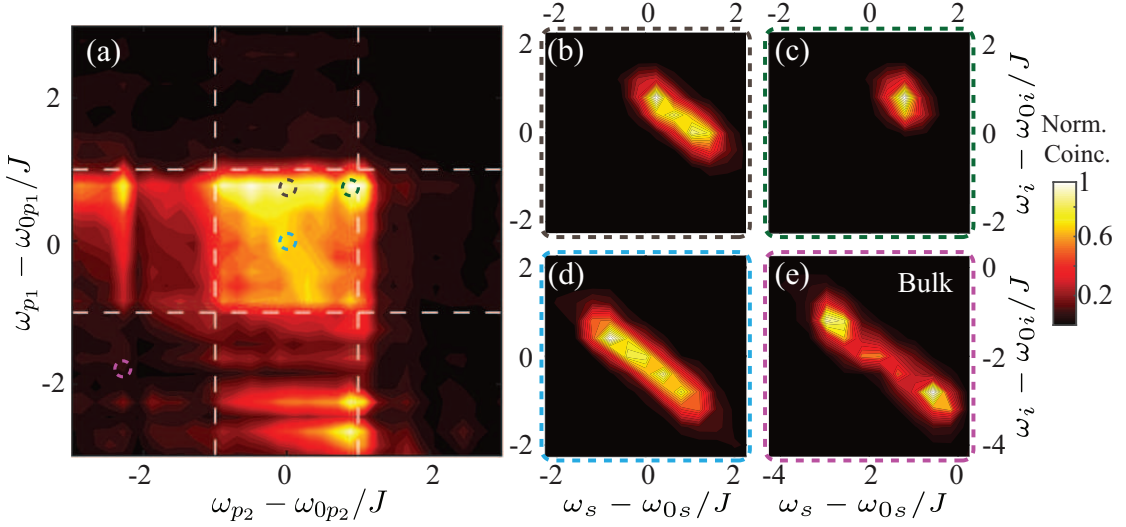


Fig. 3.3: (a-d) Measured Joint spectral intensity of the signal photons at  $[\omega_{p_1} - \omega_{0p_1}, \omega_{p_2} - \omega_{0p_2}] = [.8J, .8J], [.8J, 0J], [0J, 0J], [-1.82J, -2.42J]$  respectively.

leads to a good spatial overlap between the fields. Furthermore, both the signal and idler spectra are centered around  $0J$  which indicates that they are degenerate in frequency. Given the facts that our ring resonator waveguides supports a single TE polarized mode and the generated photons are collected from a single spatial mode (the same output port), the generated photons are indistinguishable in all degrees of freedom. Note that we use continuous-wave pumps in our experiments, and the apparent width of spectral correlations along the diagonal is because of the finite spectral resolution ( $\approx 10GHz \simeq 0.64J$ ) of our measurements.

To show the tunability of the spectra of generated photons, we measure the signal-idler JSI correlations for different pump positions in the edge band. For example, when both the pump frequencies are near the side of the edge band  $\omega_{p_1} - \omega_{0p_1} = \omega_{p_2} - \omega_{0p_2} = .8J$ , we observe that the spectra of generated photons is significantly narrower (*by*  $\approx 3X$ ) than that when both the pumps are in



the center of the edge band (Fig. 3.2(d)). This is again because of the efficient energy and momentum conservation in the edge band that limits the spectra of generated photons. Also, as expected, the spectra are centered around  $0.8J$ . Similarly, when the two pump frequencies are at different locations in the edge band  $\omega_{p_1} - \omega_{0p_1} = .8J, \omega_{p_2} - \omega_{0p_2} = 0J$ , we observe that the spectra of generated photons are centered around  $0.4J$ . We contrast these results by exciting the pumps in the bulk band, when  $\omega_{p_1} - \omega_{0p_1} = -1.82J, \omega_{p_2} - \omega_{0p_2} = -2.42J$ . We observe that spectrum is uneven and supports multiple modes due to the randomized dispersion in the bulk band.

### 3.6 *HOM experiment*

Though our spectral measurements indicate that the generated photons are indistinguishable, Hong-Ou-Mandel interference [47] can confirm the indistinguishability of photons. In HOM interference, two indistinguishable photons arriving simultaneously at the two input ports of a beam-splitter bunch together at the output. However, in our topological source, both the photons are in a single spatial mode, they are degenerate in frequency, and have same polarization. Therefore, as required for HOM interference, they can not be separated into two spatial modes using a normal beam-splitter which is probabilistic and gives only 50% interference visibility. Nevertheless, the two photons can be deterministically separated using time-reversed HOM interference in beam-splitter when the input to the beamsplitter is a path-entangled state of the form  $|20\rangle_{A,B} + |02\rangle_{A,B}$ , that is, both the photons

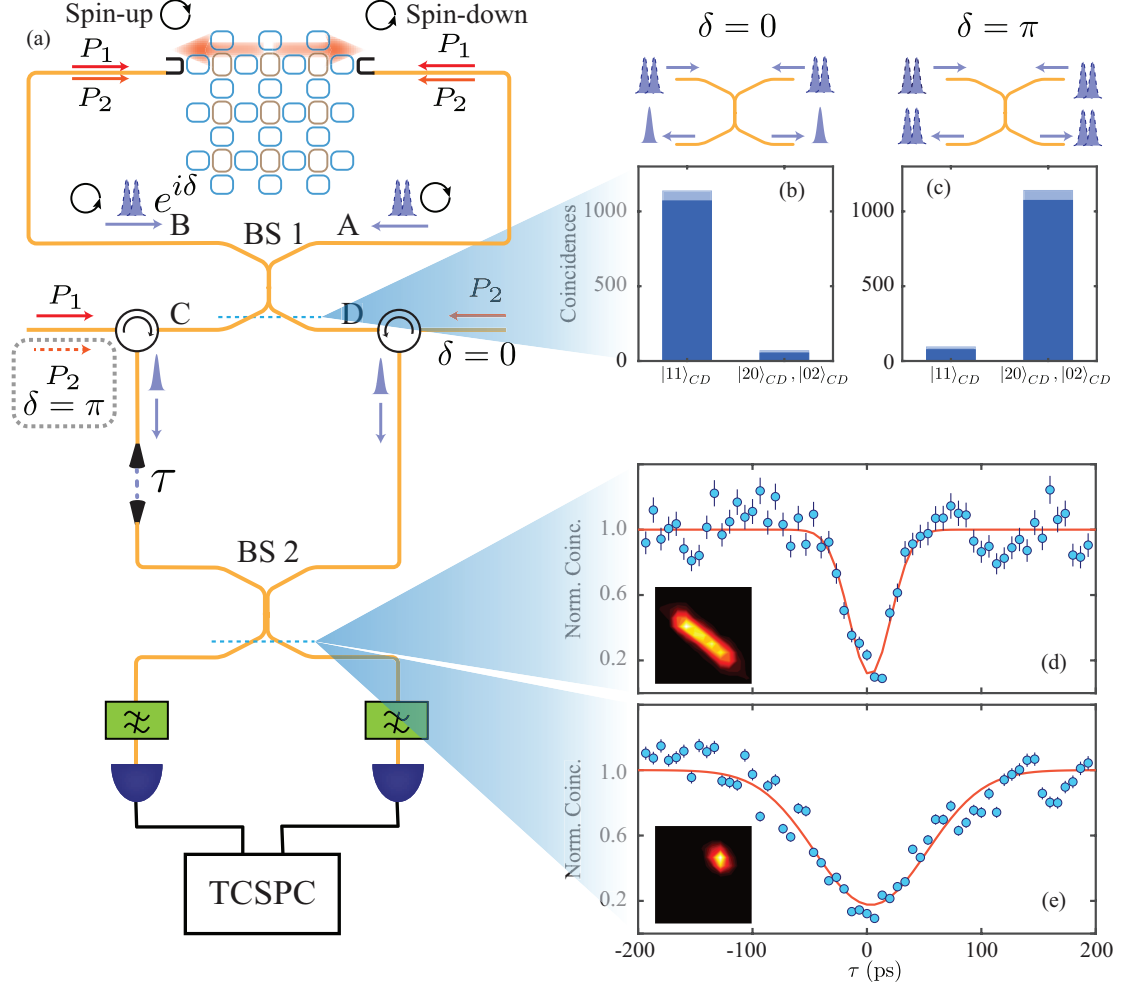


Fig. 3.4: (a) Schematic of the Sagnac interferometer setup used to deterministically split the two photons via time-reversed HOM interference of a path-entangled two-photon state (at beamsplitter BS1), and subsequently, realize HOM interference at beamsplitter BS2 with a variable delay  $\tau$  between the two photons. (b) Measured two-fold coincidences at the output ports C, D of the beam splitter BS1, for two different configurations of the input pump beams. The photons anti-bunch (bunch,  $\delta = \pi$ ) when the two pumps are in separate (same,  $\delta = 0$ ) input ports of BS1. (c,d) Measured HOM interference dip for  $\delta = \pi$ , and the pump frequencies  $\omega_{p1} - \omega_{p10} = \omega_{p2} - \omega_{p20} = 0$  and  $\omega_{p1} - \omega_{p10} = \omega_{p2} - \omega_{p20} = .8J$ , respectively. Insets show the measured JSI.

arrive either at the input port A or at port B of the beamsplitter. Here the state  $|nm\rangle_{A,B}$  refers to  $n$  photons in the first port of the beamsplitter and  $m$  photons in the second port.

To implement this deterministic beamsplitter, we use our topological source in a Sagnac interferometer (formed by beamsplitter BS-1) [41–43]. In this configuration, both the pseudospins (up and down) associated with our source are simultaneously pumped (Fig. 3.4(a)). Because they are time-reversed partners, the pump beams corresponding to the two pseudospins propagate through the same edge state, but in opposite directions, and generate an entangled two-photon state  $|20\rangle_{A,B} + e^{i\delta}|02\rangle_{A,B}$  at ports A, B of the beamsplitter BS-1. The relative phase  $\delta$  of two-photon entangled state can be set to 0 or  $\pi$  by appropriately choosing the input ports for the two pump beams at the Sagnac beamsplitter (BS 1 in Fig. 3.4(a)). When both the pumps are in the same port of the BS-1 (Port C or Port D), the phase  $\delta = 0$ , and the two photons bunch at the output of BS-1, that is, they appear at either port C or port D of BS-1 (Fig. 3.4). In contrast, when the two pumps are in different ports of the beamsplitter BS-1 (one in Port C, and the other in Port D), the phase  $\delta = \pi$  and it leads to anti-bunching of photons such that the photons are deterministically separated at the output of the BS-1. In our experiment, we use two circulators to collect the photons at ports C and D. The pumps are excited at  $\omega_{p1} - \omega_{p10} = \omega_{p2} - \omega_{p20} = 0$  and the corresponding measured coincidence histograms for the two configurations of pumps are shown in Figs. 3.4(b-c). For  $\delta = 0$ , we measure the anti-bunching ratio to be 89(1)%, and for  $\delta = \pi$ , we measure the bunching ratio to be 86(1)%. We emphasize that the use of a Sagnac interferometer, with

the two pumps beams injected at different input ports, alleviates the need for any active stabilization of our source.

To demonstrate HOM interference we set  $\delta = 0$  such that the two photons are deterministically separated in the ports C and D of the beamsplitter BS-1. We pump our source in the middle of the edge band, that is,  $\omega_{p1} - \omega_{p10} = \omega_{p2} - \omega_{p20} = 0$ . We introduce a relative delay between the two photons, interfere them on another beamsplitter (BS-2), and measure the coincidence counts at the output of BS-2 as a function of the delay  $\tau$  between the photons. As expected, we see a HOM dip in the coincidence counts, with a visibility of 88(10)%, which confirms that the two photons are indeed indistinguishable. The small degradation of visibility is from 48/52 splitting ratio of the beam-splitter, small mismatch in spectral filtering between filters. The high visibility of the HOM shows that the topological edge states could be a good source of identical photons. Here, we observed that the backscattering in the fibers contributed to noise in the output arms of the circulator and washing out the output signal. To solve this, we used monochromators of bandwidth  $\approx 200\text{pm}$  in conjunction to WDM filters to filter the coincidences. The bandwidth of the device is larger than the spectral width of the generated photons. Note, the backscattering would not be an issue if the sagnac loop was implemented on-chip due to minimized path length.

We note that the temporal width of the HOM interference dip is inversely related to the spectral width of the joint-spectral intensity (along the line  $\omega_s - \omega_{0s} = -\omega_i - \omega_{0i}$ ) that characterizes the two-photon state. As we demonstrated in Fig. 3.3, we can control the JSI of generated photons in our source by simply tuning the

input pump frequencies (Fig. 3.2). To demonstrate similar control in the HOM interference, we set the two pump frequencies to be at one of the extremes of the edge band  $\omega_{p_1} - \omega_{0p_1} = \omega_{p_2} - \omega_{0p_2} = .8J$ , such that the spectral width of the JSI is  $\approx .6J$  (Fig. 3.2(c)). We now observe that the temporal width of the HOM interference dip with a visibility of 82(7)% is indeed much larger (by a factor of  $\approx 2.7(4)$ ) compared to the case with both the pumps in the center of the edge band. This increase in temporal width of the HOM interference is in agreement with the decrease in the spectral width of the measured JSI (by a factor of  $\approx 4(6)$ ). This discrepancy is mainly because of the limited spectral resolution of our JSI measurements.

### 3.7 *Energy-time entanglement*

Finally, we show that the generated two-photon state is energy-time entangled. The use of a continuous-wave pump for generating photon pairs via SFWM (or SPDC) naturally leads to the emergence of energy-time entanglement such that  $\Delta\omega\Delta T < 1$ , where  $\Delta\omega = \Delta\omega_s + \Delta\omega_i$  is the uncertainty in the total energy of the signal and idler photons, and  $\Delta T$  is the uncertainty in the time duration between arrival of two photons [48–51]. We use a beam splitter to probabilistically split the two photons at the output of our source, and inject them into two Franson interferometers with a path-length delay ( $\approx 800$  ps) much larger than the temporal correlation of the generated photons ( $\approx 200$  ps). The phase( $\theta$ ) in the interference path is controlled through a peizo-controlled delay stage (Fig. 3.5(a)). Time-resolved

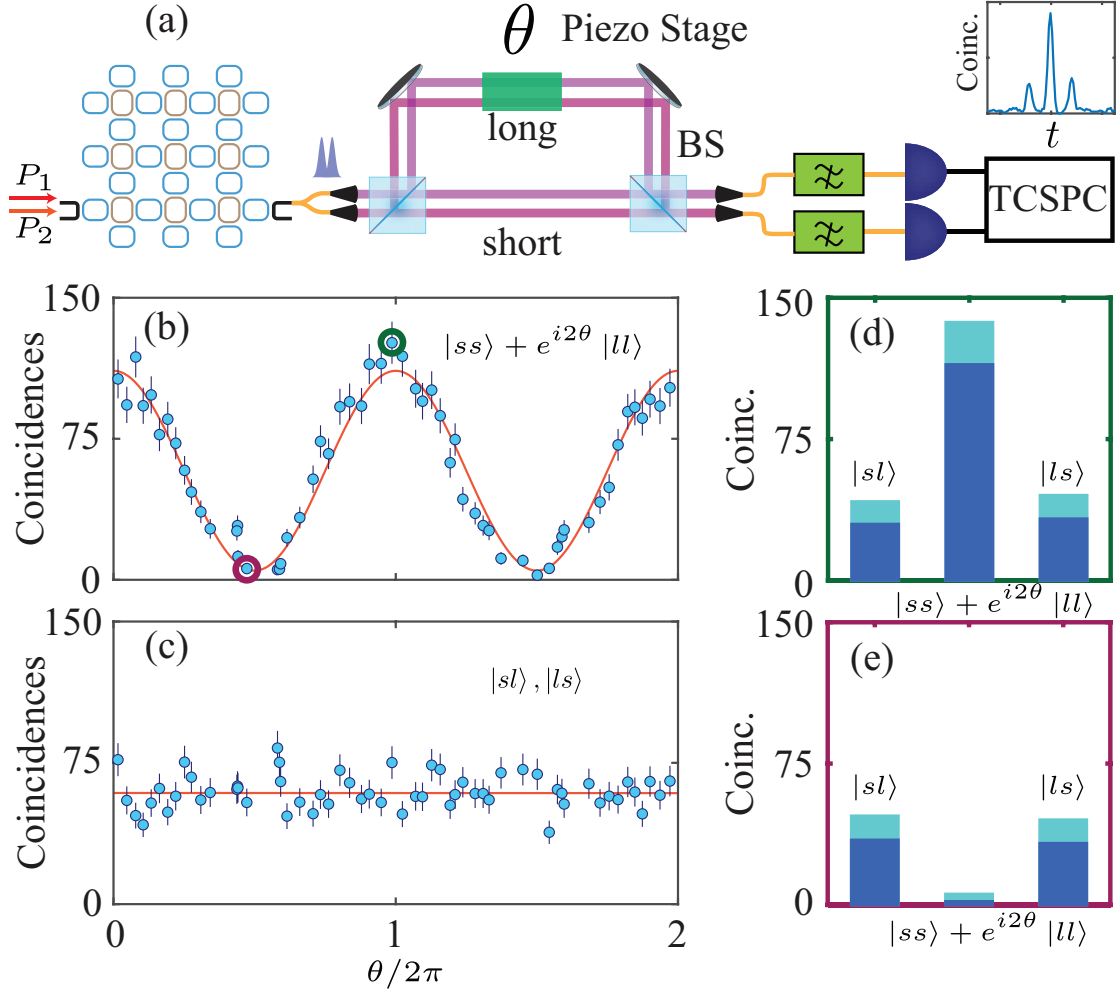


Fig. 3.5: (a) Setup of Franson interferometer (b) Coincidences in  $|sl\rangle, |ls\rangle$  as a function of phase (c) Coincidences in  $|ss\rangle + e^{i2\theta}|ll\rangle$  as a function of phase (d-e) Histograms at the minimum and maximum in the interference curve of  $|ss\rangle + e^{i2\theta}|ll\rangle$ .

coincidence measurements at the outputs of the interferometers show three peaks (Fig. 3.5). The first/third peak in the histogram corresponds to the one photon taking the short/long path and other taking the long/short path( $|sl\rangle / |ls\rangle$ ). The middle peak shows the interference when both the photons take the same path either short/long( $|ss\rangle + e^{i2\theta} |ll\rangle$ ). We measure the number of coincidence counts in the three peaks as we vary the phase  $\theta$  of the interferometers. The latter two cases (both short or both long) are indistinguishable, and therefore, we observe interference fringes in the coincidence counts as a function of the two-photon phase  $2\theta$  acquired in the interferometer. Figure 3.5(d-e) shows the coincidence histogram at the output of the detectors for phases of  $\theta = \pi, 2\pi$  when the pumps are excited at  $\omega_{p_1} - \omega_{0p_1} = \omega_{p_2} - \omega_{0p_2} = .8J$ . In contrast, the other two cases, where one photon travels through the shorter path and the other through the longer path, are distinguishable and accordingly yield no interference. Our observation of two-photon interference fringes with a fringe visibility of 92(6)% for a path-length delay in the interferometers that is much longer than the temporal correlation width of the photons, demonstrates that the coherence time of our generated two-photon state is much longer and it is indeed energy-time entangled.

### 3.8 Comparison with 1D CROW devices

Lastly, we compare the spectral correlations in topological devices with a topologically trivial devices such as a 1D array of coupled resonator optical waveguides (CROW). A 1D CROW device consists of 8 ring-resonators, the same length as

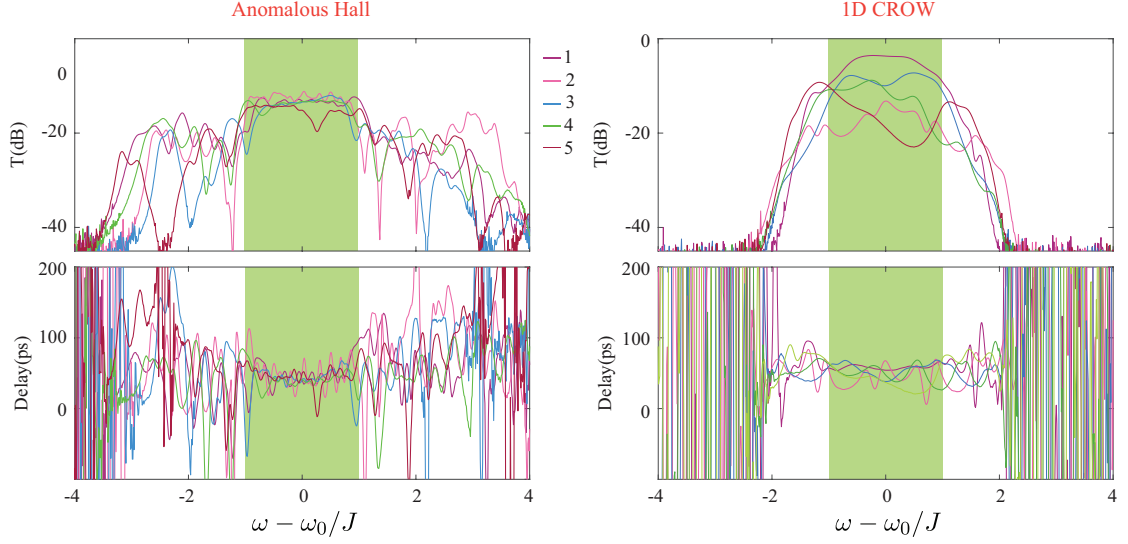


Fig. 3.6: (a) Measured transmission and delay spectra of five Anomalous Hall devices, (b) Measured transmission and delay spectra of five 1D CROW devices.

the short edge in our topologically non-trivial device. The CROW devices are also designed on the same chipsets and have the same amount of disorder as 2D devices. Since CROW devices are susceptible to fabrication-induced disorder, the output spectral correlations vary across devices due to randomized dispersion. Here, we measure the transmission and delay spectra of five anomalous Hall and five 1D CROW devices in Fig. 3.6 with the same fabrication parameters. Despite having the same disorder, we observe that 2D devices have a flatter spectrum, delay in the edge band and show smaller deviations across devices. The 1D devices show a varying spectrum and larger deviations across devices in the center band showing their susceptibility to disorder.

Next, we measure the number of indistinguishable photon pairs generated as a function of the two pump frequencies of five different anomalous Hall devices (Figures 3.7(a-e)). Even with the fabrication-induced disorder of  $2J$  (33 GHz)



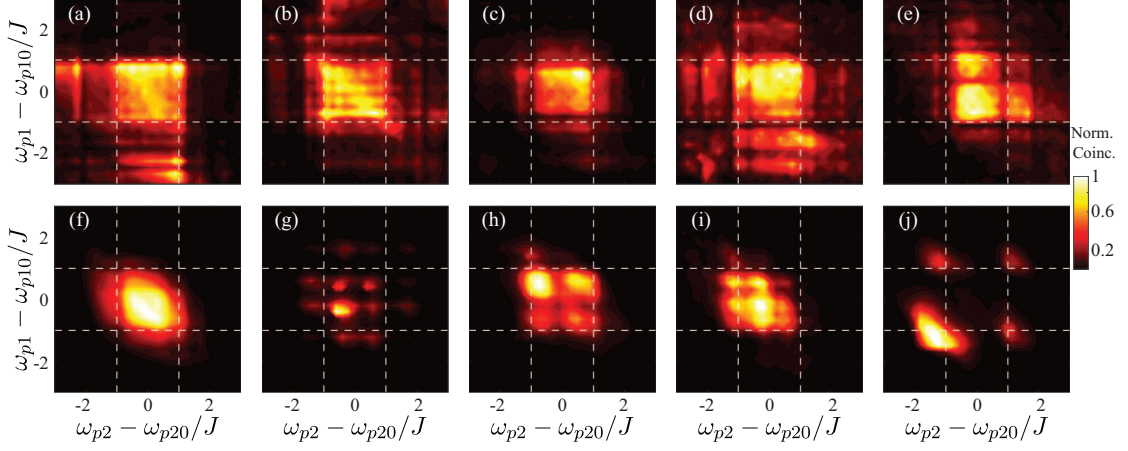


Fig. 3.7: (a-e) Output spectrum of five different anomalous Hall devices. We observe the spectral correlation are uniform in the edge bands of these devices. (f-i) Output spectrum of five different 1D CROW devices where, the disorder affects the spectral correlations.

comparable to the bandgap of device, the spectral correlations of all the devices exhibit consistent and maximum coincidences in the edge bands. The spectrum in the bulk bands on the other hand vary from device to device due to disorder. By comparison, we observe that the spectral correlations for five 1D CROW devices behave similarly to bulk bands and produces a changing spectral correlations from one device to device (Figs. 3.7(f-j)). We quantify the similarity between devices across the center band using a parameter, similarity. The similarity between two devices  $p$  and  $p'$  is calculated by taking the mean of the inner product between two spectra and is given by,

$$S_{p,p'} = \left[ \sqrt{\Gamma_{Np}\Gamma_{Np'}} \right]^2 \quad (3.6)$$

where  $\Gamma_{Np}$  is the normalized spectral correlations  $\Gamma_p$  with the maximum value of coincidences in the complete band of the device. The range of spectral correlations

to calculate similarity is taken over a bandwidth of  $2J$  in the center band. A higher value of similarity implies that center band has a maximum and the spectra is more even in the band. We observe an average similarity of .5(1) for 2D devices and .2(1) for 1D devices. This contrast clearly shows the triumph of topological robust edges over CROW devices in susceptibility of fabrication-induced disorder.

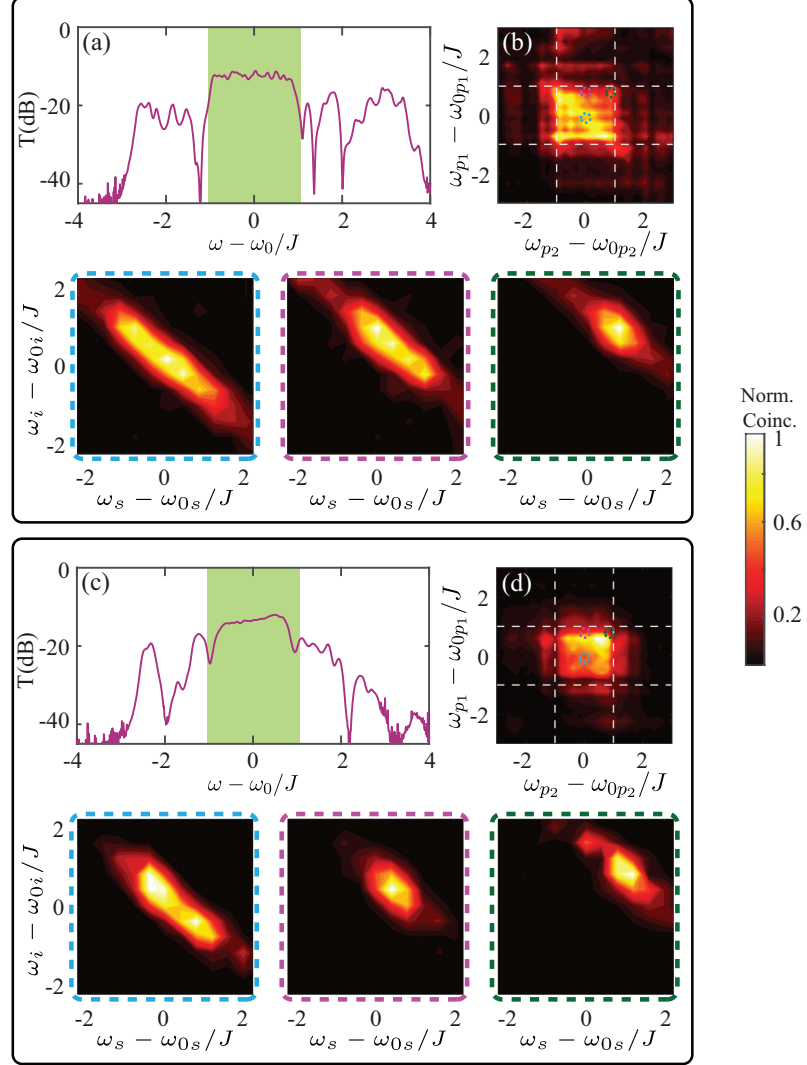


Fig. 3.8: (a-b,c-d) Transmission and output spectrum of two different anomalous Hall devices. Insets show corresponding JSI's when the pumps are excited at  $[\omega_{p1} - \omega_{0p1}, \omega_{p2} - \omega_{0p2}] = [0J, 0J], [0.8J, 0J], [0.8J, 0.8J]$ .

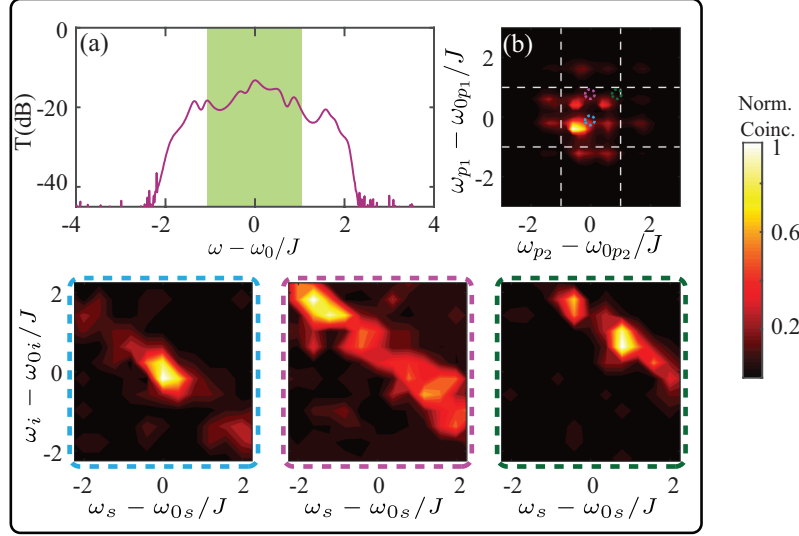


Fig. 3.9: (a-b) Transmission and output spectrum of a 1D CROW device. Insets show JSI's when the pumps are excited at  $[\omega_{p_1} - \omega_{0p_1}, \omega_{p_2} - \omega_{0p_2}] = [0J, 0J], [0.8J, 0J], [0.8J, 0.8J]$ .

In the above section, we have looked at the photon pair generation as a function of pump frequencies for different 2D devices. Here, we look at the robustness of spectral correlation between generated photons and the tunable nature of our devices. We measure the spectral correlations between generated photons (JSI) for two different anomalous Hall devices at the three different pump locations,  $[\omega_{p_1} - \omega_{0p_1}, \omega_{p_2} - \omega_{0p_2}] = [0J, 0J], [0.8J, 0J], [0.8J, 0.8J]$ . The measured JSI is robust against disorder as shown in Figs. 3.8(a-e). We also measure the JSI for a 1D CROW device as shown in Figs. 3.9(a-b) for the corresponding pumps and observe that generated JSI is prone to disorder and excites different localized modes. This is due to randomized dispersion in 1D devices. These results also show that the generated spectra of photons are robust against disorder for the topological 2D devices.

### 3.9 *Summary*

In summary, we have demonstrated a topological source of indistinguishable, energy-time entangled photon pairs generated via dual-pump SFWM. We showed that the linear dispersion of the edge states leads to an enhanced generation of photon pairs, and allows us to tune the spectral bandwidth of the generated two-photon state by simply tuning then input pump frequencies. We confirmed the indistinguishability of the photon pairs and the tunability of their spectral bandwidth using HOM interference. We also demonstrated the energy-time entanglement between photon pairs that naturally emerges because of the energy conservation and the use of continuous-wave pump beams. In addition, we showed that anomalous Hall devices outperform 1D CROW devices and produce a consistent output spectrum in presence of fabrication-induced disorder. Recent works [\[52\]](#) have produced photon pair sources in single ring devices which have comparable efficiencies to SPDC making them a good alternative. If these high efficiencies were to be achieved using topological edge states, it could create scalable, tunable, and robust photon sources on-chip that could enable many applications in quantum information and quantum computing.

## Chapter 4: Two-photon transport in the quantum Hall systems

### *4.1 Introduction*

In the previous chapter, we studied the generation of non-classical light on a topological device. Now, we study the transport of non-classical light in these topological devices. In order to study quantum transport, we first briefly describe qubits, the building blocks of quantum communications, and how they are represented in our system.

### *4.2 Qubits*

The demand for high-speed communications in the information-driven age is rapidly increasing. When the chipsets fabricated become smaller and smaller, we surpass classical mechanics and enter into the quantum domain. Learning to use and manipulate quantum effects can enable us to achieve faster and secure communications, as well as, to help solve problems that are exponentially hard in complexity for a classical computer. Qubits are the bits of a quantum system. Unlike classical systems, a quantum system has a state which is a superposition of

both the levels

$$|\psi\rangle = \alpha |0\rangle + \beta |1\rangle, \quad (4.1)$$

where  $|\psi\rangle$  is the wave function,  $\alpha$  and  $\beta$  are the probability amplitudes, which can be complex and satisfy the condition  $|\alpha|^2 + |\beta|^2 = 1$ . The probability amplitudes are obtained after performing measurements on the system as the state collapses to one of the qubit states (0 or 1). In a quantum system, one can manipulate states by applying unitary operations (rotations, reflection, etc.) on the system which are reversible operations. One can also make qubits using distinguishable properties of electrons or photons like polarisation, time, spin, etc.

In our system, we use time of arrival of photon as a qubit. A single photon is sent through a Mach-Zander interferometer with a delay placed in one of the arms as shown in Figure 4.1. Two possible outcomes are expected at the output; the photon can arrive early if it takes the shorter path or it can arrive late if it goes through the delayed path. A qubit could be constructed using time of arrival of the photon in this setup which is also known as time-bin qubit. The state of the photon could be expressed as

$$|\psi\rangle = \alpha |e\rangle + \beta |l\rangle, \quad (4.2)$$

where  $|e\rangle$  and  $|l\rangle$  correspond to the photon being in early and late time-bins respectively.

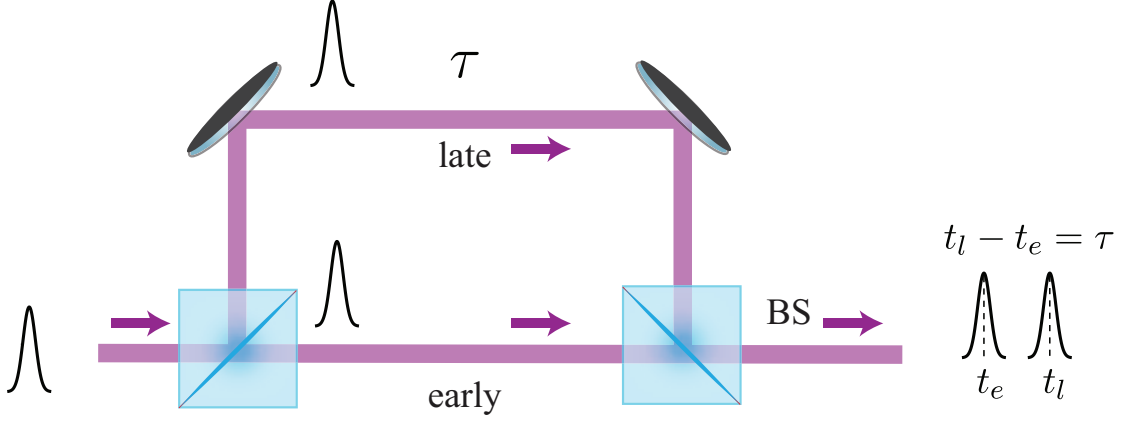


Fig. 4.1: Time-bin qubit setup. The photon could either take the shorter/longer path resulting in an early/late time of arrival.

### 4.3 Entanglement

Entanglement is one of the distinguished features of quantum mechanics which does not have an equivalent classical counterpart. One can write a general two qubit state as

$$|\psi\rangle_{A,B} = \alpha |0\rangle_A |0\rangle_B + \beta |0\rangle_A |1\rangle_B + \gamma |1\rangle_A |0\rangle_B + \delta |1\rangle_A |1\rangle_B, \quad (4.3)$$

where  $A$  and  $B$  are the two qubits of the system. If the above state can be decomposed as a product of superpositions of each qubit, the state is called a separable state. For example, it can be represented by

$$\begin{aligned} |\psi\rangle_{A,B} &= |\psi\rangle_A |\psi\rangle_B \\ &= (\alpha_A |0\rangle + \beta_A |1\rangle) (\alpha_B |0\rangle + \beta_B |1\rangle), \end{aligned} \quad (4.4)$$

Suppose we measure a qubit  $A$  and observe it to be  $|0\rangle$  state, the wavefunction of qubit  $A$  collapses, but does not affect the state of  $B$ . A measurement on qubit  $B$  yields a probability of  $\alpha_B^2$  to be in state  $|0\rangle$  and  $\beta_B^2$  in state  $|1\rangle$ . Measurement of  $A$

does not effect the measurement of  $B$  and hence they are not correlated measurements. The physics here can be described as if all the particles are independent.

There are some other two qubit states which can be written as the following

$$|\Psi^\pm\rangle_{A,B} = \alpha |0\rangle_A |0\rangle_B \pm \beta |1\rangle_A |1\rangle_B, \quad (4.5)$$

$$|\Phi^\pm\rangle_{A,B} = \alpha |0\rangle_A |1\rangle_B \pm \beta |1\rangle_A |0\rangle_B, \quad (4.6)$$

These states are called maximally entangled states or Bell states. If we measure qubit  $A$  of  $|\Psi^+\rangle_{A,B}$  to be in state  $|0\rangle$ , the measurement collapses the wavefunction and forces the state of  $B$  in state  $|0\rangle$ . Here, measurement of one qubit effects the state of the other and vice-versa. This shows that there is some sort of correlation between measurements of the two qubits and this property is called entanglement. In generic states which are not separable and not maximally entangled, there is partial entanglement in the states.

For time-bin qubits, there are only three bell states which are given by

$$|\Psi^+\rangle = \frac{1}{\sqrt{2}} (|e\rangle_1 |l\rangle_2 + |e\rangle_1 |l\rangle_2), \quad (4.7)$$

$$|\Phi^+\rangle = \frac{1}{\sqrt{2}} (|e\rangle_1 |e\rangle_2 + |l\rangle_1 |l\rangle_2), \quad (4.8)$$

$$|\Phi^-\rangle = \frac{1}{\sqrt{2}} (|e\rangle_1 |e\rangle_2 - |l\rangle_1 |l\rangle_2), \quad (4.9)$$

where  $|e\rangle_{1,2}$  and  $|l\rangle_{1,2}$  corresponds to a single photon state in early and late time-bins respectively. The fourth bell state is not considered because it is anti-symmetric under exchange of photons.



#### 4.4 Integer Quantum Hall Effect

The photonic structure for implementing a quantum spin-Hall system consists of a 2D array of ring resonators which are coupled through off-resonant link rings [5]. Similarly to anomalous Hall device, the link rings serve as waveguides and determine the hopping phase and coupling between the rings. The link rings are slightly shifted from each other along the rows such that they introduce a direction dependent phase as in Figure 4.2 [53]. This arises from photons travelling different path lengths due to the shifted link ring. The shifts are chosen to ensure that photons acquire a hopping phase along x direction which is a linear function of the row number  $y$ . The resulting overall phase in a round trip around a single unit cell would be  $\phi$ . This system simulates a tight binding model Hamiltonian with magnetic field whose hamiltonian is given by,

$$H = \sum_{x,y} \omega_0 \hat{a}_{x,y}^\dagger \hat{a}_{x,y} - J \left( \hat{a}_{x+1,y}^\dagger \hat{a}_{x,y} e^{+iy\phi} + \hat{a}_{x,y}^\dagger \hat{a}_{x+1,y} e^{-iy\phi} + \hat{a}_{x,y+1}^\dagger \hat{a}_{x,y} + \hat{a}_{x,y}^\dagger \hat{a}_{x,y+1} \right), \quad (4.10)$$

where,  $J$  is the next neighbour coupling between the rings,  $\omega_0$  is the ring resonance frequency,  $\phi$  is the synthetic magnetic flux in an unit cell,  $\hat{a}_{x,y}^\dagger$  and  $\hat{a}_{x,y}$  are photon creation and annihilation operators at site  $(x, y)$  respectively.

Figure 4.2(c) shows the transmission of a  $8 \times 8$  lattice when  $\phi = \pi/2$ . The lattice supports unidirectional clockwise (CW) and counter-clockwise (CCW) edge states which travel around the perimeter of the lattice. These topological edge states have been experimentally demonstrated to be robust against disorder [14], whereas

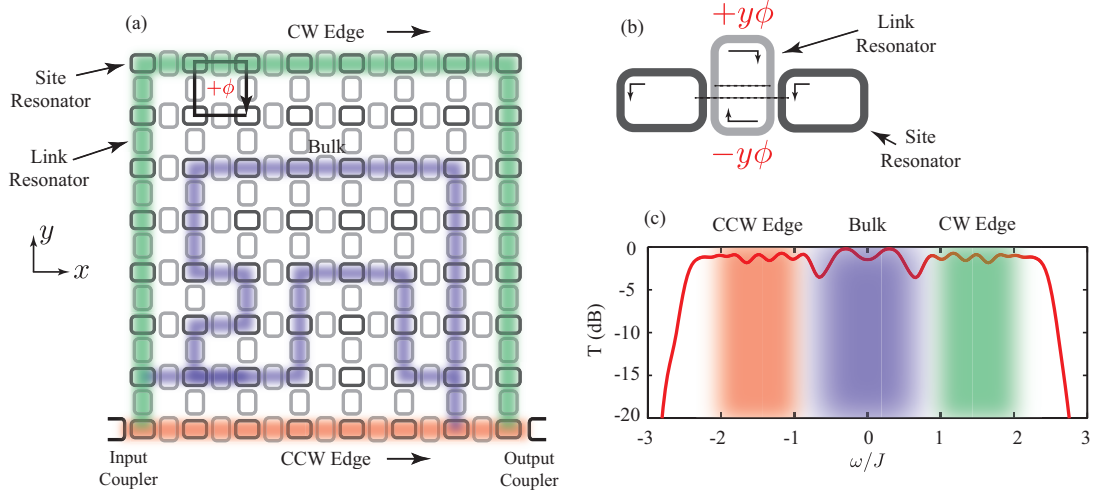


*Fig. 4.2:* (a) Schematic of a 2D lattice of coupled ring resonators implementing the integer quantum-Hall model. Site resonators (black) are coupled using link resonators (grey). The lattice is coupled to input and output waveguides. (b) A vertical shift of link resonator introduces direction dependent hopping phase and hence synthetic magnetic field for photons. Photons hopping along right experience a longer path and hence an extra phase compared to photons hopping along left. (c) Transmission spectrum (single-photon) for a pure  $8 \times 8$  lattice. CW, CCW Edge and bulk bands are shaded in green, red and blue, respectively.

the bulk states in the center of the band are susceptible to disorder. Using this feature, one could make delay lines using these topological devices which show less variability in transmission in presence of disorder. Further, when contrasted with delay lines constructed from 1D Coupled-Resonator Optical waveguides (CROW) which are collection of ring resonators which are coupled only in one direction, the average transmission falls at a lower rate as a function of number of rings [14].

## 4.5 Theory of entangled photons in the 2D lattice

The edge states of this system has been shown be robust under disorder for continuous wave excitation in [14]. We show that the integer quantum Hall device could also be used for quantum information by simulating the response for entangled states in the system [54]. We couple a generalised two photon input state

$$|\psi_{in}(t_e, t_l)\rangle = \int_{-\infty}^{\infty} \int_{-\infty}^{\infty} dt_1 dt_2 \psi_{in}(t_1, t_2; t_e, t_l) \hat{a}^\dagger(t_1) \hat{a}^\dagger(t_2) |0\rangle, \quad (4.11)$$

where  $t_e$  ( $t_l$ ) are the early (late) time bins in which the photons could arrive,  $\hat{a}^\dagger$  is photon creation operator and  $\psi_{in}(t_1, t_2; t_e, t_l)$  is the two-photon temporal wavefunction which is symmetric under exchange of photons.

We send in the corresponding bell states to check how the system behaves for these states in edge and bulk band. We derive that the output two-photon temporal wavefunction could be calculated by single photon temporal wavefunction at the output. We consider one of the bell states  $|\Psi^+\rangle$

$$\psi_{in}(t_1, t_2; t_e, t_l) = \frac{1}{\sqrt{2}} (\varphi_{in,1}(t_1 - t_e) \varphi_{in,2}(t_2 - t_l) + \varphi_{in,1}(t_1 - t_l) \varphi_{in,2}(t_2 - t_e)), \quad (4.12)$$

where  $\varphi_{in,i}(t_i - t_{e(l)})$  is the single-photon temporal wavefunction corresponding to the photon arriving in the early(late) time bin. Using 2D Fourier transform, the two-photon temporal wavefunction can be rewritten in frequency domain as

$$\psi_{in}(t_1, t_2; t_e, t_l) = \frac{1}{2\pi} \int_{-\infty}^{\infty} \int_{-\infty}^{\infty} d\omega_1 d\omega_2 \tilde{\psi}_{in}(\omega_1, \omega_2) e^{-i\omega_1 t_1} e^{-i\omega_2 t_2}, \quad (4.13)$$

where  $\tilde{\psi}_{in}(\omega_1, \omega_2)$  is the input two-photon spectral wavefunction. Using 4.12 and

4.13, we see that

$$\tilde{\psi}_{in}(\omega_1, \omega_2) = \tilde{\varphi}_{in,1}(\omega_1)\tilde{\varphi}_{in,2}(\omega_2) \left( e^{(i\omega_1 t_e + i\omega_2 t_l)} + e^{(i\omega_1 t_l + i\omega_2 t_e)} \right), \quad (4.14)$$

Since the Hamiltonian doesn't contain any non-linear terms, we can write the output wavefunction as

$$\begin{aligned} \tilde{\psi}_{out}(\omega_1, \omega_2) &= S(\omega_1) S(\omega_2) \tilde{\psi}_{in}(\omega_1, \omega_2) \\ &= \tilde{\varphi}_{out,1}(\omega_1)\tilde{\varphi}_{out,2}(\omega_2) \left( e^{(i\omega_1 t_e + i\omega_2 t_l)} + e^{(i\omega_1 t_l + i\omega_2 t_e)} \right), \end{aligned} \quad (4.15)$$

where  $S(\omega)$  is the transfer function for a single photon wavefunction at input frequency  $\omega$ .

$$\tilde{\varphi}_{out,i}(\omega) = S(\omega)\tilde{\varphi}_{in,i}(\omega), \quad (4.16)$$

This is calculated from input-output formalism described in [5]. Using inverse 2D fourier transform on 4.15, we see

$$\begin{aligned} \psi_{out}(t_1, t_2; t_e, t_l) &= \frac{1}{2\pi} \int_{-\infty}^{\infty} \int_{-\infty}^{\infty} d\omega_1 d\omega_2 \tilde{\psi}_{out}(\omega_1, \omega_2) e^{-i\omega_1 t_1} e^{-i\omega_2 t_2} \\ &= \frac{1}{\sqrt{2}} (\varphi_{out,1}(t_1 - t_e)\varphi_{out,2}(t_2 - t_l) + \varphi_{out,1}(t_1 - t_l)\varphi_{out,2}(t_2 - t_e)), \end{aligned} \quad (4.17)$$

where  $\varphi_{out,i}(t)$  is the inverse Fourier transform of  $\tilde{\varphi}_{out,i}(\omega)$ . Therefore, two-photon temporal wavefunction can be calculated using single temporal wavefunction for the above non-interacting hamiltonian. Similarly, derivation for other bell states could be also shown using above formalism.

We assume that the single photon input wavefunctions are gaussian which transforms the  $|\Psi^+\rangle$  as

$$\Psi^+(t_1, t_2; t_e, t_l) = e^{-\frac{(t_1 - t_e)^2}{2\sigma^2}} e^{-\frac{(t_2 - t_l)^2}{2\sigma^2}} + e^{-\frac{(t_1 - t_l)^2}{2\sigma^2}} e^{-\frac{(t_2 - t_e)^2}{2\sigma^2}}, \quad (4.18)$$

where  $\sigma$  is the pulse-width of a single photon temporal wavefunction. We take the time scale  $T_0$  to be inverse of the coupling rate  $T_0 = \frac{1}{J}$  and the corresponding pulse-width to be  $10T_0$ . The pulse-width is chosen such that we can resolve each band separately and study the underlying physics. The delay between the two photons is chosen be  $t_1 - t_e = 30T_0$  such that they are very well separated at the input. The correlation function is calculated using the probability of finding one photon at time  $t_1$  and other at  $t_2$  and is given by  $\Gamma(t_1, t_2) = |\psi(t_1, t_2)|^2$

#### 4.6 *Simulation Results of transport properties*

We first simulate the transport for a 8x8 lattice with no disorder. Figure 4.3 shows the input temporal correlation and at the output for both CW Edge and CCW Edge( $\omega = \pm 1.5J$ ) for  $\Psi^+$  and  $\Phi^+$  states. The output correlation functions have shifted by  $5T_0$  and  $16T_0$  diagonally for CCW and CW respectively, which depends on the length traversed through the lattice. We can also clearly see that the temporally correlations are perfectly preserved after the lattice for edge states.

To show that preservation of temporal correlations along edge states is non-trivial, we look at the correlation in the bulk band. Figure 4.4 shows that correlations for three different bulk band frequencies,  $\omega = (-.52, -.4, .52)J$  when the input is a  $\Psi^+$  state. We see that even though the photons are anti-bunched at the input, they become bunched at the output. This shows the quantum information is lost along this bulk band. We further contrast this with a separable two photon state whose temporal wavefunction is symmetrized. The separable state correspond-

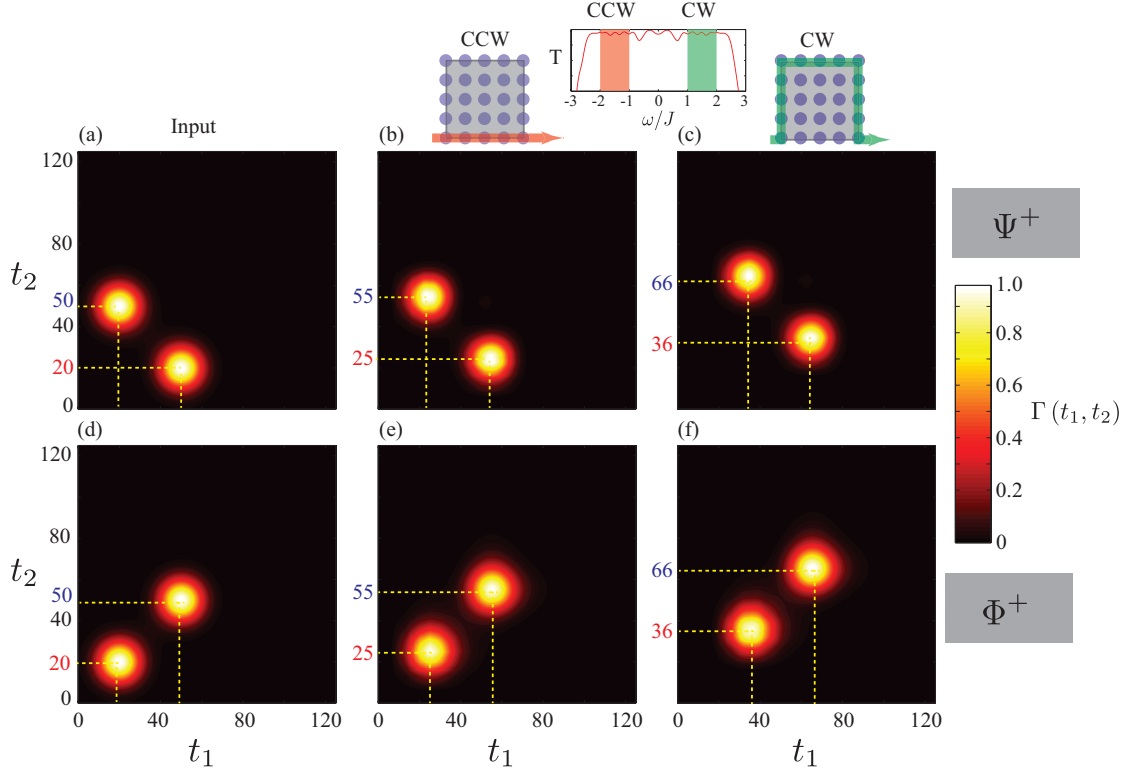
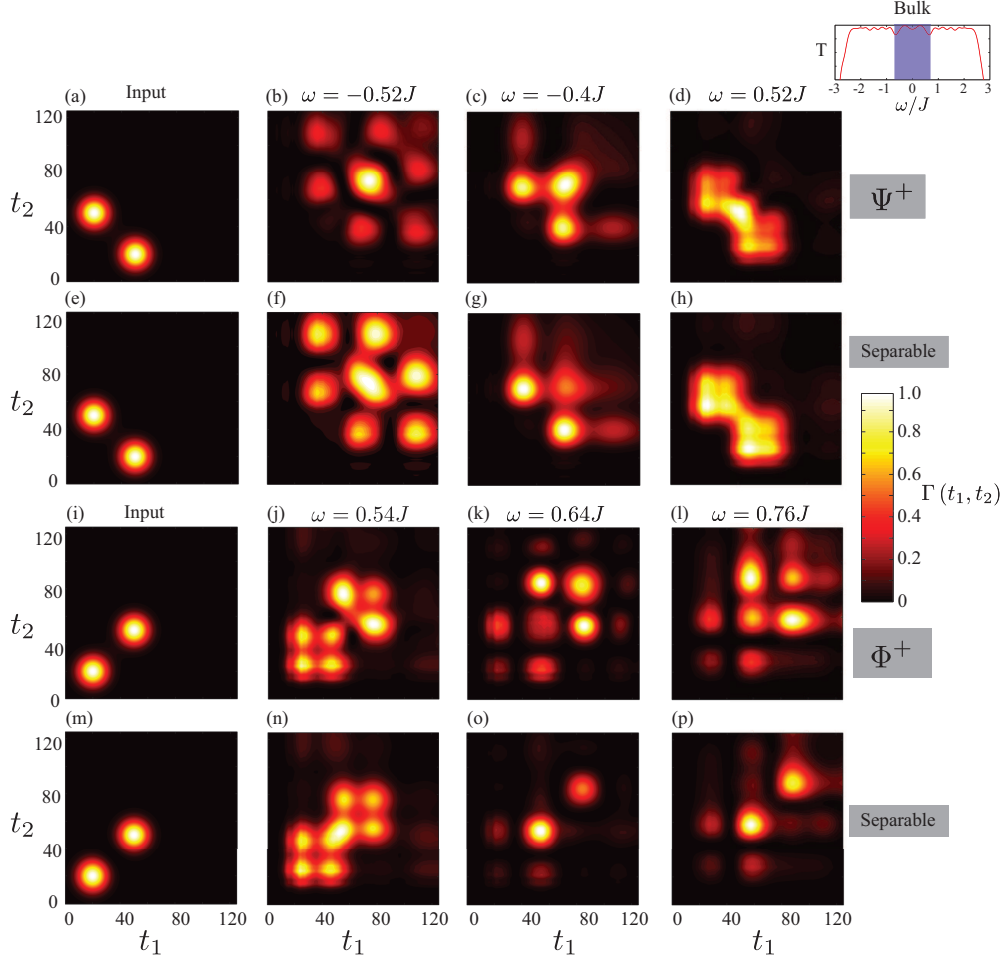


Fig. 4.3: (a) Time-correlation  $\Gamma(t_1, t_2)$  for  $\Psi^+$  input state, with  $\sigma = 10 T_0$  and delay  $\tau = 30 T_0$ , where  $T_0 = 1/J$ . (b,c) Simulated correlation function at the output port of a 8x8 lattice for CCW and CW edge states, respectively. The centres of the two time-bins are marked with dashed yellow lines. (d-f) Results for the input state  $\Phi^+$ . Insets show the transmission spectrum and the path followed by edge states.  $\Gamma(t_1, t_2)$  is normalized such that the maximum is unity.

ing to  $\Psi^+$  is given by  $\psi(t_1, t_2; t_e, t_l) = \varphi_1(t_1 - t_e) \varphi_2(t_2 - t_l)$ , where  $\varphi_i(t_i)$  is the single-photon temporal wavefunction. To contrast the entangled photon transport, we symmetrize the two-photon correlation function for separable state as

$$\Gamma(t_1, t_2) = \frac{1}{2} (|\varphi_1(t_1 - t_e) \varphi_2(t_2 - t_l)|^2 + |\varphi_1(t_1 - t_l) \varphi_2(t_2 - t_e)|^2), \quad (4.19)$$

We can see in Fig. 4.4 that bunching for entangled state is much more



*Fig. 4.4:* (a-d) Time-correlation function at the input and the output of the lattice for  $\Psi^+$  state and three different input frequencies in the bulk band,  $\omega = (-0.52, -0.4, 0.52)J$ . (e-h) Correlation for the separable state corresponding to the input frequencies in (a-d). (i-p) Simulation results for  $\Phi^+$  and the corresponding separable state.

prominent compared to a symmetrized separable state. Similar plots for  $\Phi^+$  state are also shown in which case anti-bunching occurs for bunched photons. In both cases, we see that entangled states are more susceptible to fluctuations compared a separable state.

#### 4.7 *Transport in presence of disorder*

Transport of classical light has been shown to robust in the 2D lattice when compared to 1D CROW [14]. Here, we simulate non-classical light in the lattice with disorder. The most significant disorder in a 1D lattice is ring resonance mismatch( $\Delta\omega_0$ ), hence we use on-site potential  $V$  to specify disorder. We plot results only for  $\Psi^+$  as  $\Phi^+$  follows a similar pattern with bunching and anti-bunching terms exchanged. Figure 4.5 shows the temporal correlations for  $\Psi^+$  in edge and bulk bands for disorder strengths  $V = (.2, .4, .6, .8)J$ . The simulations are averaged over the corresponding bands and over 100 devices.

The correlations in edge bands are much robust under disorder compared to bulk bands. We can also see that the CW Edge is more susceptible to disorder compared to CCW Edge since it travels through a longer path. There is some bunching observed in the edge states for higher disorder strength  $V > .6J$ , which is due to the reduced bandwidth at large disorder. Bulk states on the other hand are prone to disorder even for a small disorder  $V = .2J$ .

We quantify the bunching of photons at the output using a normalized prob-



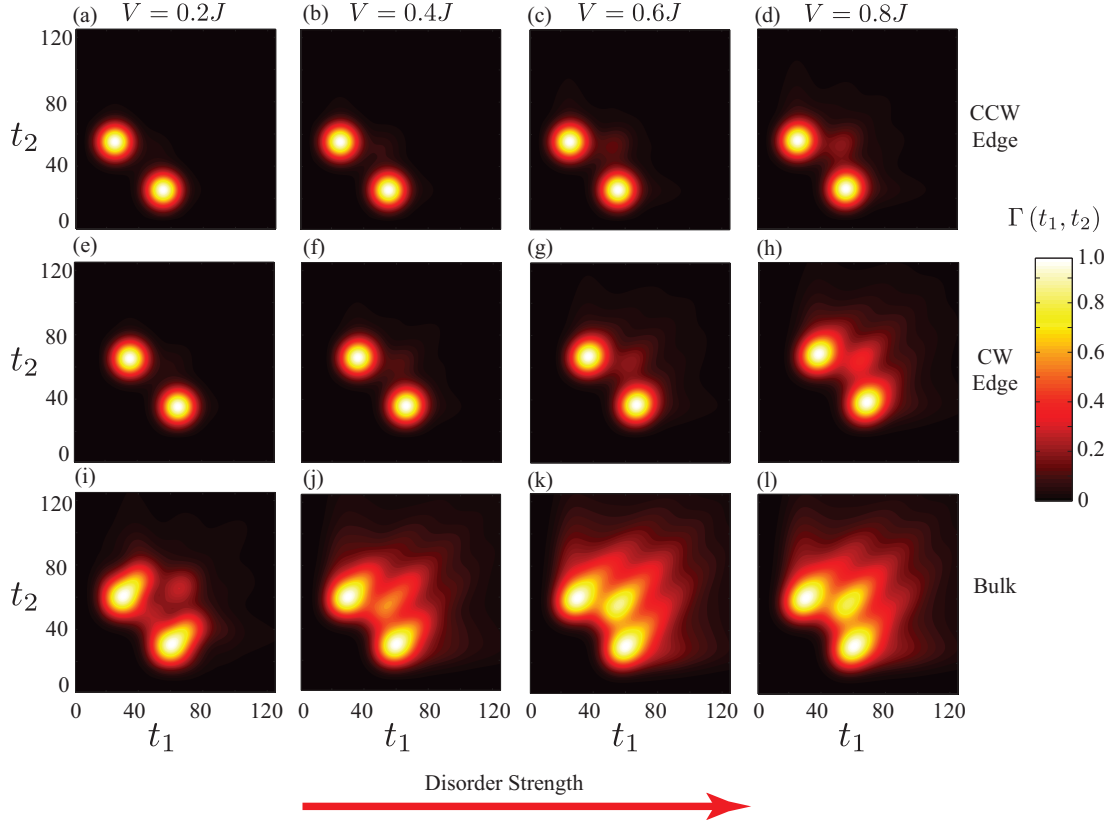


Fig. 4.5: Correlation function at the output of a disordered system, for  $\Psi^+$  input excitation in the (a-d) CCW edge band, (e-h) CW edge band and (i-l) for bulk band; for four different disorder strengths.

ability of bunching for a  $\Psi^+$  state which is given by

$$P_B = \frac{\int_{-\infty}^{\infty} \int_{-\infty}^{\infty} dt_1 dt_2 \delta(t_2 - t_1 \pm \tau) \Gamma(t_1, t_2)}{\int_{-\infty}^{\infty} \int_{-\infty}^{\infty} dt_1 dt_2 \Gamma(t_1, t_2)}, \quad (4.20)$$

where bunching of photons occurs in a  $\tau = \sigma/2$  time window. Figure 4.6(a) shows that  $P_B$  as a function of disorder strength. The probability of bunching for edge states is much lower compared to bulk states and also the bunching probability increases with disorder. We also look at another figure of merit which is the similarity of the output correlation with respect to the input correlation.

$$S = \text{MAX}_{i \in \text{shifts}} \left\{ \frac{\left( \int_{-\infty}^{\infty} \int_{-\infty}^{\infty} dt_1 dt_2 \sqrt{\Gamma_{out,i}(t_1, t_2) \Gamma_{in}(t_1, t_2)} \right)^2}{\int_{-\infty}^{\infty} \int_{-\infty}^{\infty} dt_1 dt_2 \Gamma_{out,i}(t_1, t_2) \int_{-\infty}^{\infty} \int_{-\infty}^{\infty} dt_1 dt_2 \Gamma_{in}(t_1, t_2)} \right\}, \quad (4.21)$$

where  $\Gamma_{in}$  is the input correlation function at the input and  $\Gamma_{out,i}$  is shifted output correlations along the diagonal with a value  $i$ . Maximum similarity is obtained when the output spectrum has maximum overlap with the input function. Figure 4.6(b) shows that  $S$  as a function of disorder strength. The similarity for edge states is higher compared to bulk which is as expected from theory.

## 4.8 Summary and experimental Progress

In this chapter, we showed that temporal correlations of entangled states are preserved when transported through edge states. This is in contrast with bulk states where the correlations are distorted and can result in bunching/anti-bunching. One of the major challenges in realizing the quantum transport experiment is the inability to resolve temporal correlations due to jitter of the single photon detectors. The photons have to be delayed by  $< 50$  ps (longest delay in the lattice) for them to

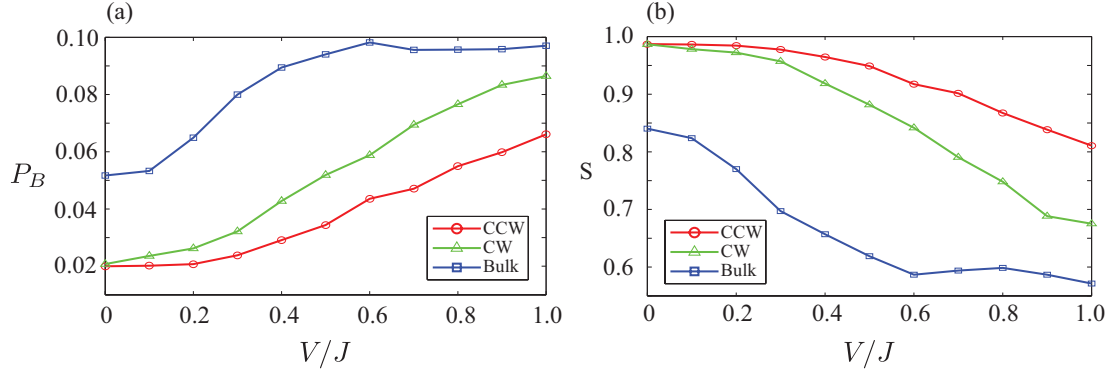


Fig. 4.6: (a) Calculated probability of bunching for  $\Psi^+$  input state, with excitation in the edge and the bulk bands, as a function of disorder. (b) Similarity between the input and the output correlation.

interact in the lattice. However, the timing jitter of the single photon detectors were  $\approx 100$  ps. In addition, the loss in the system is of the order 25dB, which translates into an effective loss of 50dB for coincidence measurements. To solve these challenges, we have developed a few experimental techniques in quantum optics which are described in the next chapters.

## Chapter 5: Temporal and Spectral manipulation of correlated photons using Time-lens

### 5.1 Introduction

Entangled photons are one of the most frequently used sources in quantum information [55, 56]. Hence, spectral and temporal manipulation of these entangled photons play a vital role in quantum optics. Usually, the single photon detectors used in these experiments are too small to resolve the features in a single photon wavepacket. Using the technique of time-lens, one could spectrally compress the bandwidth of the photons and magnify these temporal features [57]. Time-lens techniques has been previously used in classic light waves and demonstrated recently for single photons [58, 59].

In this chapter, we use an Electro-Optic Modulator (EOM) based time-lens to magnify and measure the two photon wavefunction of time-bin entangled photons while preserving their quantum correlations. Though other methods of resolving these correlations exist, such as time-resolved frequency upconversion [60] and intensity modulation [61], they are very slow because they require a two-dimensional scan of a narrow filter in time/frequency. Our scheme allows for measurement of

Joint Temporal Intensity (JTI) without any filtering and enables a single shot measurement of JTI [62]. Our time-lens is designed to work in the telecom domain and achieves a temporal magnification of 9.6(2)x. Using the magnification, we measure JTI of two-photon states with a delay much less than the resolution of superconducting nanowire single photon detectors (SNSPDs). Furthermore, we show that the time-lens maps temporal correlations of incoming photons to frequency correlations of outgoing photons and can be used to manipulate frequency-bin entangled two-photon states [63].

## 5.2 Time-lens setup

Fig. 5.1 shows the time-lens setup. The time-lens consists of three elements 1. Input dispersive element, 2. EOM 3. Output dispersive element. The three parameters corresponds to object distance, focal length and image distance in their equivalent spatial domain. The input dispersive element with a group delay dispersion (GDD)  $\phi_i'' = \frac{d^2\phi_i(\omega)}{d\omega^2}$  chirps the input photon pulses spectrally. where  $\omega$  is the angular frequency and  $\phi_i(\omega)$  is the frequency dependent phase-shift accumulated during propagation. The EOM driven by an rf field acts as a time-lens introducing a quadrature time varying phase  $\phi_l(t) = \frac{\pi V_m \omega_m^2}{2V_\pi} t^2$ , when the photon time arrival is locked in phase with the rf. Where,  $\omega_m$ ,  $V_m$  are the modulation frequency and amplitude of the rf drive and  $V_\pi$  is the  $\pi$  phase-shift voltage. The GDD  $\phi_l'' = \frac{V_\pi}{\pi V_m \omega_m^2}$  of the time-lens introduces a frequency shift between the photons which is given by

$$\delta\nu = \frac{V_m \omega_m^2}{V_\pi} \frac{\omega_m^2}{2} \delta_{\text{in}}. \quad (5.1)$$

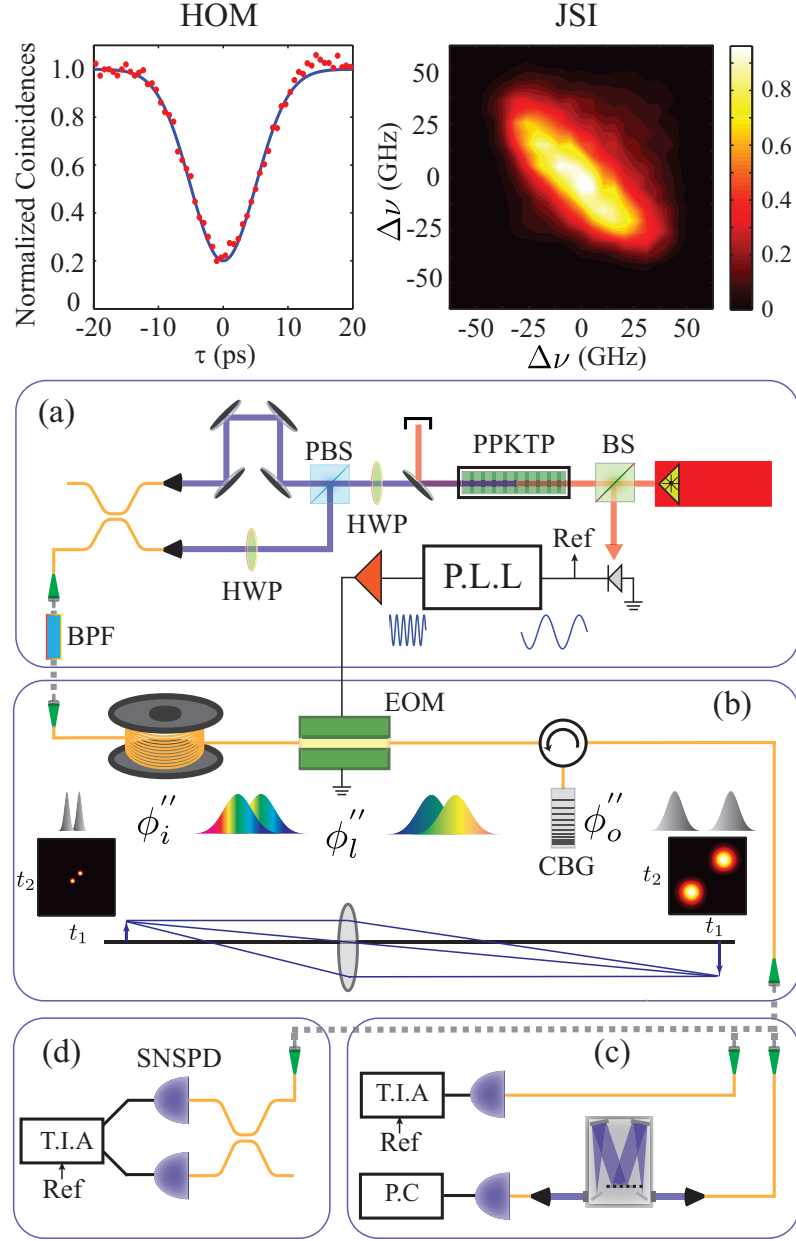


Fig. 5.1: (a) Experimental setup of time-lens half-wave plate (HWP), polarization beam-splitter (PBS), electro-optic phase modulator (EOM). Insets show the measured HOM interference with a visibility of  $\approx 80\%$  and nearly symmetric JSI, after the bandpass filter (BPF).

where  $\delta_{\text{in}}$  is the input time delay between the photons. The time information is mapped into frequency domain similar to that of spatial lens, where position is mapped into momentum. Lastly, a large GDD output dispersive element converts the frequency shifts into differential delay  $2\pi\delta\nu\phi_o''$  resulting in delay between the output photons  $\delta_{\text{out}}$  given by,

$$\delta_{\text{out}} = \delta_{\text{in}} + \frac{\pi V_m}{V_\pi} \omega_m^2 \phi_o'' \delta_{\text{in}}. \quad (5.2)$$

When the time-lens equivalent lens-equation is satisfied  $-\frac{1}{\phi_l''} = \frac{1}{\phi_i''} + \frac{1}{\phi_o''}$ , the input photons experience a temporal magnification given by  $M = \frac{\delta_{\text{out}}}{\delta_{\text{in}}} = -\frac{\phi_o''}{\phi_i''}$ . The time-lens similar to spatial lens has a limited aperture which is given by  $\tau_a \approx \frac{1}{\omega_m}$  and hence can be used only pulsed-light sources.

Our experiment is designed to produce a magnification,  $M \approx 9.8\times$ . The initial dispersive element is a 15 km spool of SMF-28 fiber with  $\text{GDD} = -326 \text{ ps}^2$  and output dispersion is achieved through a Chirped-bragg grating(CBG) with  $\text{GDD} = -3190 \text{ ps}^2$ . The EOM was driven by a rf signal with frequency  $\nu_m = \frac{\omega_m}{2\pi} = 2.786 \text{ GHz}$  and was locked to the Ti-Sapphire laser. The  $\pi$ -phase-shift voltage  $V_\pi$  of the modulator was measured to be 3.49(6) V, at 2.786 GHz. The rf signal amplitude  $V_m$  was set to 12.3 V so that the GDD introduced by the EOM is  $-326 \text{ ps}^2$  and satisfies the time-lens equation. The corresponding signs of the GDD lead to a converging lens [57].

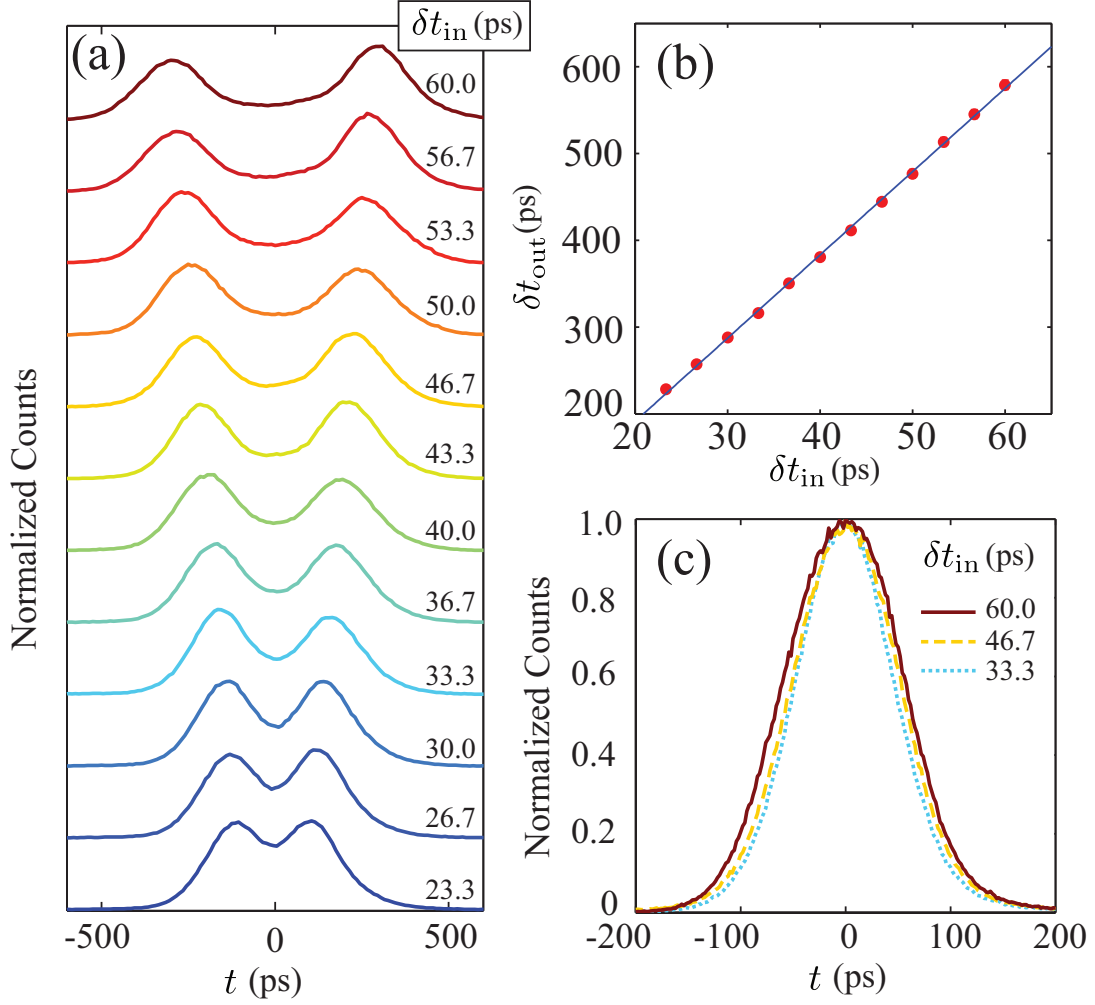


Fig. 5.2: (a) Observed photon pulses after the time-lens, for different input time delays  $\delta t_{\text{in}}$ . (b) Measured delay (red markers) between photons at the output of the lens as a function of delay at the input. The delay increases linearly, with a slope  $M = 9.6(2)$  where the uncertainty is from the linear fit (blue solid line). The size of the errorbars, representing statistical error in finding peaks of photon pulses, is less than the size of markers. (c) Output pulses without the time-lens



### 5.3 Temporal Magnification of photons

In order to test the magnification of the lens, we send two photons with input delays between 20-60 ps less than the detector jitter of 100 ps.  $\delta_{\text{in}} = t_l - t_e$  where,  $t_e$  and  $t_l$  are time of arrival of photon in early time-bin and late time-bin. A periodically-poled potassium titanyl phosphate (PPKTP) crystal (30 mm length) is pumped using a pulsed ( $\approx 1.6$  ps) Ti-Sapphire laser ( $\approx 775$  nm) which generates orthogonally polarized, spectrally-degenerate photon pairs at telecom wavelengths via Type-II collinear spontaneous parametric down-conversion (SPDC). We separate the two orthogonally polarized photons using a polarization beam-splitter (PBS) and introduce a relative delay  $\delta_{\text{in}}$  between them. We rotate the polarization in one of the arms such that the two photons are identically polarized and collect them into a single fiber using a beam-splitter. The photons are filtered through narrow band filter of  $\approx 75$  GHz (0.6 nm) FWHM and sent into time-lens. The photon pulsewidth is measured to be 16.7(7) ps using Hong-Ou-Mandel(HOM) interference before the time-lens. The photons at the output of the time-lens are then detected using a superconducting nanowire detectors (SNSPDs) and the timing information is collected through a time-interval analyzer (TIA)(Fig. 5.1(c)).

Figure 5.2(a) shows the output photon pulses at the output of the lens for different input delays. The lowest delay we could resolve is a separation of 23 ps which is consistent with estimated time resolution, which is the ratio of focal length to the aperture of the lens,  $\delta t_0 = \frac{2V_\pi}{V_m \omega_m} \approx 30$  ps. The output delay is plotted as a function of input delay and estimated magnification  $M$  given by the slope to

be 9.6(2), which is close to the design parameter of  $M = 9.8$  (Fig. 5.2(b)). The discrepancy is due to the overfilling of aperture for higher  $\delta_{\text{in}}$ . The estimated output of the photon pulse-width is 186(1) ps given the input pulse-width is 16.7(7) ps. Fig. 5.2(c) shows contrasted output of detectors without time-lens which shows that the photons are un-resolved.

#### 5.4 Temporal Correlations of photons

JTI is useful in measurements of two-photon states where single channel delay measurements cannot distinguish them. One example is to distinguish between a bunched and an anti-bunched state. In the bunched state ( $|2_e, 0_l\rangle - |0_e, 2_l\rangle$ ), both the photons arrive in the *early* time-bin or both in the *late* time-bin. In the anti-bunched state ( $|1_e, 1_l\rangle$ ), one photon arrives early and the other late. Single channel spectrum would show two peaks at early and late time-bin for both the states, where as JTI would be distinguishable. JTI is the probability of two photons, one at time  $t_1$  and the other at  $t_2$ , and is defined as  $|\psi(t_1, t_2)|^2$  where  $\psi(t_1, t_2)$  is the two-photon temporal wavefunction. JTI is measured using a beam splitter and two detectors where the measurements are limited by jitter of the detectors. By using a time-lens technique, we show that temporal correlations could be accessed with resolutions smaller than the detector jitter. Even though JTI doesn't measure the phase of the wavefunction, it is still useful in many quantum applications like quantum walks [54, 64], boson sampling [32, 65, 66] which only require intensity measurements.

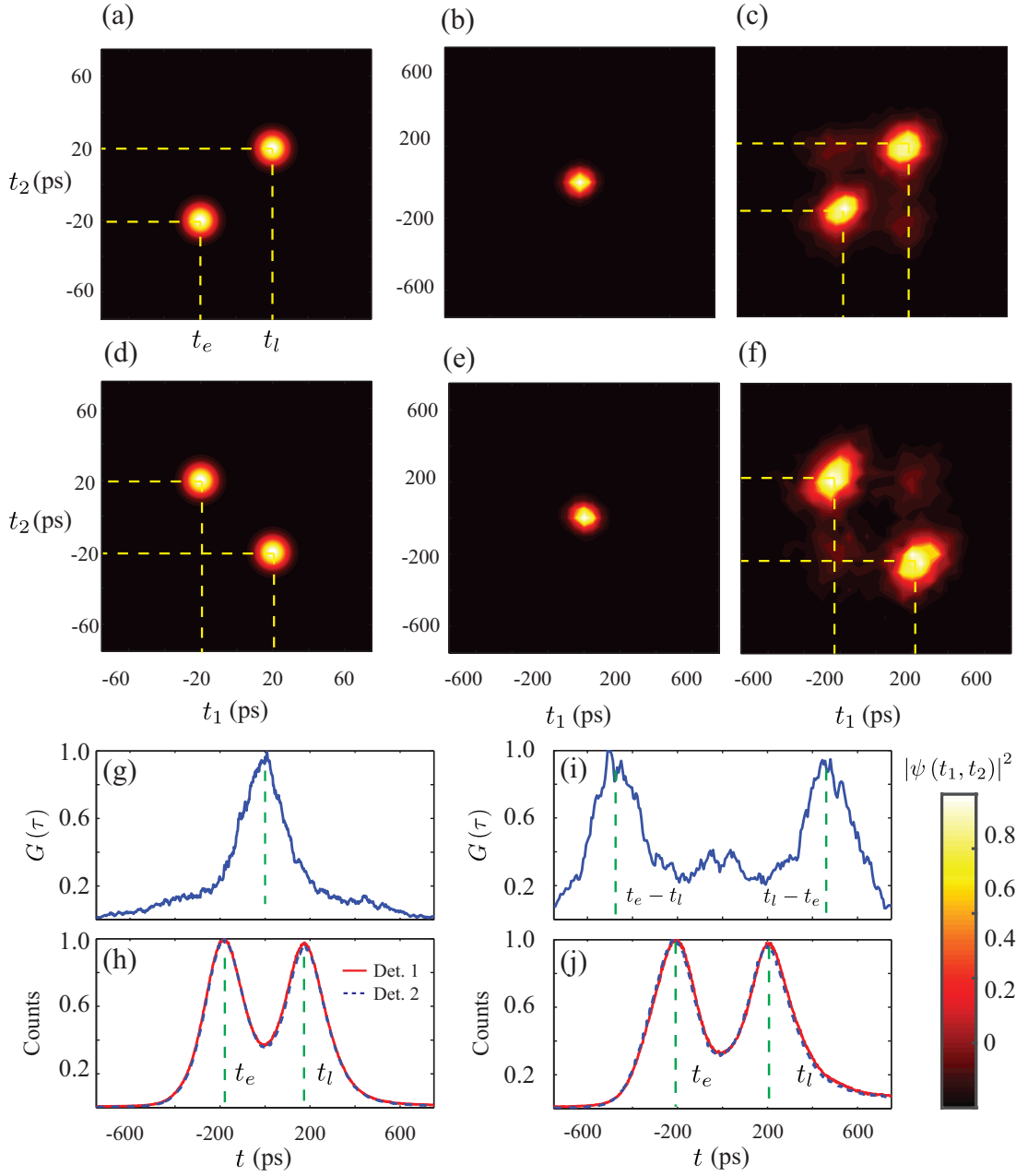


Fig. 5.3: (a) Simulated JTI of the bunched two-photon state before the time-lens. (b) Measured JTI, without the time-lens. (c) Measured JTI with the time-lens. (g) Measured  $G(\tau)$  peaks at  $\tau = 0$ , consistent with bunched behavior. (h) Measured singles counts on two detectors. (d)-(f) Corresponding results for the anti-bunched state. (i-j)  $G(\tau)$  now peaks at  $\tau = \pm(t_e - t_l) \approx 420$  ps, showing anti-bunched photons.

We generate two-photon states which are bunched and anti-bunched using a HWP after the SPDC. When the HWP is set to  $22.5^\circ$ , it acts a 50:50 beam-splitter for the H and V photons and produces a two-photon state.

$$\begin{aligned}
|\Psi\rangle = \iint d\omega_1 d\omega_2 \tilde{\psi}(\omega_1, \omega_2) [ & \hat{a}_H^\dagger(\omega_1) \hat{a}_H^\dagger(\omega_2) + \\
& \hat{a}_V^\dagger(\omega_1) \hat{a}_H^\dagger(\omega_2) - \hat{a}_H^\dagger(\omega_1) \hat{a}_V^\dagger(\omega_2) - \\
& \hat{a}_V^\dagger(\omega_1) \hat{a}_V^\dagger(\omega_2) ] |0\rangle, \tag{5.3}
\end{aligned}$$

If the two-photon wavefunction is symmetric  $\tilde{\psi}(\omega_1, \omega_2) = \tilde{\psi}(\omega_2, \omega_1)$ , it generates a polarization entangled state where the photons are bunched

$$\begin{aligned}
|\Psi\rangle = \iint d\omega_1 d\omega_2 \tilde{\psi}(\omega_1, \omega_2) [ & \hat{a}_H^\dagger(\omega_1) \hat{a}_H^\dagger(\omega_2) - \\
& \hat{a}_V^\dagger(\omega_1) \hat{a}_V^\dagger(\omega_2) ] |0\rangle, \tag{5.4}
\end{aligned}$$

We realize this by using a bandpass filter of .6 nm centered at 1550.965 nm. Transforming the two-photon wavefunction in time-domain after passing through another HWP and a delay line produces a time-bin entangled state where both the photons come early or both the photons late and is given by,

$$\begin{aligned}
|\Psi_B\rangle = \iint dt_1 dt_2 \psi(t_1, t_2) [ & \hat{a}^\dagger(t_1 - t_e) \hat{a}^\dagger(t_2 - t_e) - \\
& e^{i2\varphi} \hat{a}^\dagger(t_1 - t_l) \hat{a}^\dagger(t_2 - t_l) ] |0\rangle, \tag{5.5}
\end{aligned}$$

Figure 5.3(a) shows the simulated JTI for the bunched states where the input pulses are gaussian. The symmetric nature of the wavefunction is verified using HOM which showed a visibility of  $\approx 80\%$ . We also confirmed the exchange symmetry of the two-photon wavefunction by measuring the JSI of two photons using chirped

Bragg grating as a frequency-to-time converter as shown in Fig. 5.1. When we set the HWP to zero, it generates an product state in polarization and after converting the polarization domain into time generates at two-photon product state in time which is given by

$$|\Psi_{AB}\rangle = \int \int dt_1 dt_2 \psi(t_1 - t_e, t_2 - t_l) a^\dagger(t_1 - t_e) a^\dagger(t_2 - t_l) |0\rangle.$$

When this state is passed through a beam splitter needed for measuring JTI, it generates a time-bin entangled state as the detectors cannot distinguish between the two photons. Fig. 5.3(b,c) show the measured JTI without and with a time-lens for a bunched state  $|\Psi_B\rangle$ . Fig. 5.3(g,h) show the measured JTI without and with a time-lens for a anti-bunched state  $|\Psi_{AB}\rangle$ . The delay with between the photons is set to 40 ps, less than that of the detector jitter. We can clearly see that the temporal correlations which were otherwise inaccessible are measured by using a time-lens and there is good fidelity between input and output states. There is a small probability of photons in time-bins diagonal to that of expected, which is due to the multi-photon process in SPDC. The measured delay between the photons is about 360 ps which is consistent with the magnification.

To quantify the correlation measurement, we look at probability of photons  $G(\tau)$  arriving with a time difference,  $\tau$

$$G(\tau) = \int \int dt_1 dt_2 |\Psi(t_1, t_2)|^2 \delta(\tau - t_1 + t_2). \quad (5.6)$$

As can be seen from Fig. 5.3(d,i),  $G(\tau)$  for  $|\Psi_B\rangle$  peaks at  $\tau = 0$  verifying that the photons are bunched and  $G(\tau)$  for  $|\Psi_{AB}\rangle$  shows two peaks at  $\tau \approx t_l - t_e$ . We also plot single channel measurements in Fig. 5.3(e,j) for bunched and anti-bunched states

and show that these measurements cannot distinguish the corresponding two-photon states.

## 5.5 Spectral Correlation Measurements

The time-lens in our setup also maps the temporal correlation of the input photons into spectral correlations of output photons. The EOM introduces frequency shifts  $\delta\nu$  for input delays which are mapped to time using a CBG. The CBG acts a frequency to time mapper irrespective of the time-lens equation and timing information from TIA gives the corresponding frequency shifts. We independently measure the frequency shifts of output photons using a monochromator. Fig. 5.4(a) shows measured spectrum for different input delays. Fig. 5.4(b) plots the frequency shifts as function of delay and the measure slope is .60(8) which fits well with estimated .54 from (5.1). We also see a spectral compression of the single-photon spectrum after the time-lens compared to before timelens in Fig. 5.4(c) and observe a compression factor of 8.3x.

## 5.6 Coherence of Time-lens

In order to show that the time-lens preserves quantum states, it is necessary for the phase  $\theta$  to be also preserved when a quantum state passes through time-lens. Standard Franson interferometer to estimate the phase would not work, as both the early and late photons acquire different frequency shifts after the time-lens. We use a modified Franson interferometer setup to show the coherence of the time-lens. We

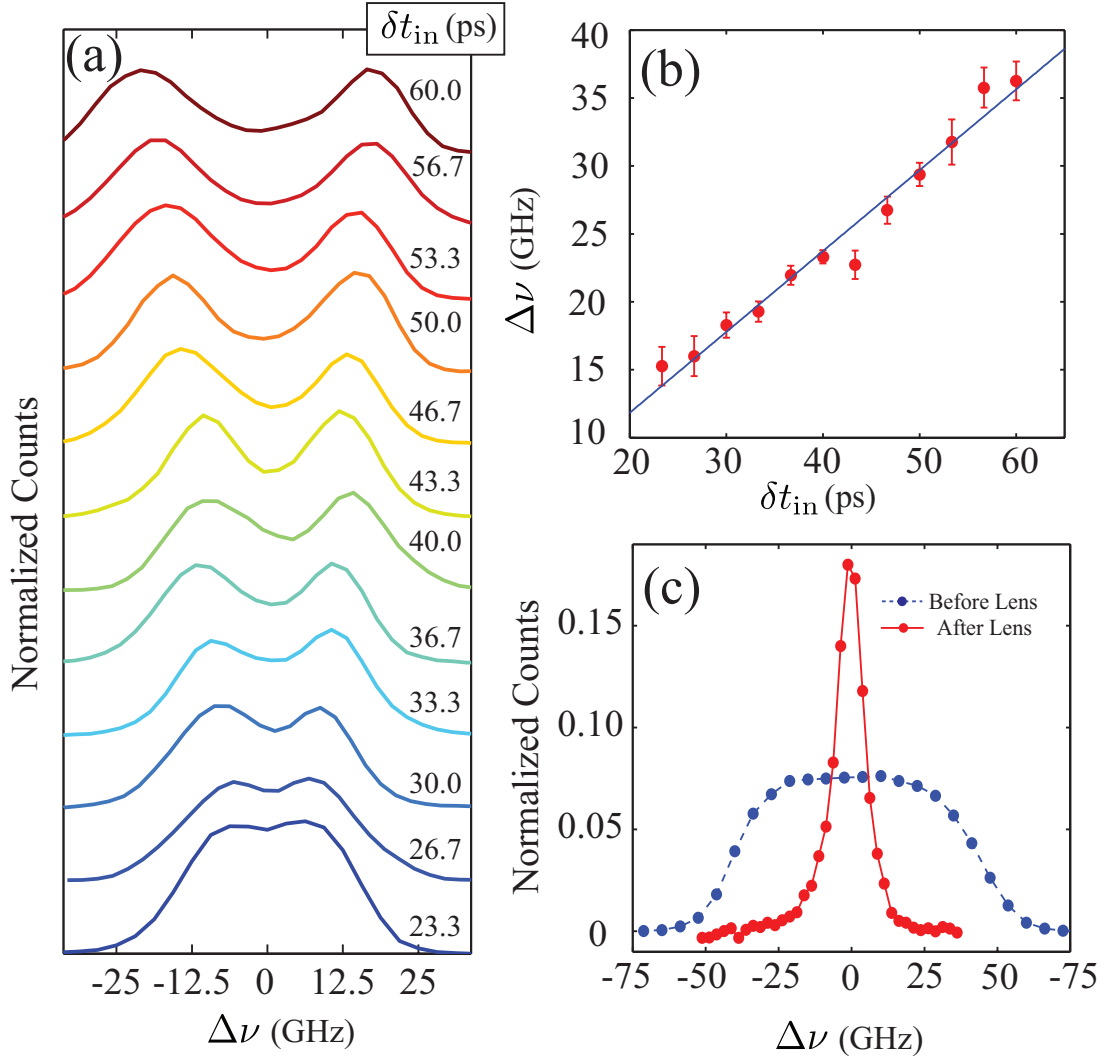


Fig. 5.4: (a) Measured spectrum of photon pulses, for different input delay  $\delta_{\text{in}}$ . (b) Relative frequency shift as a function of input delay  $\delta_{\text{in}}$ . (c) Measured spectral profile before the time-lens (FWHM  $\sim 75$  GHz) and after the time-lens (FWHM  $\sim 9$  GHz, corrected for monochromator bandwidth of 8.2GHz) gives a spectral compression factor of  $\approx 8.3\times$ .

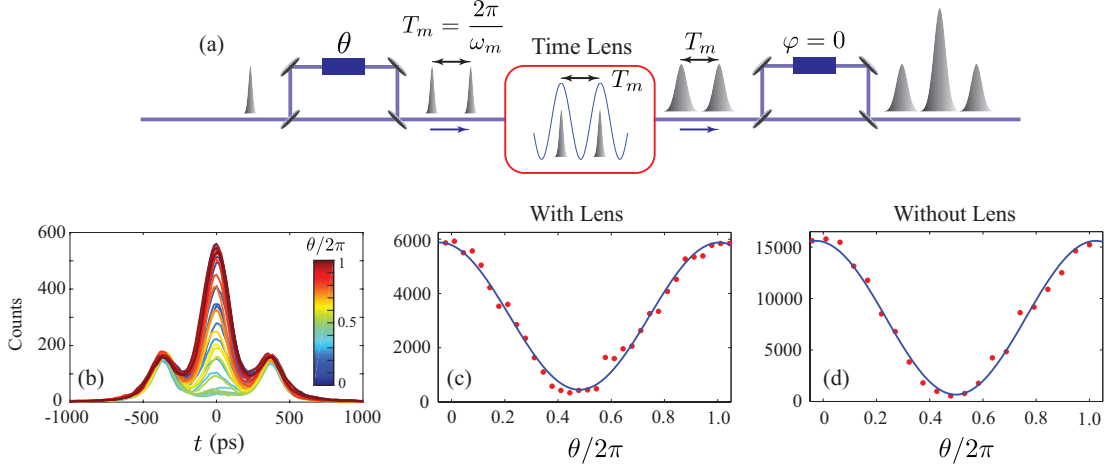


Fig. 5.5: (a), Setup used to test coherence of the time-lens. (b), Observed signal at the output for different values of phase  $\theta$ . (c) Intensity of the middle peak as a function of phase  $\theta$ . The intensity varies as  $\cos(\theta - \varphi)$ , where  $\varphi$  is the phase associated with the output interferometer. (d), Intensity of the middle peak as a function of  $\theta$ , without a time-lens.

prepare a single photon in a superposition of early and late time-bins with a relative phase  $\theta$ ,  $|e\rangle + e^{i\theta} |l\rangle$ . The early and late time-bins are separated by the period ( $\approx 360$  ps) of the rf drive chosen such that both the photons experience the same frequency shift (Fig. 5.5(a)). Effectively, early photons and late photons experience different time-lenses with the same magnification. Now, a Franson interferometer can be used to measure the relative phase  $\theta$  between the photons.

Figure 5.5(b) shows the temporal response at the output of the detector for different phases of  $\theta$  and fixed phase  $\varphi = 0$  of the output interferometer. The first the third peaks corresponds to interference of early photons taking early path and late photons taking late path. The middle peak shows the interference between early photons taking late path and late photons taking early path. The intensity of the



middle peak varies as  $\cos(\theta - \varphi)$  and agree with measurement in Fig. 5.5(c). We see an interference visibility of 83 %. Furthermore, we are able to resolve the interference fringes without time-lens since the photons are separated by larger than detector jitter. Fig. 5.5(d) shows the interference without time-lens with a visibility of 93 %. The temporal magnification of the time-lens reduces slightly the orthogonality of the time-bins and shows a small reduction in interference visibility.

## 5.7 Summary

In this chapter, we realized an EOM based time-lens technique to resolve temporal and spectral correlations of time-bin entangled photons, which would have otherwise been inaccessible due to limited detector resolution. This technique could enable picosecond scale temporal resolutions using existing single photon detectors for use in quantum communications.

## Chapter 6: Interference of temporally distinguishable photons using frequency-resolved detection

### 6.1 Introduction

The nonclassical interference of two or more photons in an optical network is the fundamental phenomenon enabling many algorithms used in linear optics quantum computing [56, 67–69], quantum communications [30, 70, 71], metrology [28, 72] and boson sampling [32, 33, 73]. Quantum interference, such as, Hong-Ou-Mandel (HOM) and Shih-Alley interference [47, 74], usually require photons which are identical in their temporal and spectral degrees of freedom. Any distinguishability in the photons at the detectors leads to a reduction in the interference. The difficulty in experimentally generating identical photons has prompted strong interest in developing “real world” optical networks enabling interference of nonidentical photons [75, 76]. Recently, it was shown that non-classical interference can be observed between photons completely distinguishable in time or frequency by exploiting correlation measurements in the corresponding conjugate parameter [77–81]. Remarkably, the interference can occur for any values of the input frequencies (or times) as long as the detector resolution in the conjugate parameter is sufficient to make

the detectors ‘blind’ to the spectral (or temporal, respectively) distinguishability of the photons. Furthermore, the temporal/spectral distinguishability can actually be used as a resource, for example, to reveal spectral properties of the input photons and the symmetries of the optical network [79, 80].

Many experiments have demonstrated interference of two photons that are distinguishable in frequency or time by resolving them in the conjugate parameter [77, 78, 82, 83]. Scaling these spectrally/temporally resolved interference phenomena to a larger number of photons can enable, for example, multi-boson correlation sampling experiments where sampling over temporal/spectral modes, in addition to spatial modes, can relax the requirements on generating identical photons and could demonstrate quantum supremacy [84–87]. Indeed, time-resolved interference of three photons with different frequencies was demonstrated very recently where the temporal correlations between detected photons were manipulated using a spatial network of beam-splitters [81]. In contrast, the complementary phenomenon, that is, frequency-resolved interference of multiple photons that are separated in time, allows convenient manipulations of spectral correlations by tuning the relative delays between photons, without reconfiguring the spatial network [80, 87]. This scheme can operate in a single spatial (transverse) mode and, therefore, enable the realization of scalable temporal boson sampling using time-varying dispersion [66]. However, such frequency-resolved interference of more than two photons has not yet been demonstrated.

Here, we demonstrate frequency-resolved quantum interference of three photons that are completely distinguishable in time [88]. We show that the interference

observed in the spectral correlations of detected photons can be manipulated by changing the relative delays between the photons at the input. The interference is completely wiped out for longer delays between photons, that is when the spectral resolution of the detectors is not sufficient to erase the temporal distinguishability of the photons. Moreover, we observe that the symmetries of the optical network and the spectral wavefunctions of photons are reflected in the measured spectral correlations. Finally, we also demonstrate spectral correlations in inverse-HOM interference using two time-bin entangled photons where both photons arrive either “early” or “late” [41]. In this case, we observe that the interference is sensitive to the phase between the two components of the entangled state, unlike the case of unentangled photons where interference is insensitive to small fluctuations in delay between the photons. Our experimental setup could easily be extended to introduce time-varying dispersion using phase modulators and realize the temporal boson sampling scheme of Ref. [66].

## 6.2 Two-photon frequency-resolved detection

To demonstrate our scheme, we discuss first the interference of two temporally distinguishable photons in our setup (Fig. 6.1). The two-photon interference can be analyzed using the spectral correlation function  $\Gamma(\omega_1, \omega_2, \tau)$ , which is the probability of detecting two photons at the two detectors, with frequencies  $\omega_1$  and  $\omega_2$ , respectively and  $\tau = t_2 - t_1$  is the relative delay between photons at the input. The

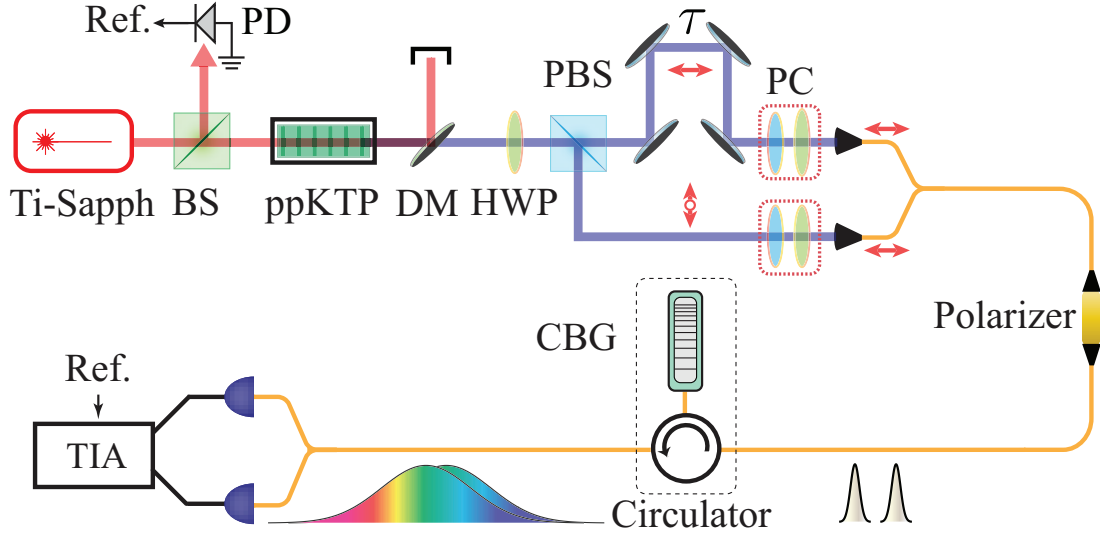


Fig. 6.1: Schematic of the experimental setup to observe frequency-resolved interference of two photons with a relative delay  $\tau$ . PBS: Polarization beam-splitter, CBG: chirped Bragg grating, TIA: time-interval analyzer, HWP: half-wave plate, PC: polarization controller, PD: photo-diode.

correlation function in our setup is given by [82, 83],

$$\Gamma(\omega_1, \omega_2, \tau) = \left| \psi_1(\omega_1) \psi_2(\omega_2) e^{-i(\omega_1 t_1 + \omega_2 t_2)} + \psi_1(\omega_2) \psi_2(\omega_1) e^{-i(\omega_2 t_1 + \omega_1 t_2)} \right|^2, \quad (6.1)$$

where  $\psi_{1(2)}(\omega)$  is the spectral wavefunction of the first (second) photon. The spectral correlation function depends on  $t_1$  and  $t_2$  only through the delay  $\tau$  and exhibits interference fringes as a function of  $(\omega_1 - \omega_2)$ , with fringe separation  $2\pi/\tau$  [66]. Furthermore, because the photons are in a single spatial mode, the unitary transformation describing our optical network adds an overall phase to the photonic wavefunctions and therefore, does not contribute to the interference.

In our experiment, we generate photon pairs using spontaneous parametric down conversion (SPDC) (Fig. 6.1). A periodically-poled potassium titanyl phos-

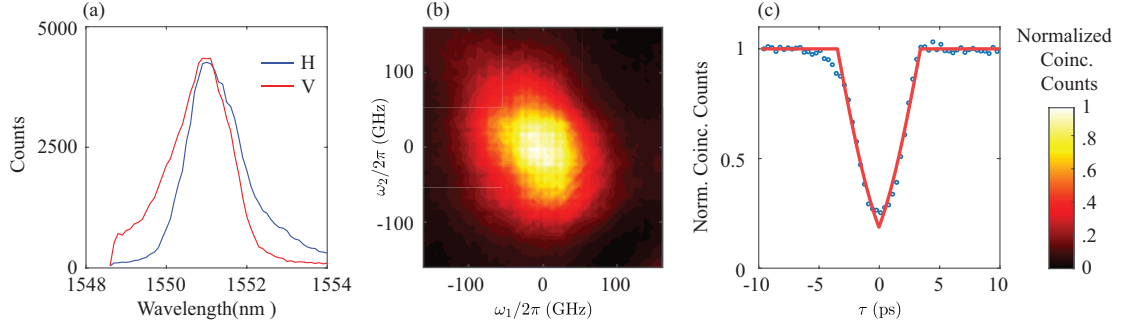


Fig. 6.2: (a) Measured spectra of H and V polarized photons, (b) joint spectrum intensity (JSI) and, (c) HOM interference dip with a visibility of 82%. The solid curve in (c) is an error function fit to the data [89].

phate (ppKTP) crystal (30 mm length) is pumped using a pulsed ( $\approx 1.6$  ps) 50 mW Ti-Sapphire laser  $\approx 775.5$  nm which generates orthogonally polarized, spectrally-degenerate photon pairs at telecom wavelengths via Type-II collinear SPDC. We separate the two orthogonally polarized photons using a polarization beam-splitter (PBS) and introduce a relative delay ( $\tau$ ) between them. We rotate the polarization in one of the arms such that the two photons are identically polarized and collect them into a single fiber using a beam-splitter. We then use a chirped fiber Bragg grating (CBG), two superconducting nanowire detectors (SNSPDs) and a time-interval analyzer (TIA) to measure the spectral correlations between photons.

This setup realizes a time-of-flight spectrometer where the arrival time of dispersed photons is used to infer their frequency spectrum [62, 82, 83, 90, 91]. Specifically, the frequency  $\omega_i$  of a photon detected at the detector  $i$  is related to the time-of-arrival  $t_i^d$  at the detector as  $(\omega_i - \omega_0) = (t_i^d - t_{0i}^d) / \phi''$ . Here,  $\omega_0$  is the peak frequency of the photonic spectral wavepacket and  $t_{0i}^d$  is the peak arrival time of the

photonic temporal wavepacket at the detector  $i$ .  $\phi'' \simeq 3196 \text{ ps}^2$  is the group delay dispersion (GDD) of the CBG. In our measurements, we set the central frequency  $\omega_0$  (corresponding to the time  $t_0^d$ ) to be zero such that  $\omega_i$  is actually the detuning from the central frequency. The spectral resolution ( $\delta\omega$ ) of our spectrometer is limited by the timing jitter ( $\approx 100 \text{ ps}$ ) of the nanowire detectors and is  $\approx 5 \text{ GHz}$ . Furthermore, the finite delay between the input photons contributes to the timing uncertainty in  $t_0^d$  and marginally lowers the spectral resolution of our spectrometer for input delay values approaching the inherent timing jitter of the detectors.

### 6.2.1 JSI and Pulse-width of generated photons

We use type-II SPDC in a 30-mm-long PPKTP crystal to generate two- and four-photons in our experiment. The crystal has a poling period of  $46.2 \text{ }\mu\text{m}$  and is held at a temperature of  $30^\circ \text{ C}$ . We pump the crystal using a pulsed Ti:sapphire laser ( $\approx 80 \text{ MHz}$ ,  $1.6 \text{ ps}$ ) set at a wavelength of  $\approx 775.5 \text{ nm}$  such that the spectra of generated photons ( $\approx 1551 \text{ nm}$ ) is well within the passband of our CBG ( $\approx 533 \text{ GHz}$ , centered at  $1550.9 \text{ nm}$ ). Figures 6.2(a-c) show the spectra of the horizontally (H) and vertically (V) polarized photons measured using a tunable filter and a superconducting nanowire detector, the joint spectral intensity of the two-photon wavefunction measured using CBG as a time-of-flight spectrometer, and the HOM interference dip. We observe small ellipticity in the JSI that also manifests in the two-photon spectral correlations. We also note that there is a small mismatch in the spectra of generated photons that reduces the visibility of the HOM interference. The visibility can be improved by spectral filtering or by using a crystal with ex-

tended phase matching [92]. Using HOM interference, we estimate the upper bound on the single-photon pulsewidth to be  $\approx 1.7$  ps (Fig. 6.2(b)). This agrees well the value of  $\approx 1.55$  ps that we estimate by fitting numerical simulation results to the experimentally measured data in the two-photon interference.

### 6.2.2 Two-photon Frequency-resolved Interference Results

Figures 6.3(a-d) show quantum interference fringes in the measured spectral correlations  $[\Gamma(\omega_1, \omega_2), 2\text{-fold coincidences}]$  for different delays between the two photons. The interference fringes can be seen more clearly by plotting the number of coincidences as a function of the frequency separation  $\omega_2 - \omega_1$  (Figs. 6.3(i-l)). As expected, the fringe separation decreases as  $1/\tau$  (Fig. 6.3(m)). Moreover, we see that the visibility of the interference decreases with increasing delay (Fig. 6.3(n)), disappearing completely for  $\tau \gtrsim 150$  ps (Fig. 6.3(d)). This is because of the residual distinguishability following spectrally resolved detection for time delays that approach the inverse of the spectral resolution  $\delta\omega$ . The interference visibility could, in principle, be restored by increasing the spectral resolution of the detector so that the condition  $\delta\omega \gg 1/\tau$  is satisfied [66, 80, 87]. Our experimental results agree well with the simulation results (Figs. 6.3(e-h)). We note that similar interference in spectral correlations has been observed in Refs. [82, 83] using the two spatial modes of a HOM interference setup. By contrast, in our setup, the two delayed photons are in a single spatial mode. Furthermore, the large GDD of our CBG allows us to observe interference between photons that are separated by delays as long as 100 ps, which is more than 50 times the single-photon temporal pulse-widths (estimated to



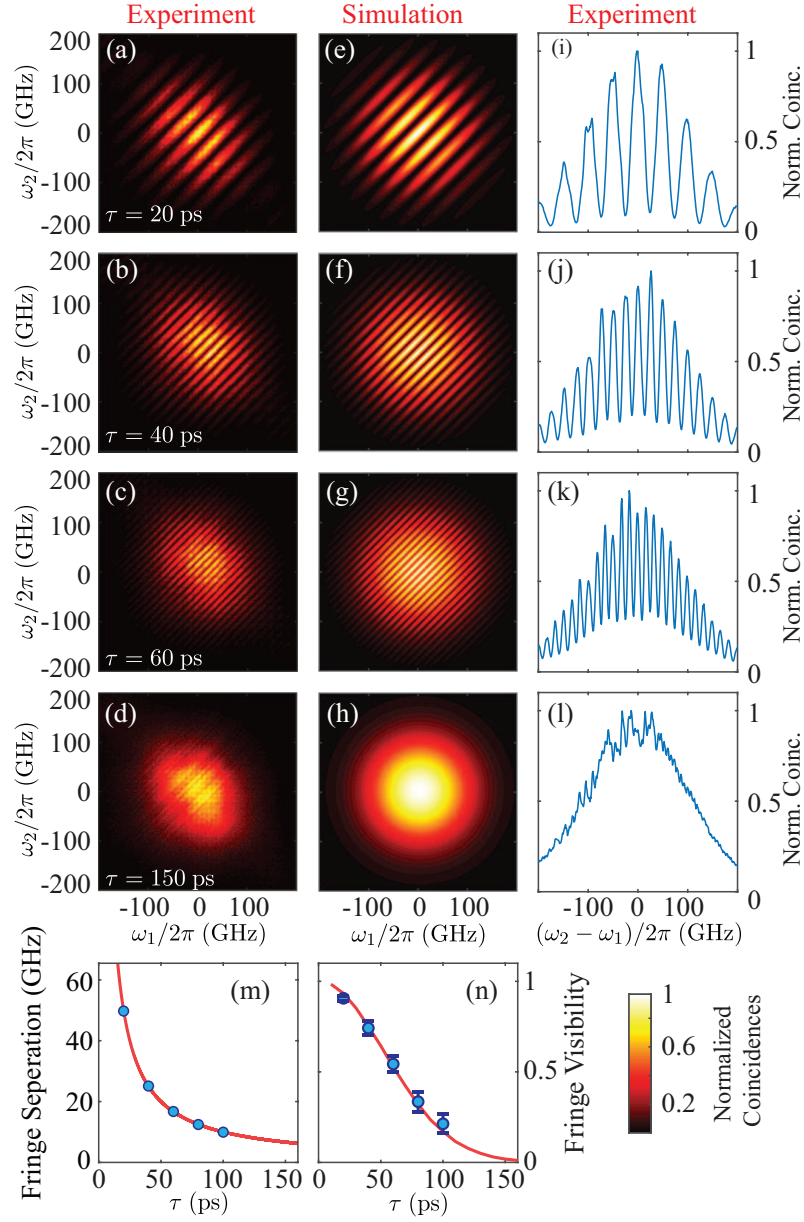


*Fig. 6.3:* (a-d) Measured and, (e-h) simulated spectral correlations  $[\Gamma(\omega_1, \omega_2, \tau)]$  between two photons with varying relative delay  $\tau$  at the input. (i-l) Measured coincidence counts (maximum normalized to unity) as a function of frequency separation  $(\omega_2 - \omega_1)$ . Measured (blue dots) and simulated (red line) (m) fringe separation, and (n) visibility as function of the delay  $\tau$ . The delay between the photons was calibrated using HOM interference.

be  $\approx 1.55$  ps). For each delay setting, the data was acquired for 12 minutes and the maximum number of coincidence counts (normalization factor) in Figs. 6.3(a-d) is 313, 277, 267, and 198, respectively, in a 1 GHz frequency bin.

### 6.2.3 Fringe Visibility

Figure 6.3 shows interference fringes in the normalized coincidence counts as a function of frequency detuning ( $\omega_2 - \omega_1$ ). From the plot, the interference fringe contrast seems to decrease with the increasing frequency detuning ( $\omega_2 - \omega_1$ ). This apparent decrease in the contrast is mainly because of the lower coincidence counts as we move away from the center of the two-photon spectral intensity distribution. Therefore, to better estimate the visibility of the interference, we use the ratio of coincidence counts to accidental counts (product of singles counts on the two detectors), shown in Fig. 6.4(a). We choose a window of 2 ns on each side from the center to further remove the contribution from the edges. Fig. 6.4(b) shows CAR as a function of ( $\omega_2 - \omega_1$ ). From this plot, we calculate the fringe visibility as  $(\overline{I_{\max}} - \overline{I_{\min}}) / (\overline{I_{\max}} + \overline{I_{\min}})$ , where  $\overline{I_{\max}}$  and  $\overline{I_{\min}}$  are averages of the peak maxima and minima, respectively. We used this visibility measurement scheme for all the data presented in Figures 6.3.

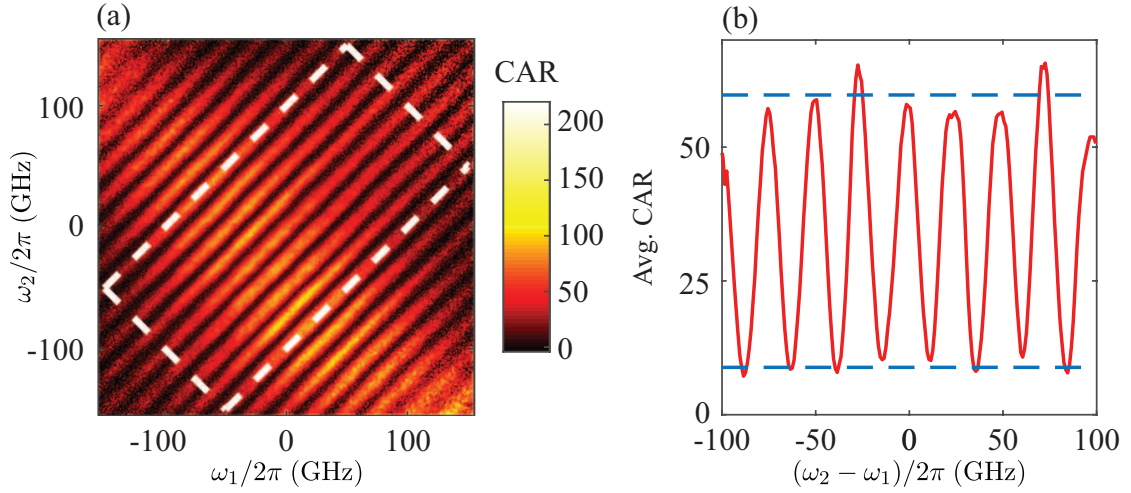


Fig. 6.4: (a) Measured CAR data for  $\tau = 40$  ps (b) Corresponding Fringe Separation data as a function of  $\omega_2 - \omega_1$ , blue dotted lines are the mean of the maximum peaks and the minimum peaks

### 6.3 Three-photon frequency-resolved detection

#### 6.3.1 Three-photon Frequency-resolved Interference Results

Next we discuss the experimental setup and our observation of three-photon interference using frequency-resolved detection. We pump the ppKTP crystal at higher power (400 mW) to ensure a higher probability of generating two pairs of photons. We use a PBS and two non-polarizing beam splitters to probabilistically split the four photons into four spatial modes (see Fig. 6.5(a)). We then introduce relative delays between the photons using two-photon interference measurements as a calibration tool, and combine three of the four spatial modes into a single fiber using a tritter ( $3 \times 3$  beam-splitter). As before, the three photons are then dispersed using the CBG, separated using a tritter and their spectral correlations are measured

using three detectors connected to the TIA. The fourth photon is used to trigger the TIA.

Figures 6.5(b-e) show the measured spectral correlations between the three photons (using four-fold joint detections) as a function of the frequency detunings measured at the second and the third detectors, relative to that of the first detector, that is,  $(\omega_2 - \omega_1)$  and  $(\omega_3 - \omega_1)$ . We analyze three different delay scenarios 1:  $(\tau_{21}, \tau_{31}) \approx (0, 15)$  ps, 2:  $(20, 40)$  ps and 3:  $(10, 25)$  ps, where  $(\tau_{21}, \tau_{31})$  are the delays of the second and the third photon, respectively, relative to the first photon. We observe that the interference landscape changes significantly with the relative delays between photons. For delays symmetric under exchange of two of the photons  $(\tau_{21}, \tau_{31}) \approx (0, 15)$  and  $(20, 40)$  ps, the interference fringes are periodic along both axes. By contrast, in the case of asymmetric delays  $(10, 25)$  ps, the constructive correlations are more prominent along the cross-sections  $\omega_2 = \omega_1$  (vertical),  $\omega_3 = \omega_1$  (horizontal) and  $\omega_2 = \omega_3$  (diagonal). However, irrespective of the delays between the photons, we always observe a constructive interference for zero frequency detuning, that is, when  $\omega_2 - \omega_1 = 0 = \omega_3 - \omega_1$  [see Eq.6.1]. We also analyze the scenario when the spectral resolution of our setup is not high enough to erase the temporal distinguishability of photons (Fig. 6.5(e)), and, as expected, we do not observe any interference.

We see that the interference patterns shown in Figs. 6.5(b-e) are symmetric under any permutation of the frequency detunings, for instance,  $\omega_2 \leftrightarrow \omega_3$  or  $\omega_3 \leftrightarrow \omega_1$ , etc. This permutation symmetry is simply a manifestation of the symmetry of our optical network [80]. We again emphasize that the interfering photons propagate

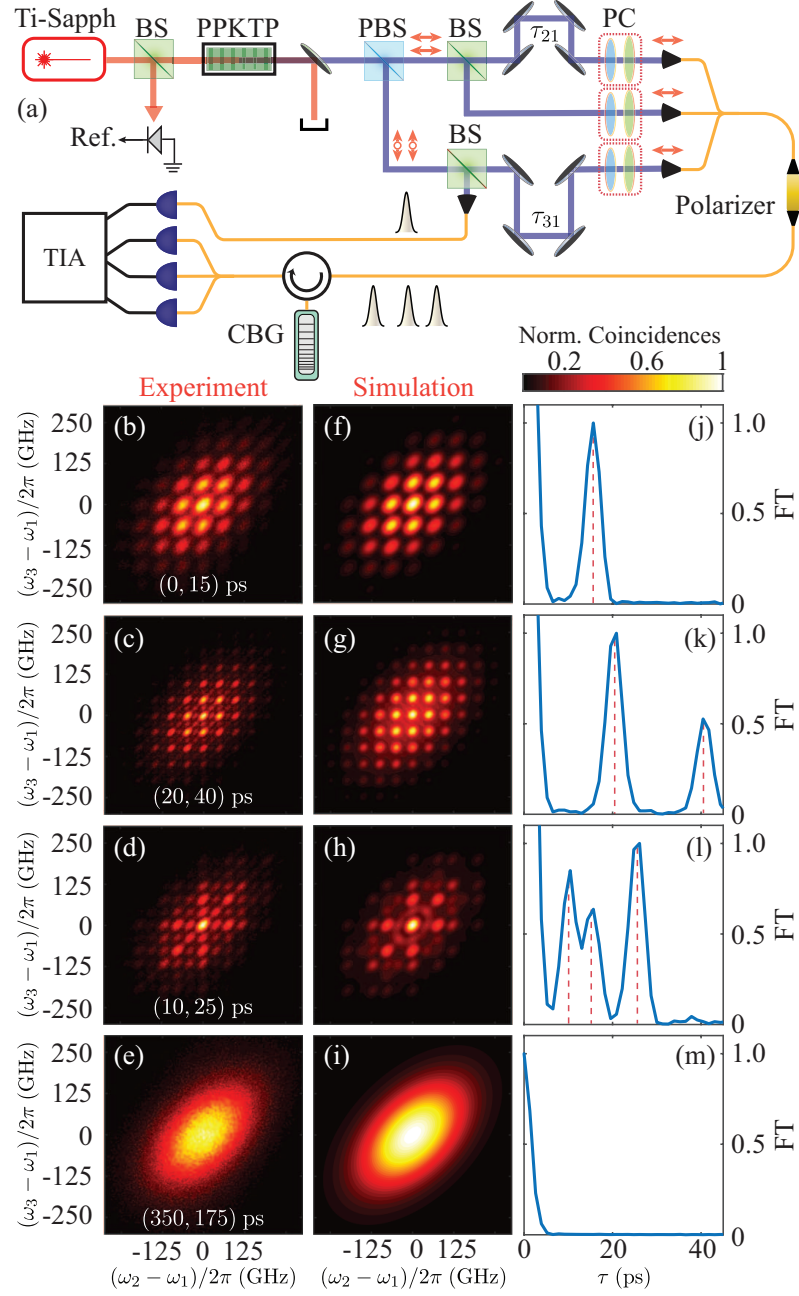


Fig. 6.5: (a) Schematic to observe frequency-resolved three-photon interference. (b-e) Measured and, (f-i) simulated spectral correlations between three photons with relative delays  $(\tau_{21}, \tau_{31}) \approx (0, 15); (20, 40); (10, 25); (350, 175)$  ps. (j-m) Fourier transform (FT) of the three-photon correlation function (in (b)-(e)), integrated over  $\omega_3$ . The peaks (highlighted by red dashes) indicate beat notes associated with multiple pairwise interferences.

in a single fiber. The tritter, together with the three detectors, at the output simply emulates a number-resolving detector and does not contribute to the interference. Moreover, the interference landscape is also symmetric under reflections  $\omega_i \leftrightarrow -\omega_i$ , for all  $i$ , where  $i = 1, 2, 3$  is the detector number, because of the symmetric frequency spectra of the input photons [80].

### 6.3.2 Reduced three-photon interference

Here, we show how the integration of the three photon interference over one of the frequencies, reveals information about multiple pairwise interferences. The three-photon correlation function,  $\Gamma(\omega_1, \omega_2, \omega_3) = \psi^*(\omega_1, \omega_2, \omega_3) \psi(\omega_1, \omega_2, \omega_3)$  where,  $\psi(\omega_1, \omega_2, \omega_3)$  is the three-photon spectral wave function at the detectors, and is associated with the different ways in which three photons with spectral amplitudes  $E_1, E_2, E_3$  at the input, injected at times  $t_1, t_2, t_3$  can trigger the three detectors at frequencies  $\omega_1, \omega_2, \omega_3$ . It is given as,

$$\begin{aligned}
\psi(\omega_1, \omega_2, \omega_3) = & E_1(\omega_1) E_2(\omega_2) E_3(\omega_3) e^{-i\omega_1 t_1} e^{-i\omega_2 t_2} e^{-i\omega_3 t_3} \\
& + E_1(\omega_2) E_2(\omega_1) E_3(\omega_3) e^{-i\omega_2 t_1} e^{-i\omega_1 t_2} e^{-i\omega_3 t_3} \\
& + E_1(\omega_1) E_2(\omega_3) E_3(\omega_2) e^{-i\omega_1 t_1} e^{-i\omega_3 t_2} e^{-i\omega_2 t_3} \\
& + E_1(\omega_2) E_2(\omega_3) E_3(\omega_1) e^{-i\omega_2 t_1} e^{-i\omega_3 t_2} e^{-i\omega_1 t_3} \\
& + E_1(\omega_3) E_2(\omega_1) E_3(\omega_2) e^{-i\omega_3 t_1} e^{-i\omega_1 t_2} e^{-i\omega_2 t_3} \\
& + E_1(\omega_3) E_2(\omega_2) E_3(\omega_1) e^{-i\omega_3 t_1} e^{-i\omega_2 t_2} e^{-i\omega_1 t_3} \quad (6.2)
\end{aligned}$$

We rewrite the above equation by separating the contribution of  $\omega_3$  as,

$$\psi(\omega_1, \omega_2, \omega_3) = \psi_{12} E_3(\omega_3) e^{-i\omega_3 t_3} + \psi_{13} E_2(\omega_3) e^{-i\omega_3 t_2} + \psi_{23} E_1(\omega_3) e^{-i\omega_3 t_1}. \quad (6.3)$$

Here

$$\psi_{ij} = E_i(\omega_1) e^{-i\omega_1 t_i} E_j(\omega_2) e^{-i\omega_2 t_j} + E_j(\omega_1) e^{-i\omega_1 t_j} E_i(\omega_2) e^{-i\omega_2 t_i} \quad (6.4)$$

such that  $\Gamma_{ij} = |\psi_{ij}^* \psi_{ij}|$  is the two-photon correlation function between photons with input times  $t_i$  and  $t_j$  respectively and is independent of  $\omega_3$ . When the three-photon correlation function is integrated over measured frequencies at one of the detectors, here  $\omega_3$ ,

$$\begin{aligned} \int_{-\infty}^{\infty} \Gamma(\omega_1, \omega_2, \omega_3) d\omega_3 &= \int_{-\infty}^{\infty} \psi^*(\omega_1, \omega_2, \omega_3) \psi(\omega_1, \omega_2, \omega_3) d\omega_3 \\ &= \int_{-\infty}^{\infty} \left[ |\psi_{12}|^2 |E_3(\omega_3)|^2 + |\psi_{13}|^2 |E_2(\omega_3)|^2 + |\psi_{23}|^2 |E_1(\omega_3)|^2 \right. \\ &\quad + \psi_{12}^* \psi_{13} E_3^*(\omega_3) E_2(\omega_3) e^{-i\omega_3(t_2-t_3)} \\ &\quad + \psi_{12}^* \psi_{23} E_3^*(\omega_3) E_1(\omega_3) e^{-i\omega_3(t_1-t_3)} \\ &\quad \left. + \psi_{13}^* \psi_{23} E_2^*(\omega_3) E_1(\omega_3) e^{-i\omega_3(t_1-t_2)} + \text{c.c.} \right] d\omega_3 \end{aligned} \quad (6.5)$$

The first three terms are pairwise interferences between photon pairs (1,2), (1,3), (2,3). The remaining terms integrate out to zero, given the single photon spectral wavefunctions are smooth functions of  $\omega$ . Therefore, the three-photon spectral correlation function integrated over one of the frequencies is given as

$$\int_{-\infty}^{\infty} \Gamma(\omega_1, \omega_2, \omega_3) d\omega_3 \propto |\psi_{12}|^2 |E_3(\omega_3)|^2 + |\psi_{13}|^2 |E_2(\omega_3)|^2 + |\psi_{23}|^2 |E_1(\omega_3)|^2, \quad (6.6)$$

where, the intensities of three single-photon spectral wavefunctions contribute to the weights of the pairwise interferences. Fig. 6.6 shows the measured three-photon correlation function integrated over  $\omega_3$  and plotted as a function of the frequency separation  $(\omega_2 - \omega_1)$ , for different delay settings.

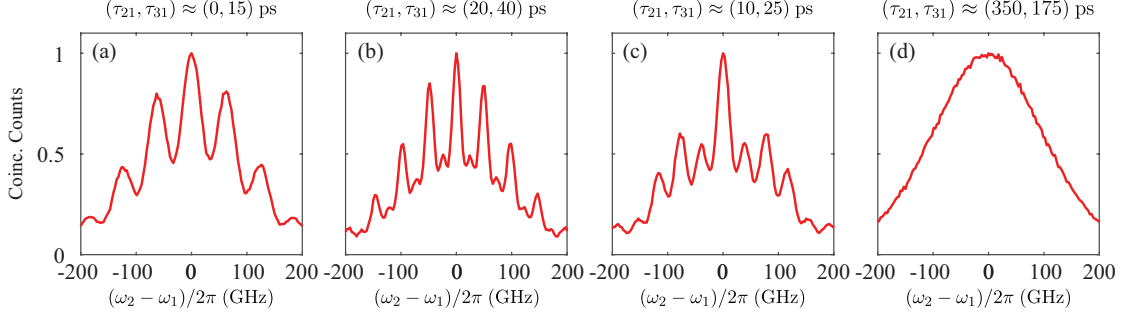


Fig. 6.6: Measured three-photon correlation function integrated over  $\omega_3$ , as a function of the frequency separation  $(\omega_2 - \omega_1)$  for different delay settings.

The measured three-photon interference is dictated by the  $3!$  three-photon detection amplitudes associated with the possible ways in which the three photons can trigger the three detectors. However, it is instructive to integrate the three-photon correlation function over one of the frequencies (here  $\omega_3$ ) and analyze the reduced interference as a function of the relative frequency detunings at the other two detectors  $(\omega_2 - \omega_1)$ . Fourier analysis of this 1D plot then reveals the beat notes corresponding to the multiple pairwise interference terms between the three photons (Figs. 6.5(j-m)). When the input delay values are configured to be  $(\tau_{21}, \tau_{31}) \approx (0, 15)$  ps, there is only one possible delay combination between any two photon pairs and the corresponding Fourier transform shows a single peak (highlighted by the dashed red line) at 15.7 ps. For (20, 40) ps, there are two possible combinations and accordingly we observe two peaks in the Fourier transform, at 20.9 ps and 40.4 ps. For (10, 25) ps, there are three possible combinations and as expected, we see three beat notes in the Fourier transform, at 10.4 ps, 15.7 ps and 26.1 ps. The peak delay values agree well with the expected values to within 1.3 ps, the temporal



resolution of the Fourier transform. For the three-photon interference experiment, we used a pump power of 400 mW and measured a four-photon generation rate of  $\approx 8000 \text{ s}^{-1}$ . The data in Figures 6.5(b-e) was acquired for 270, 270, 180, and 390 minutes, and the maximum number of four-fold coincidence counts (normalization factor) is 325, 286, 289, and 167, respectively, in a 3 GHz frequency bin.

### 6.3.3 *Miscellaneous probability contributions in three-photon interference*

Our three-photon interference setup uses one polarization beam splitter and two non-polarizing beam splitters to probabilistically split two pairs of orthogonally polarized photons into four spatial modes (Fig. 6.5(a)). We use one of the modes to trigger the TIA, and use the other three modes along with delay lines and a tritter to achieve a configuration of three photons at times  $(t_1, t_2, t_3)$  in one output port of the tritter (before the CBG). Due to the probabilistic nature of beam splitters, three photons with time-delays  $(t_1, t_1, t_3)$  and  $(t_2, t_2, t_3)$  are also generated with a probability of 0.25, in addition to the desired  $(t_1, t_2, t_3)$  events which occur with a probability of 0.5. In Fig. 6.7 we compare the simulated three-photon interference results, with and without these unwanted events. These events do not generate any new beat frequencies and therefore, do not drastically alter the three-photon interference pattern; we observe a fidelity of  $\approx 0.99$  between the two plots. These events could easily be removed using two ppKTP crystals to generate two photon pairs. Nevertheless, our experimental observations match very well with our simulations. We achieve a fidelity of  $\approx 0.95$  for each of the three scenarios presented in Fig. 6.5(b-d). The small loss in observed fidelities is because of the small ellipticity

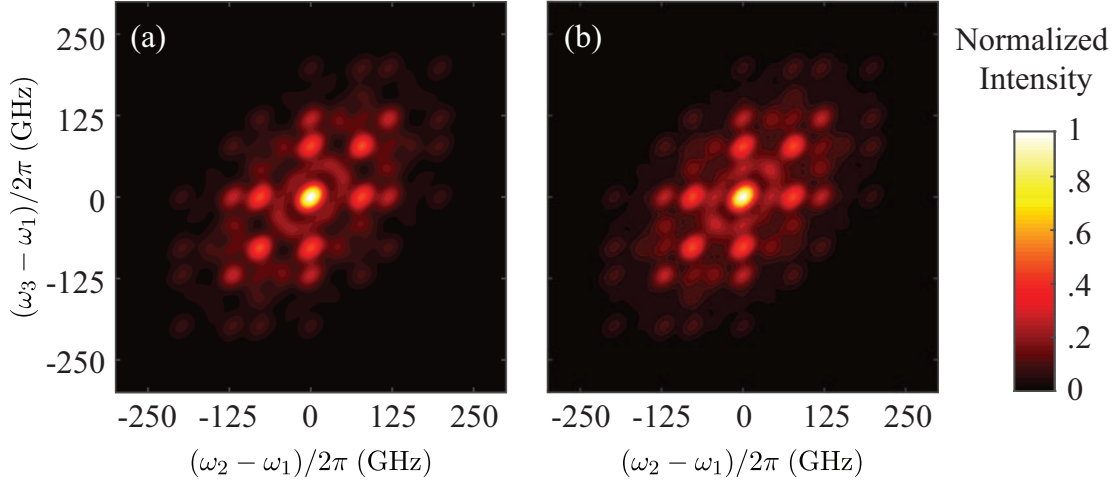


Fig. 6.7: Simulated three-photon interference, (a) without and, (b) with the extra probability terms, for delays  $(\tau_{21}, \tau_{31}) = (10, 25)$  ps.

in the joint spectral intensity of the photons.

#### 6.3.4 Photon generation rates

The measured two- and four-photon generation rates as a function of pump power are shown in Fig. 6.8. For the two-photon interference experiment, we used a pump power of 50 mW and the measured two-photon generation rate at the output of the SPDC was  $\approx 2.1 \times 10^5 \text{ s}^{-1}$ . The insertion loss of the CBG was measured to be 1.7 dB, and the per-channel excess insertion losses of the fiber beam splitter and the tritter were measured to be  $\approx 0.4$  dB and  $\approx 0.5$  dB, respectively.

### 6.4 Entangled two-photon Frequency resolved detection

Finally, we demonstrate frequency-resolved interference of two photons which are entangled in their arrival times. In particular, we consider time-bin entangled

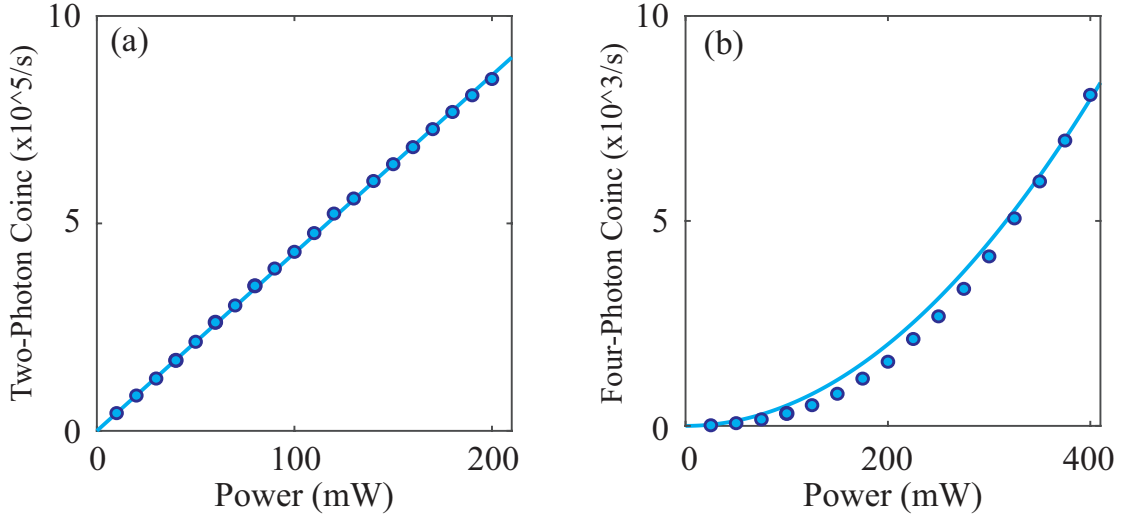


Fig. 6.8: (a) Measured two-photon and, (b) four-photon generation rates as a function of pump power. The solid lines are linear and quadratic fits to the data, respectively.

states of the form  $|\Psi\rangle = |2\rangle_e |0\rangle_l - e^{-i\varphi} |0\rangle_e |2\rangle_l$  where both the photons at the input are in the ‘early’ time-bin (at time  $t_1$ ) or in the ‘late’ time-bin (at  $t_2$ ) and  $\varphi$  is the phase associated with the delay between the photons. The spectral correlation function at the output of our optical network (Fig. 6.1) is then given as

$$\Gamma(\omega_1, \omega_2, \tau) = \left| \psi_1(\omega_1) \psi_2(\omega_2) e^{-i(\omega_1 + \omega_2)t_1} + \psi_1(\omega_2) \psi_2(\omega_1) e^{-i(\omega_1 + \omega_2)t_2} \right|^2. \quad (6.7)$$

The correlation function now exhibits interference fringes as a function of the two-photon phase  $\varphi = (\omega_1 + \omega_2)\tau$ , where  $\tau = t_2 - t_1$  is the relative delay between the photons. This interference is similar to the time-reversed HOM interference where the photons are path-entangled, that is, they arrive together at either port of the beam-splitter [41]. The two photons can then exit the beam-splitter in the same port or in different ports, depending on the phase  $\varphi$ .

#### 6.4.1 Generation of polarization and time-bin entangled photons

We use a HWP set to  $22.5^\circ$  before the PBS of the setup shown in Fig. 6.9(a) to generate polarization-entangled photon pairs in the two-photon interference setup. The HWP acts as a 50:50 beam-splitter in the polarization domain and when the two-photon spectral wavefunction is symmetric under exchange of photons, generates polarization-entangled state  $|\Psi\rangle = |2\rangle_H |0\rangle_V - |0\rangle_H |2\rangle_V$  [62, 93, 94]. To ensure the symmetric wavefunction, we use a band-pass filter with a bandwidth of  $\approx 0.6$  nm. To verify this entanglement, we measure the number coincidences in the two arms of the PBS as a function of the HWP angle [94] (Fig. 6.9). The coincidence counts follow a cosine function with a period of  $44(2)^\circ$ , half of that expected for single photons. We observe the coincidences to be minimum at  $22.5(5)^\circ$ , that is, when the two photons are polarization-entangled. The interference visibility is calculated to be 83.0(6)%. The low interference visibility is due to temporal walk-off between the H and V photons in the PPKTP crystal which leads to a small temporal distinguishability between the two photons at the HWP.

As shown in Chapter 5, we use a PBS to introduce a relative delay between the two orthogonal polarization modes and achieve the time-bin entangled state  $|\Psi\rangle = |2\rangle_e |0\rangle_l - e^{-i\varphi} |0\rangle_e |2\rangle_l$ . The phase  $\varphi$  was actively stabilised using a continuous-wave telecom laser with tunable wavelength. We verified the two-photon entanglement using coincidence measurements in the time domain (Fig. 6.9(c)). As before, we use a PBS to spatially separate the H and the V polarized photons. We then introduce a large delay ( $\approx 5$  ns) for the V-polarized photons such that they can be

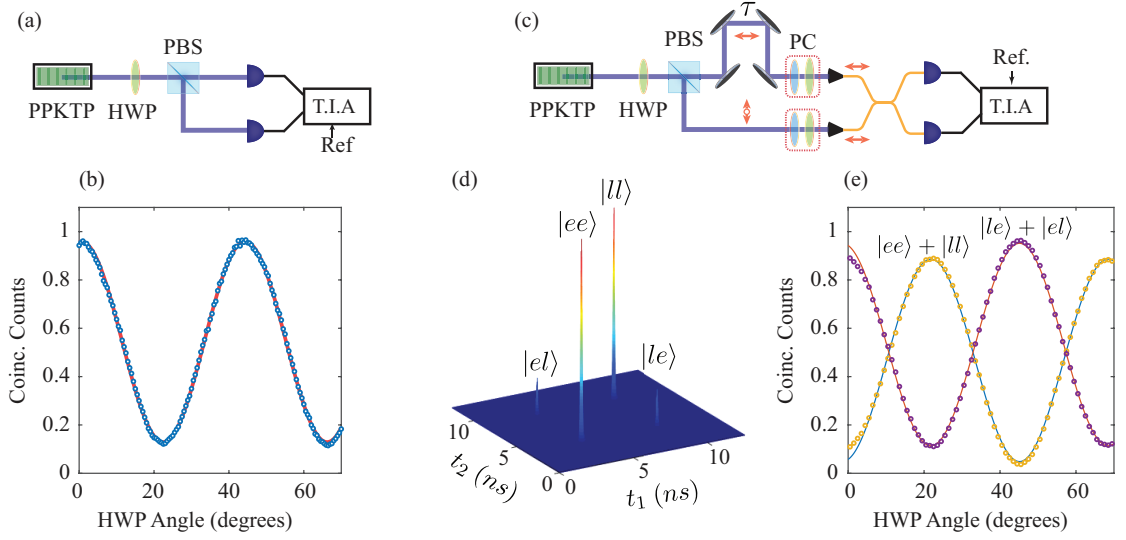


Fig. 6.9: (a) Experimental setup to verify polarization entanglement. (b) Measured coincidences (blue) as a function of the half-wave plate angle. Red solid line is a cosine fit to the data. (c) Experimental setup to verify time-bin entanglement. (d) Measured joint-temporal intensity at HWP angle of  $21.5^\circ$ , and (e) coincidences as a function of the half-wave plate angle.

temporally distinguished from the H-polarized photons. Subsequently, we change their polarization to H, and combine the two arms using a beam splitter. The H and the V polarization states now correspond to the ‘early’ and the ‘late’ time-bin states, respectively. Fig. 6.9(d) shows the measured temporal correlations between the two output ports of the beam splitter, when the HWP angle is set to  $22.5^\circ$ . As expected, we observe four coincidence peaks corresponding to the scenarios when both the photons arrive in the ‘early’ time bin ( $e - e$ ), or in the ‘late’ time bin ( $l - l$ ), and one photon arrives ‘early’ and the other ‘late’ ( $e - l$ , and  $l - e$ ). Fig. 6.9(e) shows the total coincidence counts in the  $e - e$  and  $l - l$  bins, and in the  $e - l$  and  $l - e$  bins, as a function of the HWP angle. Similar to the polarization resolved

measurements, we observe that the coincidence counts follow a cosine curve, and when the HWP angle is  $\approx 22.5^\circ$ , the two photons are in the time-bin entangled state  $|\Psi\rangle = |2\rangle_e |0\rangle_l - e^{-i\varphi} |0\rangle_e |2\rangle_l$ . The interference visibility for coincidence counts in the  $e - e$  and  $l - l$  time bins is  $\approx 90\%$  and that for the  $e - l$  and  $l - e$  time bins is  $\approx 79\%$ .

#### 6.4.2 Entangled photons Frequency-resolved Interference Results

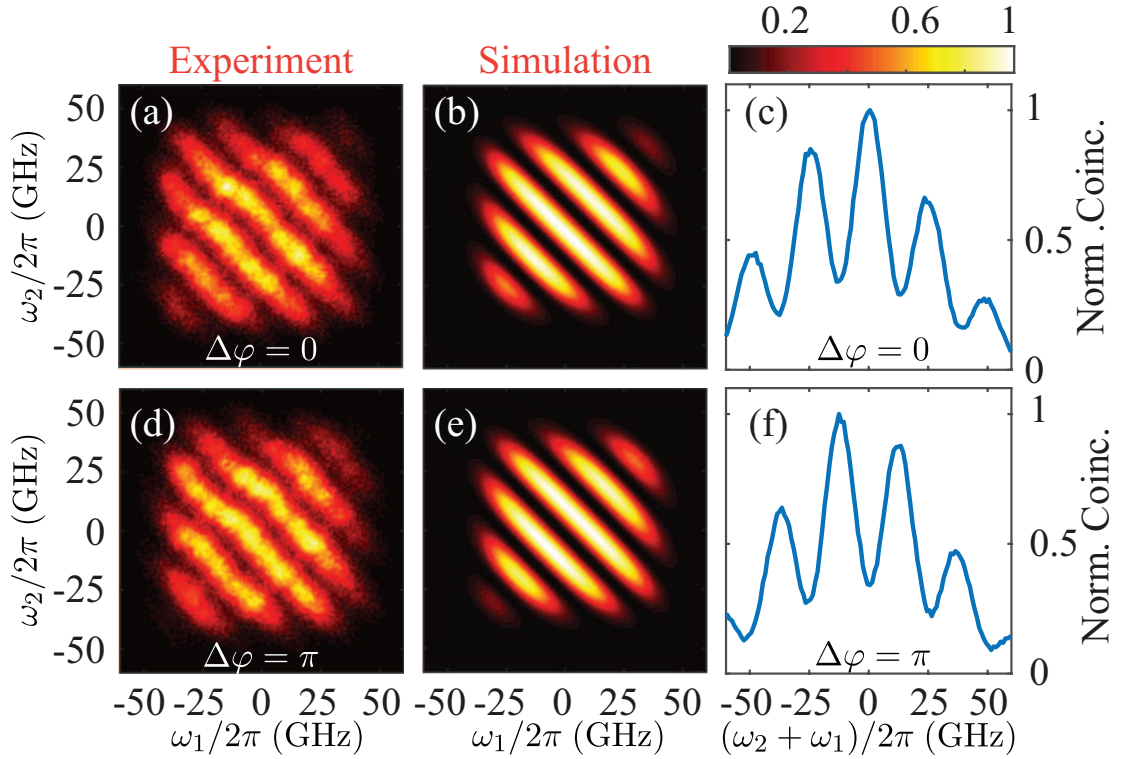


Fig. 6.10: (a-b, c-d) Measured and simulated spectral correlations for time-bin entangled photon pairs, with the phase factor  $\Delta\varphi = 0$  and  $\pi$ . (e-f) Measured coincidences as a function of  $(\omega_1 + \omega_2)$ .

Figures 6.10(a),(b) show the measured and simulated spectral correlations for the time-bin entangled two-photon state where we set  $t_2 - t_1 = 40$  ps, much longer

than the single photon pulsewidths (estimated to be  $\approx 5.4$  ps following the bandpass filter). We observe interference fringes in the correlations as a function of two-photon phase  $(\omega_1 + \omega_2) \tau$  (Fig. 6.10(c)). This contrasts the interference for a separable state of two-photons with a delay (Fig. 6.3) where interference pattern is rotated by  $90^\circ$  because of its dependence on  $(\omega_1 - \omega_2) \tau$ . Furthermore, as in the time-reversed HOM interference, the interference observed here is sensitive to small changes in the two-photon phase  $\varphi$ . For example, by introducing an additional small delay  $\Delta\tau$  (few fs) such that  $\Delta\varphi = (\omega_1 + \omega_2) \Delta\tau = \pi$ , we observe the complimentary interference where the peaks are replaced by troughs and vice-versa (Figs. 6.10(d-f)). We note that the decrease in the observed visibility for the interference of time-bin entangled photons compared to the unentangled photons (Fig. 6.3) is because of the sensitivity to path length fluctuations in the interferometer and also the imperfections in entangled state preparation. For this part, we pump the SPDC at 100 mW, and each data set was acquired for 20 minutes. The maximum number of counts in Figures 6.10(a,b) is 180, in a frequency bin of 1 GHz.

## 6.5 Summary

In this chapter, we have demonstrated frequency-resolved interference of three photons that are separated in time using a single dispersive element. Using a larger number of photons and a time-varying dispersion element, such as, a phase modulator, our setup could realize temporal boson sampling in a single spatial mode with easily reconfigurable unitary transformation and explore phase transitions in the

complexity of sampling [66,95]. Our scheme can also be used to implement scalable multi-boson correlation sampling where the photonic correlations are sampled over spatial as well as temporal/spectral modes at the input/output of a random linear optical network with multiple spatial modes [84,87]. Finally, these experimental results may pave the way to new techniques for the experimental characterization of optical networks and their input photonic states with potential application in quantum information processing and metrology [80,96,97].



## Chapter 7: Miscellaneous Experimental Techniques

### 7.1 *Signal Recovery and Amplifier for Time-lens*

#### 7.1.1 *Introduction*

In chapter 5, we implemented a time-lens technique to measure temporal and spectral correlations of time-bin entangled photons for resolutions smaller than the detector jitter. One of the key components of the setup was an Electro-Optic modulator (EOM) which acts as a spatial equivalent of a lens. We need to drive the EOM with an RF signal such that photons generated are centered around the quadratic region (Fig. 7.1(a)) of the phase. To accomplish that, we need to sync the RF drive to the laser. One could have used an external signal generator to generate the required RF signal, but most signal generators accept only a tolerance of  $\pm 50$  Hz in deviation from the input reference frequency. However, the photo-diode in our 780nm Ti-Sapphire laser could only produce a sync signal to an accuracy of .5 MHz and hence was not suited to work with external signal generators. For these reasons, we designed a custom signal-recovery printed circuit board (PCB) and an amplifier which could generate a signal synced to the laser and produce an RF sinusoidal wave of 2.8 GHz and  $V_m = 12$  V. Here, we discuss the design and operation of the PCBs.

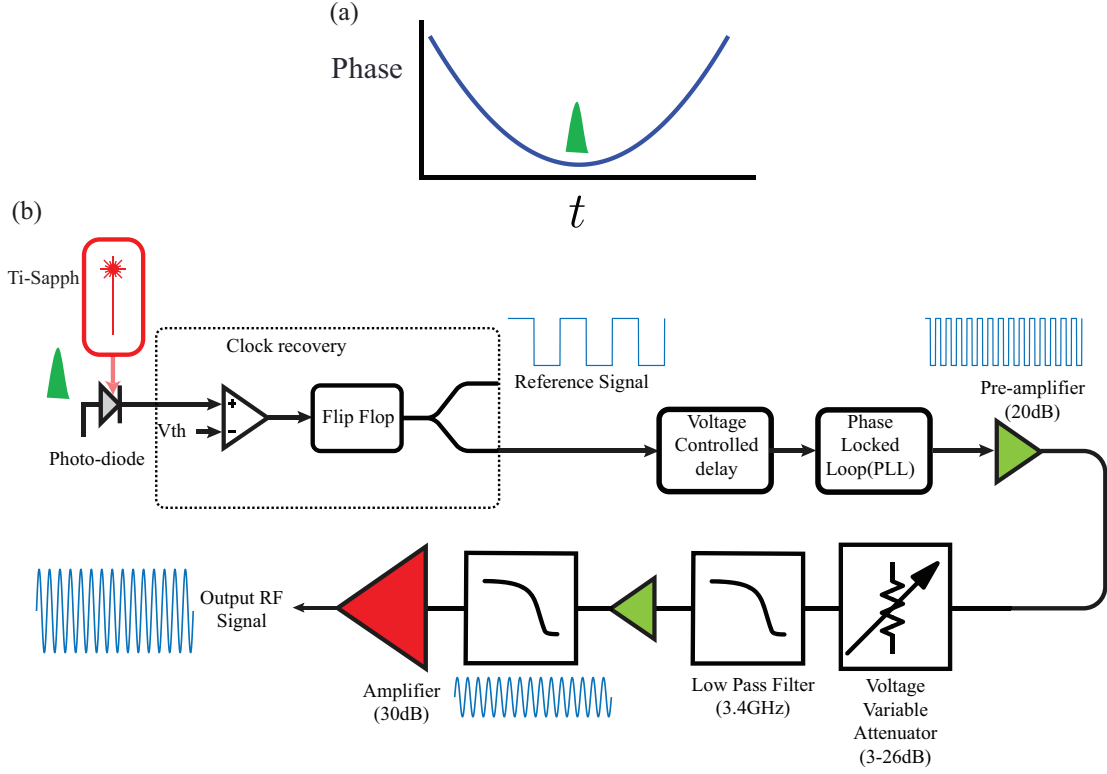


Fig. 7.1: (a) Input pulses should be synchronized such that the pulse is centered around the quadratic phase of the EOM. (b) Block diagram showing generation of an RF sinusoidal wave.

### 7.1.2 Setup

The successful operation of the temporal lens requires: (1.) synchronization between the electrical signal that drives the EOM and the Ti-Sapphire laser and (2.) minimization of the jitter between them. Preservation of low jitter has been guaranteed with the use of high-speed differential logic integrated circuits (IC) connected on printed circuit board (PCB) through microstrips and coplanar waveguides. Fig. 7.1(b) shows the block diagram for generation of RF signal. We use a fast photodetector (Thorlabs DET025A) after the Ti-Sapphire laser to get the pulse information

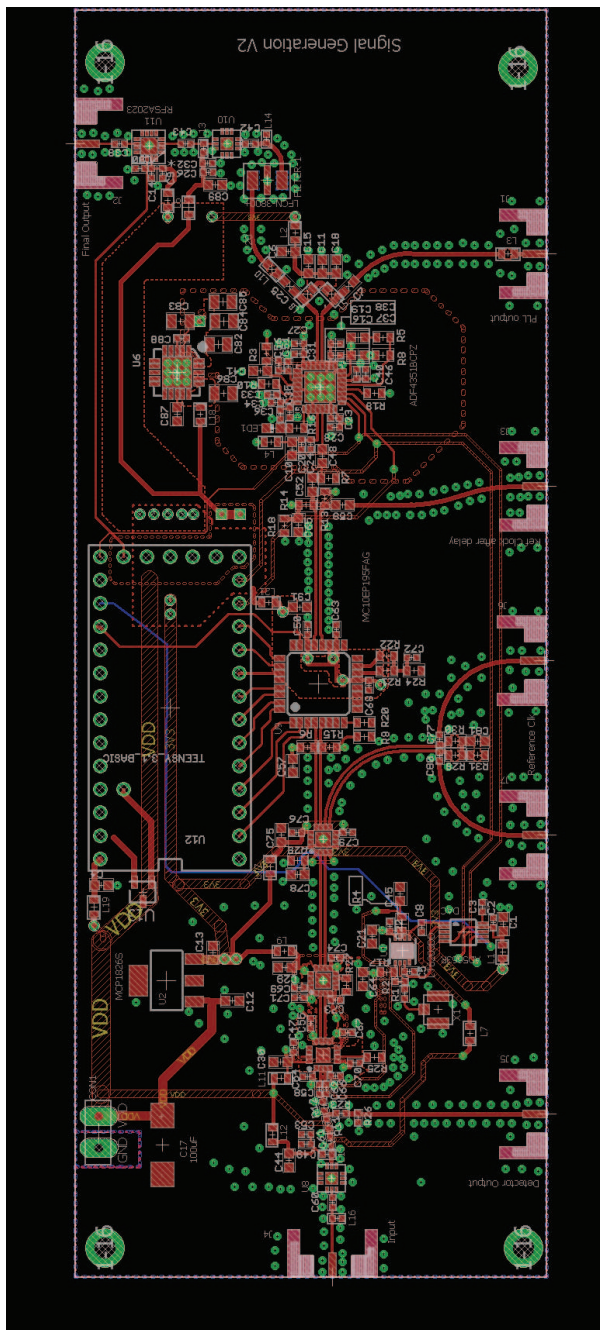
which is then processed by the clock recovery circuit to produce a synchronized clock with the laser. A part of the clock is sent to a time-interval analyzer to provide timing information of the incoming pulses. A voltage-controlled delay is used to control the timing of the pulses with respect to the RF wave. The clock is then fed to phase-locked loop (PLL) to produce a high frequency square wave synchronized with the clock. The signal is then amplified through a pre-amplifier and a voltage variable attenuator is used to control the amplitude of generated signal. The signal is amplified through a pre-amplifier and filtered through two low pass filters (Minicircuits VLF-3400+) to make it a sinusoidal wave by preserving only the fundamental frequency. An additional amplifier is used to achieve the desired operational RF power. Finally, the output RF signal is fed to the EOM.

We make two PCBs, one for signal recovery to generate the desired frequency and one for an amplifier to amplify the signal. The amplifier is made in a separate board as it needs additional cooling, less RF interference, and operates at higher voltage whereas all the components in signal recovery board operate at 5V.

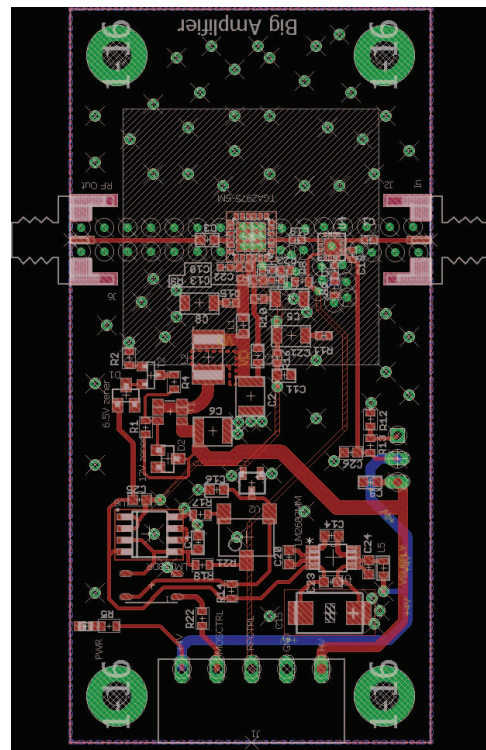
We use Eagle software to design the schematic and placement of components for both the PCBs. Our PCBs are four layer boards where routing is accomplished through copper traces. Depending on the complexity of the circuit, multiple layers of the board are used and different layers are connected through Via's. Most of the unused space on the board is grounded to prevent any floating voltages on individual components. All the copper traces for various signals are designed such that they are impedance-matched to  $50\Omega$ . The inputs and outputs are coupled SMA connectors.

Fig. 7.2 shows the board diagram for the signal recovery and the amplifier circuit.

## Signal Recovery Board



## Amplifier Board





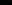
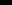
-  Via  
 Top Layer  
 Second Layer  
 Third Layer  
 Bottom Layer

Fig. 7.2: (a-b) Board diagram of signal recovery and amplifier. Each board consists of four layers.

### 7.1.3 Signal Recovery Board

The schematic of the signal generation circuit is shown in Fig. 7.3. The incoming signal from the fast photo-diode is amplified using low noise wide-bandwidth amplifier (Mini-circuits PMA3-83LN+). A fast comparator (Analog Devices AD-CMP572) with an adjustable threshold converts the signal into a clock using a flip flop (Onsemi NBSG53) in toggle mode. The output of the flip flop is a square wave with 50% duty cycle. A 1:2 differential fanout buffer (OnSemi NBSG11) is used to provide a clock reference that can be sent to the TIA. The other part of the clock goes through a digitally programmable delay (Onsemi MC10EP195) that provides a range of 1 ns with 10 ps increments. We use a commercial integrated PLL evaluation board (Analog Devices ADF4350) to generate an high frequency output wave  $\approx 2.8$  GHz which is programmable using a 3-wire interface. The produced RF signal is filtered through a low-pass filter (Mini-circuits LFCN-3800+) to remove higher harmonics and results in a sinusoidal wave. The sin wave generated is then amplified using a pre-amplifier (Mini-circuits PMA3-83LN+) and then passed through a voltage-controlled variable attenuator (RFMD RFSA2013). This allows fine tuning of the final peak-to-peak voltage applied to the EOM. The signal generated from the signal recovery board is then passed through an additional pre-amplifier (Minicircuits ZX60-83LN-S+) and a low pass filter (Minicircuits VLF-3400+) before being sent to the GaN power amplifier. The programmable elements like comparator thresholds, delay, and attenuation are controlled using a micro-controller (Teensy) with an USB interface. Fig. 7.4(c) shows the picture of the signal recovery PCB.

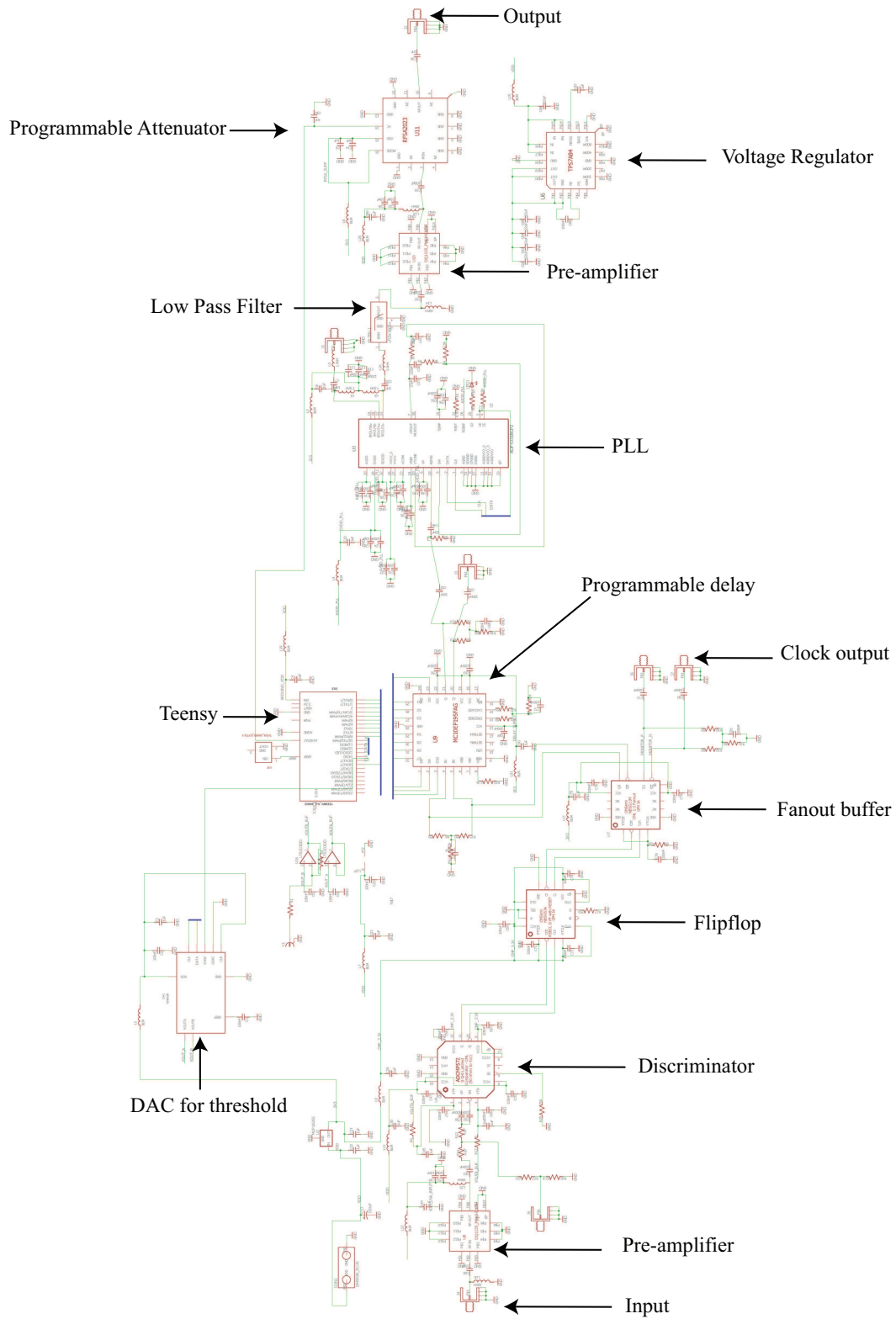


Fig. 7.3: Schematic of signal recovery PCB.

### 7.1.4 Amplifier

We use a high powered GaN monolithic amplifier (TGA2975-SM) to generate a gain of 30dB over a wide range of frequencies, 2.7 - 3.5GHz. The amplifier has a peak saturation of 35V which is well within our designed range of operation. The schematic of the circuit is shown in Fig. 7.4(a). An RF3025 absorptive switch is used to turn off or on the RF input power to the amplifier. The amplifier has a biasing up and down procedure that need to be correctly followed for successful operation of the amplifier. The bias up procedure used for the amplifier is:

1. Set ID limit to 1.3 A, IG limit to 8 mA
2. Apply  $-2.7$  V to VG
3. Apply  $+28$  V to VD; ensure IDQ is approx. 0 mA
4. Adjust VG until  $IDQ = 175$  mA ( $VG \approx -2.7$  V Typ.)
5. Turn on RF supply

and the bias-down procedure used for the amplifier is:

1. Turn off RF supply
2. Set VD to 0 V
3. Turn off VD supply
4. Turn off VG supply

We designed the circuit surrounding the amplifier to adhere to the biasing procedures and corresponding expanded schematic is shown in Fig. 7.5. The circuit works such that the gate voltage is switched on before the drain voltage to the amplifier. This is accomplished using a charge pump, some transistors and diodes. The voltage supply

to the amplifier is the voltage required for the drain voltage, 28 V. We use a voltage regulator to bring down the voltage from 28 V to +4 V which is then converted to -8 V using a charge pump. The output of the charge pump is connected to two circuits, one driving the drain voltage and the other driving the gate voltage. The connection to the gate is designed such that gate voltage is activated much before the charge pump reaches to -8 V. Hence, drain voltage activates after the gate voltage has been applied. Similarly, drain voltage is turned off before the gate voltage during discharge. This ensures the correct biasing operation of the amplifier.

In the gate voltage driving circuit, a voltage reference followed by a potentiometer is used to bring the voltage down to -2.7 V and a buffer is used to isolate any RF interference or ripple in the DC supply. The drain voltage driving circuit makes use of two transistors, an NPN bipolar junction transistor (BJT) and a P-type metal-oxide-semiconductor (P-MOS) such that the drain voltage is turned on when the charge pump is lower than -7.2V. An LC circuit is used to filter the RF noise or interference in the drain voltage.

We optimize the amplifier operation by controlling the gate voltage through a potentiometer and by looking at the current consumption of the amplifier as well the gain produced. Additionally, the amplifier has to be cooled to dissipate heat. We use two heat sinks, one on the top and the other on the bottom of the board and use fans to cool the amplifier (Fig. 7.4(b)). Using a 20GHz oscilloscope, we look at the amplified signal through a 30dB attenuator and compare with the clock generated. We observe that the waveforms have less than 50 ps jitter between them.



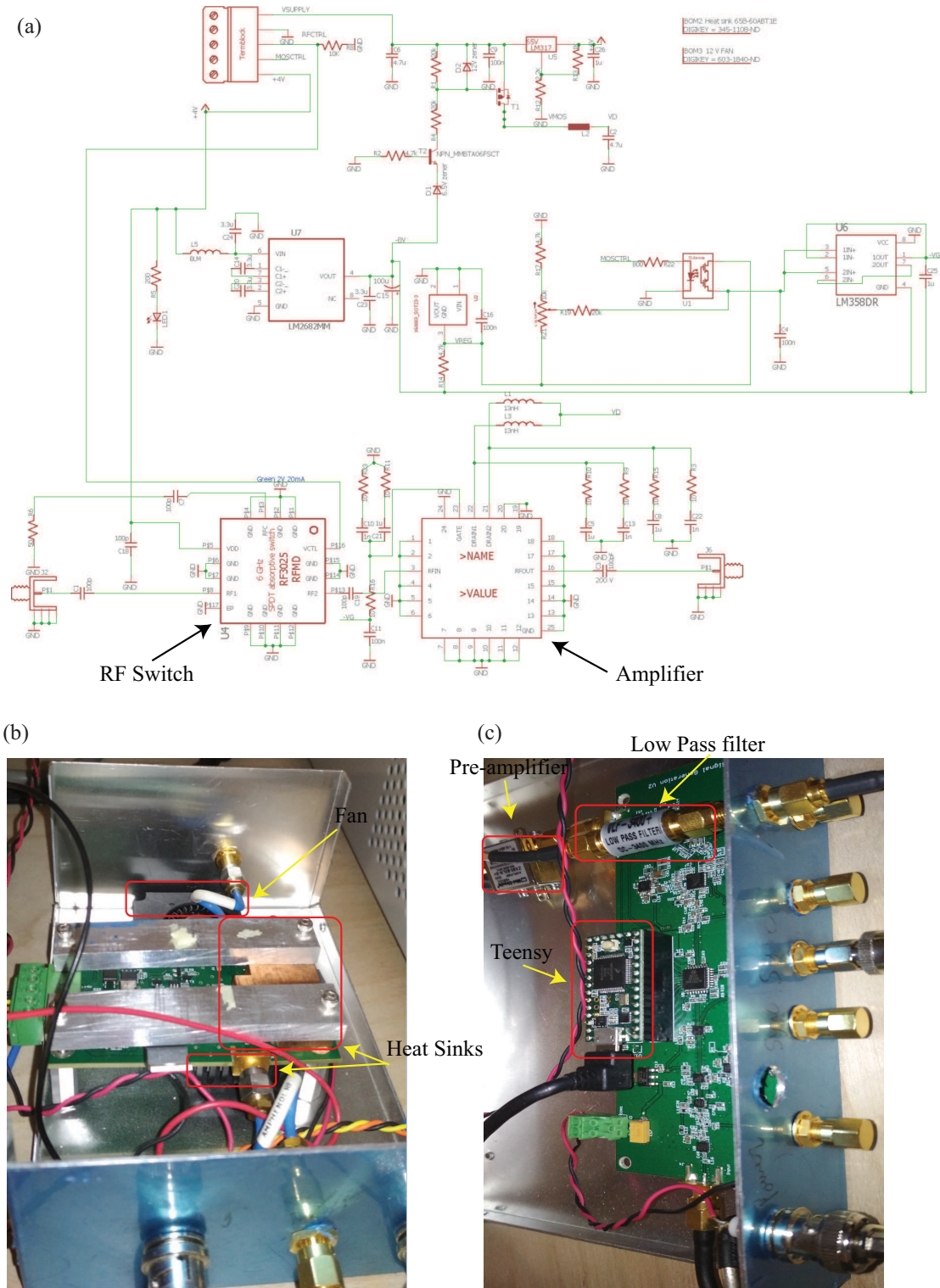


Fig. 7.4: (a) Schematic of Amplifier (b) PCB for amplifier (c) PCB for signal recovery.

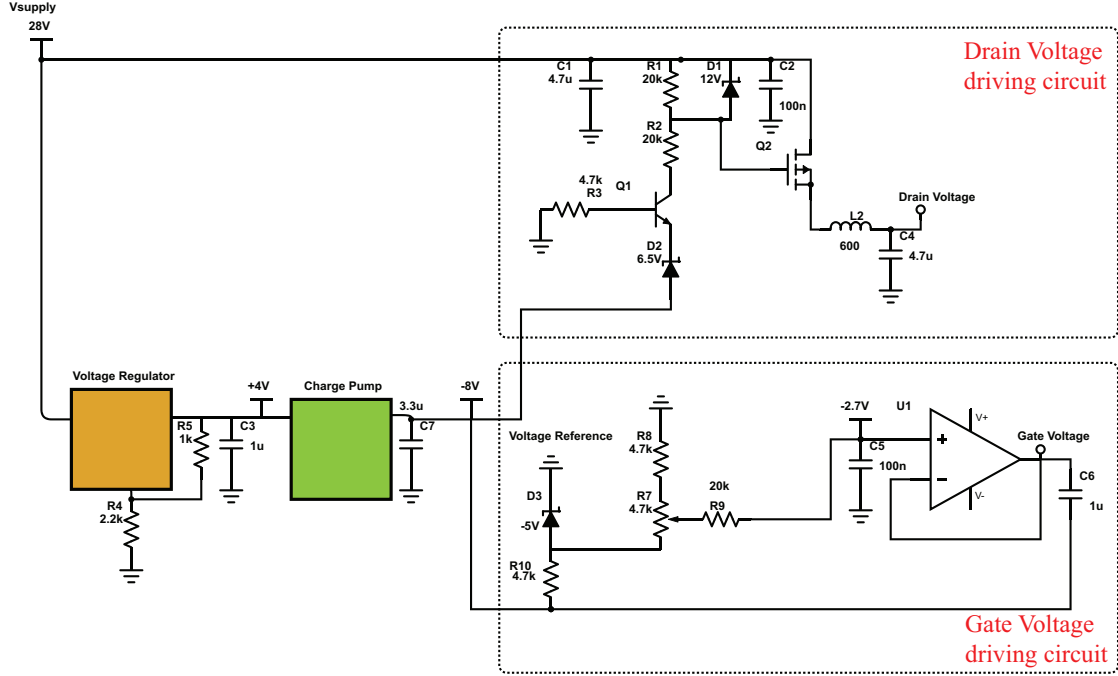


Fig. 7.5: (a) Schematic of driving circuits for Amplifier. Drain voltage turns on only after the gate voltage.

### 7.1.5 Labview Control

We control the frequency, delay, and amplitude of signal generated through a micro-controller Teensy and a labview interface. The arduino code to control teensy is given in Appendix C. We use Serial Peripheral Interface (SPI) communication protocol to communicate with Teensy. Fig. 7.6(b) shows the labview interface used to control the system. The amplitude and phase controls are in the other settings panel. Threshold 1 and threshold 2 control the discriminator settings for the clock generation. The PLL settings control the frequency of RF signal generated. The labview program runs in a continuous loop and we can choose to either update one parameter, such as amplitude, or all the parameters at once. The program is

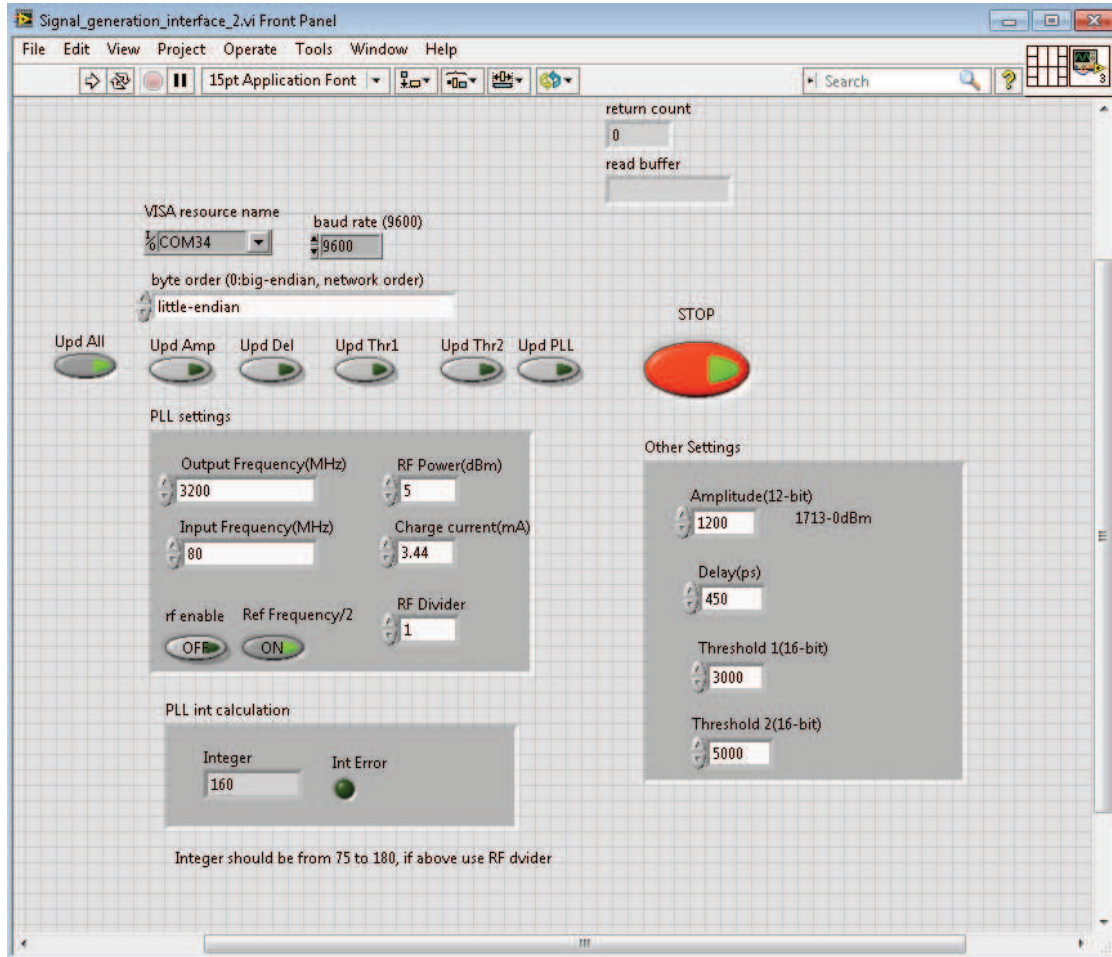


Fig. 7.6: Labview control for signal generation.

designed in such a way that it updates the registers in the Teensy, and the labview program can be closed without affecting the state of the system.

## 7.2 Spontaneous Parametric Down conversion Photon Pair

### Generation in a non-linear crystal

#### 7.2.1 Theory of Spontaneous Parametric Down conversion

Entangled-pair sources are frequently used in quantum information and quantum communication [30,31,55]. One of the most common ways to generate entangled photons is using spontaneous parametric down conversion (SPDC) [98]. We generate photon-pairs through type-II collinear SPDC process where a pump photon splits into signal and idler photons in a non-linear crystal. The energy conservation equation gives  $\omega_i + \omega_s = \omega_p$ , where  $\omega_{i,s,p}$  are the frequencies of idler, signal and pump photons respectively. The joint-spectral intensity of the output of SPDC is given by [99,100]

$$|\Psi(\omega_i, \omega_s)|^2 \propto e^{-\frac{(\omega_i + \omega_s - \omega_{p0})^2 \tau_p^2}{4 \log(2)}} \text{sinc} \left( \frac{\Delta k(\omega_i, \omega_s) L}{2} \right)^2 \quad (7.1)$$

where  $\omega_{s,i}$  are the frequencies of the signal and idler photons, L is the length of the crystal.  $\omega_{p0}$  is the central frequency of the pump and  $\tau_p$  is the width of the pump. The efficiency of the SPDC is maximum when the phase matching condition  $\Delta k(\omega_i, \omega_s) = k_i(\omega_i) + k_w(\omega_s) - k_p(\omega_i + \omega_s) + \frac{2\pi}{\Lambda}$  is satisfied. Here,  $k_j(\omega_j)$  is the frequency-dependant propagation constant and  $\Lambda$  is the poling period of the crystal.

From equation 7.1, the width of the generated two-photon spectrum depends on the temporal pulse-width of the pump beam and length of the crystal. By choosing different pulse-widths and crystal lengths, one could manipulate the joint spectral intensity (JSI) to create say, a separable state. For example, a choice of

1.6 ps pulse-width and 30 mm crystal in our system creates JSI which is close to a circle. Measured JSI is shown in Fig. 7.7(b) which matches well with the simulation in Fig. 7.7(a).

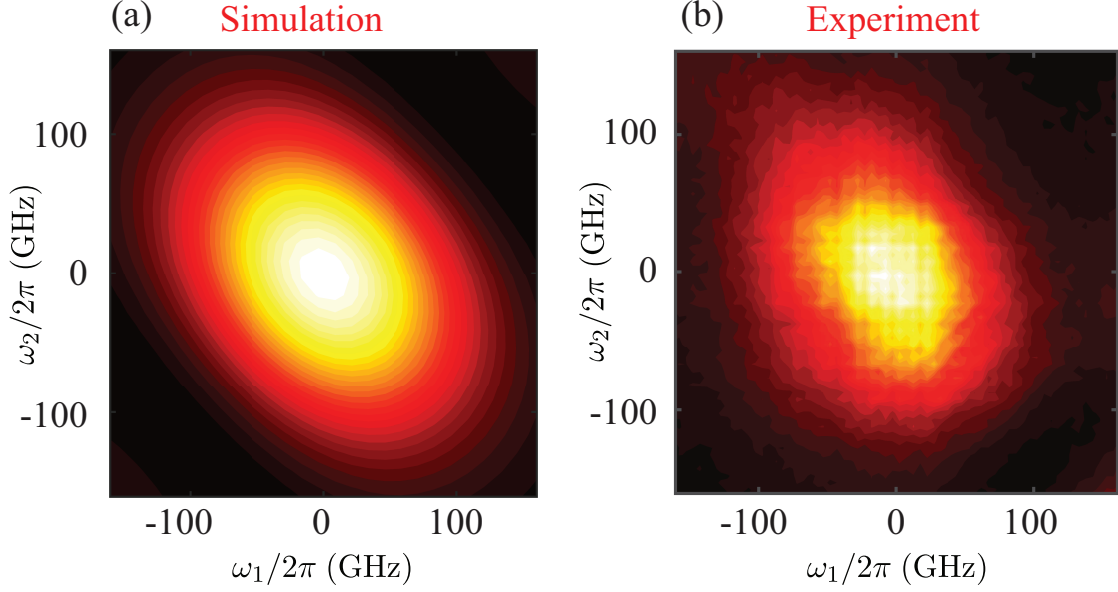


Fig. 7.7: (a-b) Simulated and measured Joint spectral distribution for parameters of pump width of 1.6 ps and 30 mm crystal length.

### 7.2.2 Design Parameters

In this section, we go through the experimental parameters in our SPDC setup. A pulsed Ti-sapphire laser around  $\approx 775$  nm is pumped through a PPKTP crystal to produce photon pairs at 1550.9 nm. The polling period of 30 mm crystal is  $46.2 \mu\text{m}$  and phase matched at  $30^\circ$  C. Fig. 7.8 shows the experimental setup for SPDC. One of the design parameters of the experiment is to determine the lenses needed to achieve the maximum efficiency. In order to determine the lens, we look at the optimal pump-width when focussed in the crystal. Ref. [101] has shown that

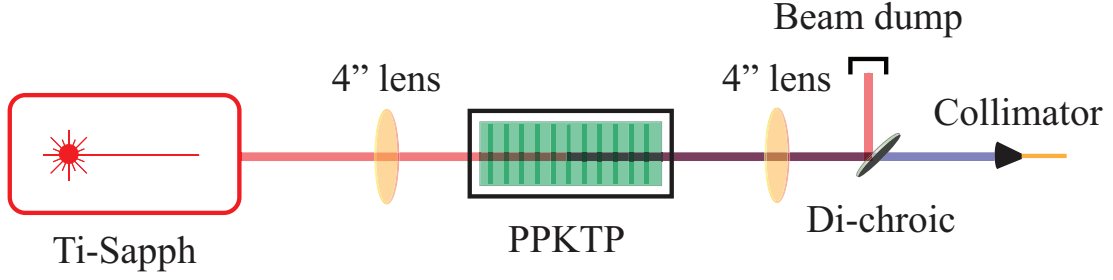


Fig. 7.8: Experimental setup for SPDC.

pump-width should be chosen such that the  $L/b = 2.84$ , where  $b$  is the confocal parameter to maximize the photon pair generation. This condition comes from trying to maximize the efficiency of the photon generation and number of photon-pairs generated which are inversely correlated [102]. The resultant beam-width,  $w_o$ , at the focus is derived from the rayleigh length,  $b = 2z_R = \frac{2\pi\omega_o^2}{\lambda}$ . Here,  $\lambda$  is wavelength of the light used. The corresponding focal length,  $f$ , of the lens is calculated from the equation  $2\omega_o = (\frac{4\lambda}{\pi})(f/D)$ , where  $D$  is the input beam diameter of the pump. For a crystal length of 30 mm, we determine that a focal length of  $4\tau$  (100 mm) is closest for maximizing the efficiency for 775 nm. Similarly, by optimizing the output diameter of the 1550 beam to the specifications of the collimator used for light collection and the focal length equation, we determine 100 mm lens gives the maximum output coupling after the SPDC. The efficiency of our SPDC setup is measured to be 25% by taking the ratio of coincidences to singles.

### 7.3 *Joint Spectral Intensity measurement using a chirped bragg grating*

Spectral correlations are commonly used to measure frequency statistics between photons, which is often helpful in characterizing a two-photon source. One method of characterization includes measuring Joint Spectral Intensity (JSI). Though it doesn't provide the phase information, it is still helpful in many scenarios like quantum walks [54,64] and boson sampling [32,65,66]. Traditionally, JSI is measured using a beam splitter and two scanning monochromators. The technique measures the JSI by looking at coincidences and performing a 2D scan of the monochromators. The number of photon counts at a given point are low (since the bandwidth is very small), which also requires a longer integration time. This leads to slower measurements requiring the source to be stable over long periods.

One promising technique to measure JSI is to use a time-of-flight spectrometer which maps the frequency information into time [90]. This works on the principle that in an optical medium, shorter wavelengths travel slower than long wavelengths for a positive dispersion. Hence, the corresponding frequencies can be mapped to time when they travel in a dispersive medium. We use chirped bragg grating (CBG) of group delay dispersion ( $GDD = -3190 \text{ ps}^2$ ) as the dispersive element. This technique enables a single shot measurement of JSI where all the photons contribute to the JSI and lead to faster acquisition times. Here, we show a typical setup for measuring JSI of photon pairs produced from SPDC using CBG (Fig.



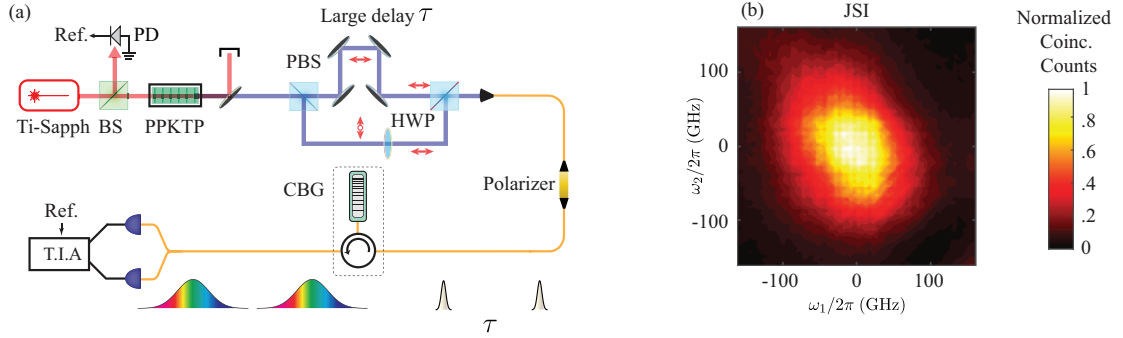


Fig. 7.9: (a) Experimental setup for measuring JSI (b) Measured JSI using CBG.

7.9(a)). The photons are separated by a polarizing beam-splitter (PBS) into two channels and the polarization is made identical for both the channels through a half-wave plate (HWP). A delay (5 ns) is introduced between the photons, which is longer than their temporal pulsewidths so that they don't interfere when sent through the CBG. The photons are then combined through a PBS and sent through the CBG. The coincidences are then collected from a time-interval analyzer (TIA) using a beam-splitter and two single photon nanowire superconducting detectors (SNSPDs).

The frequency  $\omega_i$  of a photon detected at the detector  $i$  is related to the time-of-arrival  $t_i^d$  at the detector as  $(\omega_i - \omega_0) = (t_i^d - t_{0i}^d) / \phi''$ . Here,  $\omega_0$  is the peak frequency of the photonic spectral wavepacket and  $t_{0i}^d$  is the peak arrival time of the photonic temporal wavepacket at the detector  $i$ .  $\phi''$  is the GDD of the CBG. In our measurements, we set the central frequency  $\omega_0$  (corresponding to the time  $t_0^d$ ) to be zero such that  $\omega_i$  is actually the detuning from the central frequency. The frequency resolution of the setup is determined by the dispersion of the CBG and the timing jitter of the detector and is calculated to be  $\approx 5$  GHz. We note that the



beam-splitter used to measure the coincidences has two possibilities, one early/late photons going to detectors 1/2 or the late/early photons going to detectors 1/2, which results in two symmetric images of JSI. Since resultant spectrum measured is symmetric, we look at one half of the spectrum to calculate the JSI. Fig. 7.9(b) shows a typical example of measured JSI using CBG.

#### 7.4 *Simultaneous measurement of Hong-Ou-Mandel dip for different frequencies*

We use identical photon pairs in many applications of quantum optics and quantum communications. One of the prominent tests to characterize indistinguishability of photons is Hong-Ou-Mandel (HOM) [47]. When two identical photons with a delay are interfered at a beam-splitter, the coincidences measured at the output of the beam-splitter exhibits a dip when the delay is zero and is the result of quantum interference. The visibility of the dip determines the indistinguishability of photons and is commonly used to characterize different photon sources. One of the experiments we wanted to implement was to use HOM to realize the robust quantum transport in edge states in our topological devices. We wanted to look at HOM interference by sending one path of the photons through the topological device and the other through a delay stage, and interfering them. In the process, we designed a technique to perform HOM interferences simultaneously for different frequencies. We realize this by using a CBG to map the frequency to time. Fig. 7.10(a) shows the experimental setup used to perform simultaneous HOM. The setup is similar to

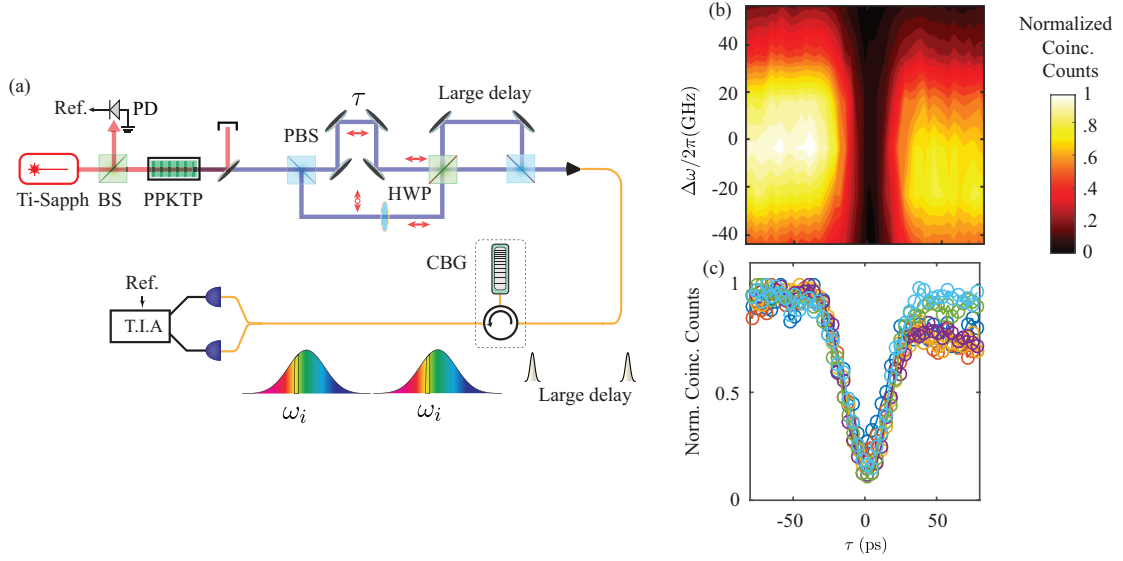


Fig. 7.10: (a) Experimental setup for measuring modified HOM (b) Contour plot of coincidence as a function of frequencies and delay (c) Normalized coincidences for different wavelengths.

JSI, where two photons are separated using a PBS and interfered with a delay  $\tau$  at a beam-splitter. The two channels are then delayed with a large delay greater than the temporal pulse-widths and then combined with a PBS. We use a PBS instead of a BS here, to maximize the number of coincidences. The output of a PBS is passed through a CBG and the timing of the coincidences are measured using a TIA after passing through a BS and two SNSPDs.

We find the coincidences for a given frequency by looking at the coincidences in corresponding frequency windows (mapped by the CBG) of photons in the spectrum. Fig. 7.10(b) shows a sample contour plot of coincidences with respect to frequencies and delay  $\tau$ . Fig. 7.10(c) shows the extracted HOM data for different frequencies. Using this technique we improve the acquisition time and simultaneously get HOM

data for all the frequencies in the input photon spectrum.

## Chapter 8: Conclusions and Outlook

Silicon photonics is a rapidly expanding platform to create integrated optical circuits for use in communications, sensing and quantum applications. However, fabrication disorder hinders their scalability by altering their functionality. Topological edge states are shown to be robust against fabrication-induced disorder. By using the robust nature of topological edge states, we can design devices which would perform superior to an array of ring resonators in the presence of disorder. In this work, we demonstrated a topological model (anomalous Hall) using ring resonators and studied two possible quantum applications of these topological models.

We began by demonstrating a photonic analogue of the anomalous Hall effect where the device exhibits edge states even when the net magnetic field is zero. We showed the presence of edge states by using transmission and imaging spectroscopy. Furthermore, we realized a topological trivial to non-trivial boundary interface in the device to show the tunability of the device by just changing the resonance frequencies of the site rings. Next, we used the edge states of an anomalous Hall device to generate indistinguishable photon pairs using spontaneous four-wave mixing. We demonstrated that the linear dispersion of the edge states lead to an efficiency phase matching condition resulting in maximum generation of photons in the edge band.

We also showed the tunability of the generated bi-photon spectrum in the edge band by changing the pump frequencies. We also confirmed the indistinguishability of photons by performing a Hong-Ou-Mandel experiment. Next, we studied the quantum transport in an integer quantum Hall device. Our simulations showed that edge states preserve two-photon correlations in the presence of disorder whereas the bulk does not. This illustrates that edge states of a topological devices can be used for quantum transport experiments.

In the process of realizing the quantum transport experiment, we devised two new techniques in quantum optics. We used an electro-optic modulator based time-lens technique to resolve photons which would not have otherwise been possible due to limited single-photon detector resolution. We measured the joint spectral correlations as well as the joint temporal correlations to show that the time-lens also maps from time to frequency. Next, we showed frequency-resolved interference of photons distinguishable in time in a setup that can be extended to perform boson sampling in time. We also showed that entangled photons behave similar to a time-reversed Hong-Ou-Mandel where the interference is sensitive to phase. Finally, we showed some miscellaneous experimental techniques such as design and construction of electronics for time-lens and a way to measure joint spectral distributions using a time-of-flight spectrometer.

We now describe two potential future experiments that could be based on this work.

## 8.1 Temporal Boson Sampling

In Chapter 7, we showed that photons distinguishable in time can be interfered by performing a frequency-resolved detection. As mentioned in the chapter, one can extend our setup to perform temporal boson sampling. Boson sampling is one of the benchmarks to achieve quantum supremacy [32, 73]. By measuring the probability statistics of photons travelling in an optical network, one can approximately compute the permanent of a matrix, a problem believed to be classically hard in complexity. Spatial mode boson sampling (SMBS) has been demonstrated experimentally where the interference happens between various spatial modes of system using beam-splitters [33]. By contrast, boson sampling in time (where the modes are time-bins) requires fewer resources compared to SMBS [66].

We can implement temporal boson sampling by changing the phase on the input photons. This can be accomplished by implementing a time-varying dispersion using phase modulators. By driving an electro-optic modulator (EOM) with a sinusoidal RF wave, one could operate in the linear region of the wave or the parabolic region. As the photons are separated in time, different pulses experience different phases and would realize permanents of different matrices. In addition, using an arbitrary function generator on the EOM would allow us to implement any random unitary matrix without the need for the phase control required in SMBS. Use of random unitary matrices would enable us to perform temporal boson sampling in time using the above setup.

## 8.2 *Two-photon experiment in Topological Devices*

In Chapter 5, we simulated the transport of time-bin entangled photons in a topologically non-trivial device. We tried different approaches such as sum-frequency generation, time-lens, simultaneous Hong-Ou-Mandel (HOM) for different wavelengths to realize this experiment. The main limiting factor in all these experiments is the loss in the device. The overall loss in our topological devices are  $\approx$  25-30 dB including the grating couplers. This results in an effective loss of 50-60 dB for coincidences when the photons go through the chip. In all the experiments we tried to realize, the acquisition time was in the order of tens of hours. However, the Ti-sapphire laser used to generate 1550 nm photons has a stability of about 10 hours and the single photon superconducting nano-wire detectors can only work for continuously 20 hours after which a cool down procedure should be re-initiated. Hence, all the above mentioned techniques have failed due to these limitations.

The experimental technique (frequency-resolved interference) we developed in Chapter 6 has a low loss and could be potentially used to realize the two-photon quantum transport experiment. A potential proposed experiment could be implemented as follows. Two photons with a delay of 40 ps with frequency bandwidth close to that of the lattice are sent into the lattice and the spectral correlations at the output are measured. Since the dispersion in edge states are linear, the fringes in the edge band width would have equal fringe spacing with period corresponding to 40 ps. In contrast, the bulk bands would exhibit varying dispersion from device to device and the fringe pattern in the bulk band would have an unpredictable pattern.

By observing this behavior across devices, one could show the robustness of the edge states against fabrication induced disorder in quantum transport experiments.



## Appendix A: Device parameters

In this appendix, we discuss the specifications of the fabricated anomalous Hall devices. Most of the specifications are similar to the integer quantum Hall devices fabricated in the same platform as given in [53]. The anomalous Hall devices are fabricated in silicon-on-insulator (SOI) platform using deep-UV projection lithography at a commercial foundry (IMEC, Belgium). The schematic of the silicon waveguide is shown in Fig. A.1(a). A silicon strip waveguide sits on a  $2\mu\text{m}$  layer of silicon oxide. The silicon dioxide layer is grown on top of a silicon substrate of  $\approx 500\mu\text{m}$ . The silicon waveguide is covered with a layer of silicon dioxide of about  $2\mu\text{m}$  on top to reduce the scattering losses from the waveguide. The width and height of the waveguide is 510nm and 220nm respectively. This structure supports propagation of only a single TE mode and we use polarization controllers in our experiments to match the supported polarization. The device is fabricated to support propagation of telecom wavelengths around 1550nm. The estimated effective refractive index  $n_{eff}$  and group refractive index  $n_g$  are 2.46 and 4.07 respectively at 1550nm.

We use focussing grating couplers to couple the light from the fiber in and out of the devices. The grating coupler focusses the  $10\mu\text{m}$  mode from the fiber into 500nm in the waveguide. The grating couplers have a loss of 6dB per coupler.

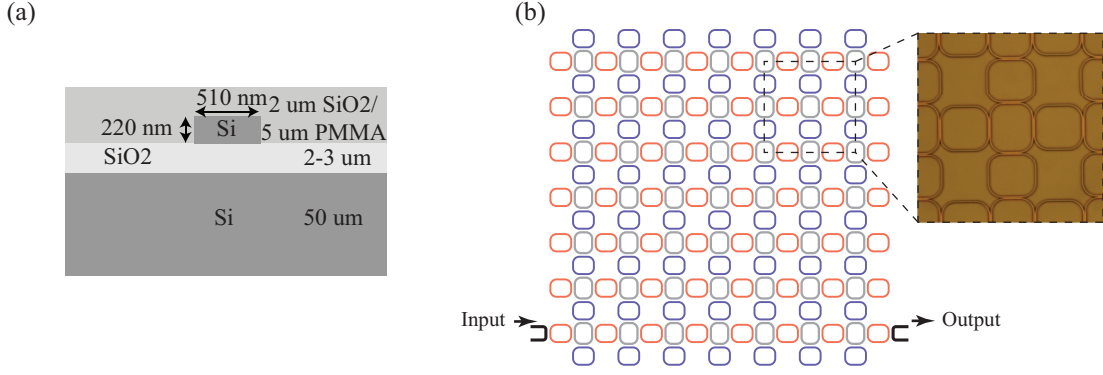


Fig. A.1: (a) Schematic of a silicon waveguide used in the structure. (b) Schematic of the anomalous Hall device which consists of a 2D array of race track resonators. Inset shows the microscopic image of the device.

The device consists of a two dimensional array of race track rings as shown in Fig. A.1(b). A race track resonator has been implemented as opposed to a ring, since the same amount of coupling would lead a smaller gap between the rings and would be a challenge to fabricate. The devices are  $70\mu\text{m}$  in diameter and length of the coupling regions is about  $7\mu\text{m}$ . The coupling gap between the rings is chosen to be  $180\text{nm}$  such that coupling between the rings,  $J$  is estimated to be  $15.6(4)\text{GHz}$ .

The free-spectral range is measured to be  $\approx 1\text{THz}$  ( $8\text{nm}$ ). This is much greater than the bandwidth of the device  $\approx 125\text{GHz}$  ( $1\text{nm}$ ) and hence the single mode approximation is valid. The estimated delay in each ring is about  $3.5\text{ps}$  whereas the round trip of each ring is around  $1\text{ps}$ . The average number of trips that the light makes in each ring is about  $3.5$ . The ring resonators have a low loaded quality factor  $Q$  of about  $1500$ . The loaded  $Q$  includes the loss to the input and output waveguides in the system. The low  $Q$  (larger bandwidth) design is used here because the edge states in the system will be well resolved. The loss in the system,  $\kappa_{in} = 2.9\text{GHz}$ . The

cross-coupling strength  $\kappa = .48$  and the absorption coefficient,  $\alpha = 15.8\text{m}^{-1}$ . The backscattering in these devices from surface roughness and couplers is suppressed and measured to be 25dB lower than the forward propagation.

## Appendix B: Simulation of delay and transmission spectra in an anomalous Hall device

Here, we discuss the procedure to simulate the propagation of electric field in an anomalous Hall device as also shown [53]. The Hamiltonian to the system is given by

$$\begin{aligned}
 H = & \sum_{\langle i,j \rangle} (\omega_0 - M) \hat{a}_i^\dagger \hat{a}_i + (\omega_0 + M) \hat{b}_i^\dagger \hat{b}_i \\
 & - J \left( \hat{a}_j^\dagger \hat{a}_i + \hat{b}_j^\dagger \hat{b}_i + \hat{a}_j^\dagger \hat{b}_i e^{-i\phi_{i,j}} + \text{h.c.} \right), \quad (\text{B.1})
 \end{aligned}$$

Here,  $\hat{a}_i$  and  $\hat{b}_i$  are the annihilation operators corresponding to site rings **A** and **B**, respectively, at lattice site index  $i = (x, y)$  and the summation  $\langle i, j \rangle$  is only over nearest and next-nearest neighbours.  $J$  is the coupling strength between nearest and the next-nearest neighbor sites, and  $\phi_{i,j} = \pm\pi/4$  is the direction-dependent hopping phase between sites **A** and **B**. By changing the sign of  $\phi_{i,j}$ , we can excite the other pseudo-spin in the system. The schematic of the system is shown in Fig. B.1.

For a finite system with site rings  $N$ , the Hamiltonian of the system can be written as an  $N \times N$  matrix. We represent the two dimensional system as an one dimensional array of rings arranged linearly. The diagonal terms in the Hamiltonian matrix are the energies of site rings which are also given by their resonance

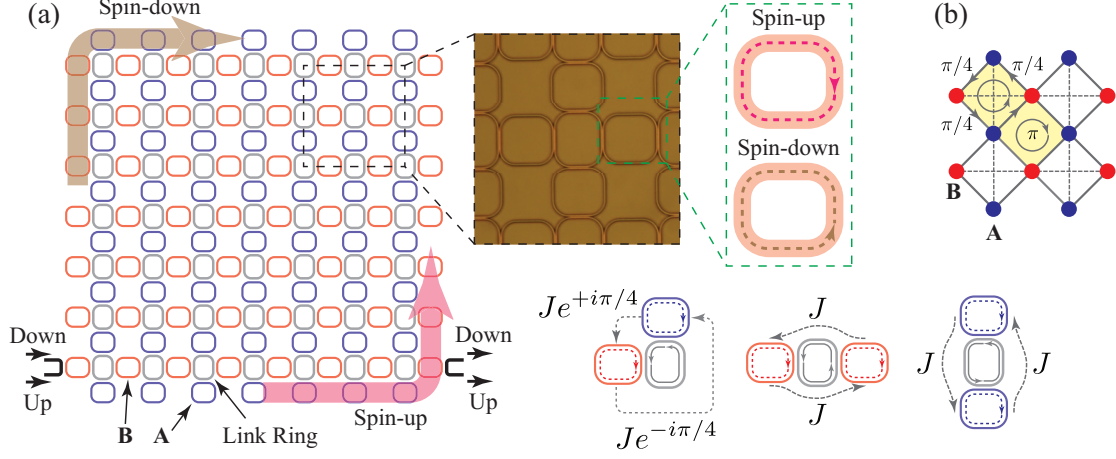


Fig. B.1: (a) Schematic of the 2D array of ring resonators, with site-rings **A**(blue) and **B**(red) coupled using link-rings (grey). Top-left inset: microscope image of the device. Top-right inset: the two pseudospin degree of freedom, up and down, which correspond to the clockwise and the counterclockwise circulation of photons in the site rings, respectively. Center inset: schematics for nearest-neighbor hopping (left) and next-nearest-neighbor hoppings (center and right) for the pseudospin-up. (b) Schematic of the 2D lattice. Red and blue circles indicate **A** and **B** lattice sites respectively. Solid lines denote nearest-neighbor hoppings between **A** and **B** sites, with hopping phases indicated. Dashes indicate next-nearest neighbor hoppings. The gauge flux is  $\pm\pi$  in a single plaquette, and zero over a unit cell of 2 plaquettes (shaded yellow).

frequencies,  $\omega_0 - M$  and  $\omega_0 + M$  for **A** and **B**. The off-diagonal elements in the matrix gives the coupling terms between the site rings. For example, the coupling term between nearest neighbours is given by  $-Je^{\pm i\pi/4}$  whereas, coupling between next nearest neighbours is given by  $-J$ .

The coupled rate equations are given by a set of differential equations [5, 9, 53]

$$\frac{d\hat{a}_i}{dt} = i[H_L, \hat{a}_i] - \kappa_{in}\hat{a}_i - (\delta_{i,I} + \delta_{i,O})\kappa_{ex}\hat{a}_i - \delta_{i,I}\sqrt{2\kappa_{ex}}\xi_I(t), \quad (\text{B.2})$$

$$\frac{d\hat{b}_i}{dt} = i[H_L, \hat{b}_i] - \kappa_{in}\hat{b}_i - (\delta_{i,I} + \delta_{i,O})\kappa_{ex}\hat{b}_i - \delta_{i,I}\sqrt{2\kappa_{ex}}\xi_I(t), \quad (\text{B.3})$$

The first term on the right gives the coupling between the rings and self-coupling i.e. the resonance frequencies of the rings. The second term gives the loss rate  $\kappa_{in}$  in the rings from scattering and attenuation. The third term is the loss of energy from coupling to input ( $I$ ) and output ( $O$ ) waveguides, where  $\kappa_{ex}$  is the loss rate associated with the coupling. The last term is the input energy to the lattice, where input electric field  $\xi_I(t)$  is coupled to the lattice using a waveguide coupler. Here, the electric field is normalized to power. If the input electric field is a continuous wave of the form  $\xi_I e^{-i\omega t}$ , we can use the rotating frame approximation and simplify the equations to

$$-i\omega a_i = i[H_L, a_i] - \kappa_{in}a_i - (\delta_{i,I} + \delta_{i,O})\kappa_{ex}a_i - \delta_{i,I}\sqrt{2\kappa_{ex}}\xi_I, \quad (\text{B.4})$$

$$-i\omega b_i = i[H_L, b_i] - \kappa_{in}b_i - (\delta_{i,I} + \delta_{i,O})\kappa_{ex}b_i - \delta_{i,I}\sqrt{2\kappa_{ex}}\xi_I, \quad (\text{B.5})$$

$a_i$  and  $b_i$  are the expectation operators of the operators  $\hat{a}_i$  and  $\hat{b}_i$  respectively. The conversion of  $\hat{a}/\hat{b}_i$  to  $a_i/b_i$  is justified because the Hamiltonian is linear. These set

of coupled linear equations can be solved using matrix methods as there no longer have time dependence in them.

The output drop port field of the lattice is given by  $\xi_D = \sqrt{2\kappa_{ex}} a_O / b_O$  using the input-output formalism. The transmission spectra is simulated by taking values of  $|\xi_D|^2$  for the different frequencies whereas, the wigner delay is calculated by taking the derivative of the phase  $\tau_D = \frac{d}{d\omega} \left( \frac{\xi_D}{|\xi_D|} \right)$ .

## Appendix C: Arduino code for Teensy operation

```
1 #include "SPI.h"
2
3 //Control 4 bits to select the data to send
4 //0x0- Amplitude
5 //0x1- Delay
6 //0x2- Threshold 1
7 //0x3- Threshold 2
8 //0x4- PLL setting
9
10 // 0 is false and 1 is true
11 class Data {
12 public:
13     unsigned int Amplitude, Delay, Threshold_1, Threshold_2
14     ;
15     unsigned int Amplitude_prev = 1, Delay_prev = 1,
16     Threshold_1_prev = 1, Threshold_2_prev = 1;
17
18     bool rfenable, fastlockenable, refby2, prescaler, mtld,
19     feedback ; //PLL
20     unsigned int Frequency, rfPower, ChargepumpCurr,
21     ClkDivValue, integer, rcounter, dividervalue,
22     RFdivider ; //PLL
23
24     //Data stream for PLL in order
25     //1.4 bit rfenable
26     //2.4 bit refby2
27     //3.8 bit Frequency
28     //4.8 bit rfPower
29     //5.8 bit ChargepumpCurr
30     //6.8 bit integer
31     //Total 10 bytes
32
33     byte reg[6][4]; //Registers to write for PLL
34     byte comm[3][3]; //commands to send to DAC
35 }
```



```

30     Data() { // Initialize some setting which can be
           changed later if needed
31         ClkDivValue = 150;
32         fastlockenable = 1;
33         mtld = 0;
34         //Initialize some with safe values
35         prescaler = 0;
36         Frequency = 3000;
37         rfPower = 3;
38         ChargepumpCurr = 9;
39         integer = 120;
40         Amplitude = 3500;
41         Delay = 10;
42         Threshold_1 = 2500;
43         Threshold_2 = 2000;
44         rfenable = 0;
45         refby2 = 1;
46         rcounter = 1; // by default 1 for lower input
           frequencies
47         feedback = 1; // 0-divided 1-fundamental
48         RFdivider = 0; // 0=1, 1=2, 3=4, ..6=64
49         dividervalue = (Frequency*(pow(2, RFdivider)))/(
           integer*.125);
50     }
51
52 };
53
54 Data *data;
55 int PLL_LEpin = 10; //Chipselect of PLL
56 int DAC_LEpin = 15; //Chipselect of DAC's
57 int D0 = 16 , D1 = 9, D2 = 8, D3 = 7, D4 = 6, D5 = 5; //
           Delay chip pins
58 int D6 = 4, D7 = 3, D8 = 2, D9 = 1, D10 = 0;
59
60 void updatePLL() {
61     unsigned long   int_r0=0, int_r1=0, int_r2=0, int_r3=0,
           int_r4=0, int_r5=0; // temp int for registers
62
63     if (data->Frequency > 3600) {
64         data->prescaler = 1;
65     }
66     else data->prescaler = 0;
67
68     data->dividervalue = (data->Frequency*(pow(2, data->
           RFdivider)))/(data->integer*.125);

```

```

69
70 //prepapare the registers
71
72 int_r0 = (data->integer << 15); // sets int value
73 byte r0Ary[] = { lowByte(int_r0 >> 24), lowByte(int_r0 >>
16), lowByte(int_r0 >> 8), lowByte(int_r0) };
74 memcpy(&data->reg[0], &r0Ary, sizeof(r0Ary));
75
76 int_r1 = (data->prescaler << 27) +// Prescaler 0-4/5
and 1-8/9
77 (1 << 15) + // phase value = 1
78 (2 << 3) + // modulus value = 2
79 1; // register value
80 byte r1Ary[] = { lowByte(int_r1 >> 24), lowByte(int_r1 >>
16), lowByte(int_r1 >> 8), lowByte(int_r1) };
81 memcpy(&data->reg[1], &r1Ary, sizeof(r1Ary));
82
83 int_r2 = (0 << 26) + // muxout
84 (data->refby2 << 24) +// Divide-by-2
85 (data->rcounter << 14) + // r-counter = 1
86 (data->ChargepumpCurr << 9) + // charge pump
- 0-15
87 (10 << 5) + // digital lock detect + polarity
+ powerdown
88 2; // register value
89
90 byte r2Ary[] = { lowByte(int_r2 >> 24), lowByte(int_r2
>> 16), lowByte(int_r2 >> 8), lowByte(int_r2) };
91 memcpy(&data->reg[2], &r2Ary, sizeof(r2Ary));
92
93 int_r3 = (data->ClkDivValue << 3) + //Clock divider
value
94 (data->fastlockenable << 15) +// Enable fast
lock
95 3; // (all zero, except register control value =
3);
96 byte r3Ary[] = { lowByte(int_r3 >> 24), lowByte(int_r3 >>
16), lowByte(int_r3 >> 8), lowByte(int_r3) };
97 memcpy(&data->reg[3], &r3Ary, sizeof(r3Ary));
98
99 int_r4 = (data->feedback << 23) + // divided/fundamental
feedback
100 (data->RFdivider << 20) +//RF divider select
101 (data->dividervalue << 12) + // band select
clock divider

```

```

102         (data->mtld << 10) + // Mute till lock
103         (0 << 9) + // vco powerdown = false; MTLD = 1;
           aux output = divided;
104         (0 << 6) + // aux out enable + aux output power
           = {-4, -1, 2, 5dbm}
105         (data->rftenable << 5) + // RF OUTPUT ENABLED
106         (data->rflPower << 3) + // RF output power = 5dbm
107         4; // register select
108     byte r4Ary[] = { lowByte(int_r4 >> 24), lowByte(int_r4 >>
           16), lowByte(int_r4 >> 8), lowByte(int_r4) };
109     memcpy(&data->reg[4], &r4Ary, sizeof(r4Ary));
110
111     int_r5 = (1 << 22) + (3 << 19) + 5; // lock detect pin
           mode = digital lock detect
112     byte r5Ary[] = { lowByte(int_r5 >> 24), lowByte(int_r5 >>
           16), lowByte(int_r5 >> 8), lowByte(int_r5) };
113     memcpy(&data->reg[5], &r5Ary, sizeof(r5Ary));
114
115     SPI.beginTransaction(SPI_Settings(2000000, MSBFIRST,
           SPI_MODE0));
116
117     unsigned int reg12[6];
118
119     reg12[0]=0x500000;
120     reg12[1]=0x8011;
121     reg12[2]=0x1008F42;
122     reg12[3]=0x84B3;
123     reg12[4]=0x9C803C;
124     reg12[5]=0x580005;
125
126     // write the registers
127     for (int j = 5; j >= 0 ; j--) { // Order from R5 to R1
128         digitalWrite(PLL_LEpin, LOW);
129         // Writes the data
130         for (int i = 0; i < 4 ; i++) {
131             SPI.transfer(data->reg[j][i]);
132         }
133         digitalWrite(PLL_LEpin, HIGH);
134     }
135 }
136
137 void updateamplitude() {
138     if (data->Amplitude_prev != data->Amplitude) {
139         analogWrite(A14, data->Amplitude ); // Attenuation
           control

```

```

140 }
141 data->Amplitude_prev = data->Amplitude;
142 }
143
144 void updatedelay() {
145     if (data->Delay_prev != data->Delay) {
146         unsigned int temp = data->Delay / 10;
147         digitalWriteFast(D0, HIGH && (temp & 0x001));
148         digitalWriteFast(D1, HIGH && (temp & 0x002));
149         digitalWriteFast(D2, HIGH && (temp & 0x004));
150         digitalWriteFast(D3, HIGH && (temp & 0x008));
151         digitalWriteFast(D4, HIGH && (temp & 0x010));
152         digitalWriteFast(D5, HIGH && (temp & 0x020));
153         digitalWriteFast(D6, HIGH && (temp & 0x040));
154         digitalWriteFast(D7, HIGH && (temp & 0x080));
155         digitalWriteFast(D8, HIGH && (temp & 0x100));
156         digitalWriteFast(D9, HIGH && (temp & 0x200)); // Phase
            control
157         digitalWriteFast(D10, LOW); // Cascading latch
158     }
159     data->Delay_prev = data->Delay;
160 }
161
162 void initializeDAC() {
163     unsigned long int_com0;
164
165     int_com0 = (7 << 19) + // update ref
166               1; // ref on
167     byte com0Ary[] = { lowByte(int_com0 >> 16), lowByte(
        int_com0 >> 8), lowByte(int_com0) };
168     memcpy(&data->comm[0], &com0Ary, sizeof(com0Ary));
169     SPI.beginTransaction(SPISettings(16000000, MSBFIRST,
        SPI_MODE2));
170     digitalWrite(DAC_LEpin, LOW);
171     for (int i = 0; i < 3 ; i++) {
172         SPI.transfer(data->comm[0][i]);
173     }
174     digitalWrite(DAC_LEpin, HIGH);
175 }
176
177 void updateDAC(int number) {
178     unsigned long int_com1, int_com2;
179
180     int_com1 = (3 << 19) + // update DAC1
181               (0 << 16) + // DAC1 address

```

```

182         data->Threshold_1; // Data threshold
183
184     byte com1Ary[] = { lowByte(int_com1 >> 16), lowByte(
        int_com1 >> 8), lowByte(int_com1) };
185     memcpy(&data->comm[1], &com1Ary, sizeof(com1Ary));
186
187     int_com2 = (3 << 19) + // update DAC2
188         (1 << 16) + //DAC2 address
189         data->Threshold_2; //Data threshold
190     byte com2Ary[] = { lowByte(int_com2 >> 16), lowByte(
        int_com2 >> 8), lowByte(int_com2) };
191     memcpy(&data->comm[2], &com2Ary, sizeof(com2Ary));
192
193
194     if (number == 1) {
195         if (data->Threshold_1_prev != data->Threshold_1) {
196             // Writes the data
197             SPI.beginTransaction(SPISettings(16000000, MSBFIRST,
                SPI_MODE2));
198             digitalWrite(DAC_LEpin, LOW);
199             for (int i = 0; i < 3 ; i++) {
200                 SPI.transfer(data->comm[1][i]);
201             }
202             digitalWrite(DAC_LEpin, HIGH);
203         }
204         data->Threshold_1_prev = data->Threshold_1;
205     }
206     else if (number == 2) {
207         if (data->Threshold_2_prev != data->Threshold_2) {
208             SPI.beginTransaction(SPISettings(16000000, MSBFIRST,
                SPI_MODE2));
209             digitalWrite(DAC_LEpin, LOW);
210             for (int i = 0; i < 3 ; i++) {
211                 SPI.transfer(data->comm[2][i]);
212             }
213             digitalWrite(DAC_LEpin, HIGH);
214         }
215         data->Threshold_2_prev = data->Threshold_2;
216     }
217
218 }
219
220
221 void setup() {
222     data = new Data();

```

```

223  Serial.begin(9600);
224  analogWriteResolution(12);
225  //pinMode(A14, OUTPUT);
226  pinMode(16, OUTPUT); //D0
227  pinMode(9, OUTPUT); //D1
228  pinMode(8, OUTPUT); //D2
229  pinMode(7, OUTPUT); //D3
230  pinMode(6, OUTPUT); //D4
231  pinMode(5, OUTPUT); //D5
232  pinMode(4, OUTPUT); //D6
233  pinMode(3, OUTPUT); //D7
234  pinMode(2, OUTPUT); //D8
235  pinMode(1, OUTPUT); //D9
236  pinMode(0, OUTPUT); //D10
237  pinMode(10, OUTPUT); //PLL LE
238  pinMode(15, OUTPUT); //DAC LE
239  digitalWrite(PLL_LEpin, HIGH);
240  digitalWrite(DAC_LEpin, HIGH);
241  SPI.begin();
242  initializeDAC();
243  updateDAC(1);
244  updateDAC(2);
245  updatePLL();
246  updatedelay();
247  updateamplitude();
248
249 }
250
251 void loop() {
252   char controlByte;
253   int tmpamp, tmpdly, tmpthr1, tmpthr2, tmpPLL[5]; // temp
        variables
254   byte temp1, temp2 , temp[12];
255   while (Serial.available() < 2) {};
256   controlByte = Serial.read();
257   switch (controlByte) {
258     case 0://Amp
259     {
260       temp1 = Serial.read();
261       temp2 = Serial.read();
262       tmpamp = temp2 << 8 | temp1;
263       memcpy(&data->Amplitude, &tmpamp, sizeof(tmpamp));
264       updateamplitude();
265     }
266     break;

```

```

267     case 1://Delay
268     {
269         temp1 = Serial.read();
270         temp2 = Serial.read();
271         tmpdly = temp2 << 8 | temp1;
272         memcpy(&data->Delay, &tmpdly, sizeof(tmpdly));
273         updatedelay();
274     }
275     break;
276     case 2://Threshold 1
277     {
278         temp1 = Serial.read();
279         temp2 = Serial.read();
280         tmpthr1 = temp2 << 8 | temp1;
281         memcpy(&data->Threshold_1, &tmpthr1, sizeof(tmpthr1
282             ));
283         updateDAC(1);
284     }
285     break;
286     case 3://Threshold 2
287     {
288         temp1 = Serial.read();
289         temp2 = Serial.read();
290         tmpthr2 = temp2 << 8 | temp1;
291         memcpy(&data->Threshold_2, &tmpthr2, sizeof(tmpthr2
292             ));
293         updateDAC(2);
294     }
295     break;
296     case 4:// PLL setttings
297     {
298         for (int i = 0; i < 12; i++) {
299             temp[i] = Serial.read();
300         }
301         tmpPLL[0] = temp[3] << 8 | temp[2]; //Frequency
302         tmpPLL[1] = temp[5] << 8 | temp[4]; //rfPower
303         tmpPLL[2] = temp[7] << 8 | temp[6]; //
304         ChargepumpCurr
305         tmpPLL[3] = temp[9] << 8 | temp[8]; //integer
306         tmpPLL[4] = temp[11] << 8 | temp[10]; //integer
307         //update the data structure
308         memcpy(&data->rflenable, &temp[0], sizeof(temp[0]));
309         memcpy(&data->refby2, &temp[1], sizeof(temp[1]));
310         memcpy(&data->Frequency, &tmpPLL[0], sizeof(tmpPLL
311             [0]));

```

```

308     memcpy(&data->rfPower, &tmpPLL[1], sizeof(tmpPLL
        [1]));
309     memcpy(&data->ChargepumpCurr, &tmpPLL[2], sizeof(
        tmpPLL[2]));
310     memcpy(&data->integer, &tmpPLL[3], sizeof(tmpPLL
        [3]));
311     memcpy(&data->RFdivider, &tmpPLL[4], sizeof(tmpPLL
        [4]));
312
313     updatePLL();
314 }
315     break;
316 default:
317     break;
318 }
319
320     delay(100);
321
322 }

```



## Bibliography

- [1] K V Klitzing, Gerhard Dorda, and Michael Pepper. New method for high-accuracy determination of the fine-structure constant based on quantized hall resistance. *Phys. Rev. Lett.*, 45(6):494, 1980.
- [2] Mahito Kohmoto. Topological invariant and the quantization of the hall conductance. *Annals of Physics*, 160(2):343–354, 1985.
- [3] David J Thouless, Mahito Kohmoto, M Peter Nightingale, and Md den Nijs. Quantized hall conductance in a two-dimensional periodic potential. *Physical review letters*, 49(6):405, 1982.
- [4] Zheng Wang, Yidong Chong, John D Joannopoulos, and Marin Soljačić. Observation of unidirectional backscattering-immune topological electromagnetic states. *Nature*, 461(7265):772, 2009.
- [5] Mohammad Hafezi, Eugene A Demler, Mikhail D Lukin, and Jacob M Taylor. Robust optical delay lines with topological protection. *Nature Physics*, 7(11):907, 2011.
- [6] RO Umucalılar and I Carusotto. Artificial gauge field for photons in coupled cavity arrays. *Phys. Rev. A*, 84(4):043804, 2011.
- [7] Takuya Kitagawa, Erez Berg, Mark Rudner, and Eugene Demler. Topological characterization of periodically driven quantum systems. *Phys. Rev. B*, 82(23):235114, 2010.
- [8] Netanel H Lindner, Gil Refael, and Victor Galitski. Floquet topological insulator in semiconductor quantum wells. *Nature Physics*, 7(6):490, 2011.
- [9] Mohammad Hafezi, S Mittal, J Fan, A Migdall, and JM Taylor. Imaging topological edge states in silicon photonics. *Nature Photonics*, 7(12):1001, 2013.
- [10] Mikael C Rechtsman, Julia M Zeuner, Yonatan Plotnik, Yaakov Lumer, Daniel Podolsky, Felix Dreisow, Stefan Nolte, Mordechai Segev, and Alexander Szameit. Photonic floquet topological insulators. *Nature*, 496(7444):196, 2013.
- [11] Ling Lu, John D Joannopoulos, and Marin Soljačić. Topological photonics. *Nature Photonics*, 8(11):821, 2014.

- [12] Alexander B Khanikaev and Gennady Shvets. Two-dimensional topological photonics. *Nature Photonics*, 11(12):763, 2017.
- [13] Tomoki Ozawa, Hannah M Price, Alberto Amo, Nathan Goldman, Mohammad Hafezi, Ling Lu, Mikael C Rechtsman, David Schuster, Jonathan Simon, Oded Zilberberg, et al. Topological photonics. *Reviews of Modern Physics*, 91(1):015006, 2019.
- [14] S. Mittal, J. Fan, S. Faez, A. Migdall, J. M. Taylor, and M. Hafezi. Topologically robust transport of photons in a synthetic gauge field. *Phys. Rev. Lett.*, 113(8):087403, 2014.
- [15] P St-Jean, V Goblot, E Galopin, A Lemaître, T Ozawa, L Le Gratiet, I Sagnes, J Bloch, and A Amo. Lasing in topological edge states of a one-dimensional lattice. *Nat. Photonics*, 11(10):651–656, 2017.
- [16] Babak Bahari, Abdoulaye Ndao, Felipe Vallini, Abdelkrim El Amili, Yeshaiahu Fainman, and Boubacar Kanté. Nonreciprocal lasing in topological cavities of arbitrary geometries. *Science*, 358(6363):636–640, November 2017.
- [17] Miguel A Bandres, Steffen Wittek, Gal Harari, Midya Parto, Jinhan Ren, Mordechai Segev, Demetrios N Christodoulides, and Mercedeh Khajavikhan. Topological insulator laser: Experiments. *Science*, 359(6381):eaar4005, 2018.
- [18] Sunil Mittal, Elizabeth A Goldschmidt, and Mohammad Hafezi. A topological source of quantum light. *Nature*, 561(7724):502, 2018.
- [19] Venkata Vikram Orre\*, Sunil Mittal\*, Elizabeth A. Goldschmidt, and Mohammad Hafezi. Tunable quantum interference using a topological source of indistinguishable photon pairs. *manuscript in progress*, 2020.
- [20] Xiaojun Cheng, Camille Jouvaud, Xiang Ni, S. Hossein Mousavi, Azriel Z. Genack, and Alexander B. Khanikaev. Robust reconfigurable electromagnetic pathways within a photonic topological insulator. *Nature Mater.*, 15(5):542–548, 2016.
- [21] Han Zhao, Xingdu Qiao, Tianwei Wu, Bikashkali Midya, Stefano Longhi, and Liang Feng. Non-hermitian topological light steering. *Science*, 365(6458):1163–1166, 2019.
- [22] F Duncan M Haldane. Model for a quantum hall effect without landau levels: Condensed-matter realization of the” parity anomaly”. *Phys. Rev. Lett.*, 61(18):2015, 1988.
- [23] Charles L Kane and Eugene J Mele. Quantum spin hall effect in graphene. *Phys. Rev. Lett.*, 95(22):226801, 2005.

- [24] Sunil Mittal, Venkata Vikram Orre, Daniel Leykam, Y. D. Chong, and Mohammad Hafezi. Photonic anomalous quantum hall effect. *Phys. Rev. Lett.*, 123:043201, Jul 2019.
- [25] Daniel Leykam, S Mittal, M Hafezi, and Yi Dong Chong. Reconfigurable topological phases in next-nearest-neighbor coupled resonator lattices. *Phys. Rev. Lett.*, 121(2):023901, 2018.
- [26] Sunil Mittal, Sriram Ganeshan, Jingyun Fan, Abolhassan Vaezi, and Mohammad Hafezi. Measurement of topological invariants in a 2d photonic system. *Nature Photonics*, 10(3):180, 2016.
- [27] Graham T Reed, G Mashanovich, F Yand Gardes, and DJ Thomson. Silicon optical modulators. *Nature photonics*, 4(8):518, 2010.
- [28] Jonathan P. Dowling. Quantum optical metrology – the lowdown on high-n00n states. *Contemporary Physics*, 49(2):125–143, 2008.
- [29] Yonatan Israel, Shamir Rosen, and Yaron Silberberg. Supersensitive polarization microscopy using noon states of light. *Phys. Rev. Lett.*, 112(10):103604, 2014.
- [30] Dik Bouwmeester, Jian-Wei Pan, Klaus Mattle, Manfred Eibl, Harald Weinfurter, and Anton Zeilinger. Experimental quantum teleportation. *Nature*, 390:575–579, Dec 1997.
- [31] SA Castelletto and RE Scholten. Heralded single photon sources: a route towards quantum communication technology and photon standards. *The European Physical Journal-Applied Physics*, 41(3):181–194, 2008.
- [32] Keith R. Motes, Alexei Gilchrist, Jonathan P. Dowling, and Peter P. Rohde. Scalable boson sampling with time-bin encoding using a loop-based architecture. *Phys. Rev. Lett.*, 113:120501, Sep 2014.
- [33] Nicolò Spagnolo, Chiara Vitelli, Marco Bentivegna, Daniel J. Brod, Andrea Crespi, Fulvio Flamini, Sandro Giacomini, Giorgio Milani, Roberta Ramponi, Paolo Mataloni, Roberto Osellame, Ernesto F. Galvão, and Fabio Sciarrino. Experimental validation of photonic boson sampling. *Nature Photonics*, 8:615–620, Jun 2014.
- [34] Jean-Luc Tambasco, Giacomo Corrielli, Robert J. Chapman, Andrea Crespi, Oded Zilberberg, Roberto Osellame, and Alberto Peruzzo. Quantum interference of topological states of light. *Science Advances*, 4(9), 2018.
- [35] Andrea Blanco-Redondo, Bryn Bell, Dikla Oren, Benjamin J. Eggleton, and Mordechai Segev. Topological protection of biphoton states. *Science*, 362(6414):568–571, 2018.

- [36] Matthew D Eisaman, Jingyun Fan, Alan Migdall, and Sergey V Polyakov. Invited review article: Single-photon sources and detectors. *Review of scientific instruments*, 82(7):071101, 2011.
- [37] Georg Harder and et.al. An optimized photon pair source for quantum circuits. *Opt. Express*, 21(12):13975–13985, Jun 2013.
- [38] Christoph Simon, Hugues De Riedmatten, Mikael Afzelius, Nicolas Sangouard, Hugo Zbinden, and Nicolas Gisin. Quantum repeaters with photon pair sources and multimode memories. *Physical review letters*, 98(19):190503, 2007.
- [39] Vittorio Giovannetti, Seth Lloyd, and Lorenzo Maccone. Quantum-enhanced positioning and clock synchronization. *Nature*, 412:417–419, 2001.
- [40] Offir Cohen, Jeff S. Lundeen, Brian J. Smith, Graciana Puentes, Peter J. Mosley, and Ian A. Walmsley. Tailored photon-pair generation in optical fibers. *Phys. Rev. Lett.*, 102:123603, Mar 2009.
- [41] Jun Chen, Kim Fook Lee, and Prem Kumar. Deterministic quantum splitter based on time-reversed hong-ou-mandel interference. *Phys. Rev. A*, 76:031804, Sep 2007.
- [42] Joshua W Silverstone, Damien Bonneau, Kazuya Ohira, Nob Suzuki, Haruhiko Yoshida, Norio Iizuka, Mizunori Ezaki, Chandra M Natarajan, Michael G Tanner, Robert H Hadfield, et al. On-chip quantum interference between silicon photon-pair sources. *Nature Photonics*, 8(2):104, 2014.
- [43] Jiakun He, Bryn A. Bell, Alvaro Casas-Bedoya, Yanbing Zhang, Alex S. Clark, Chunle Xiong, and Benjamin J. Eggleton. Ultracompact quantum splitter of degenerate photon pairs. *Optica*, 2(9):779–782, Sep 2015.
- [44] Vittorio Peano, Martin Houde, Florian Marquardt, and Aashish A. Clerk. Topological Quantum Fluctuations and Traveling Wave Amplifiers. *Phys. Rev. X*, 6:041026, 2016.
- [45] T. Shi, H. J. Kimble, and J. I. Cirac. Topological phenomena in classical optical networks. *Proceedings of the National Academy of Sciences*, 114(43):E8967–E8976, 2017.
- [46] CW Gardiner and MJ Collett. Input and output in damped quantum systems: Quantum stochastic differential equations and the master equation. *Phys. Rev. A*, 31(6):3761, 1985.
- [47] C. K. Hong, Z. Y. Ou, and L. Mandel. Measurement of subpicosecond time intervals between two photons by interference. *Phys. Rev. Lett.*, 59:2044–2046, Nov 1987.
- [48] Marek Żukowski and Jarosław Pykacz. Bell’s theorem: Proposition of realizable experiment using linear momenta. *Physics Letters A*, 127(1):1–4, 1988.

- [49] J. D. Franson. Bell inequality for position and time. *Phys. Rev. Lett.*, 62:2205–2208, May 1989.
- [50] JD Franson. Two-photon interferometry over large distances. *Phys. Rev. A*, 44(7):4552, 1991.
- [51] J. Brendel, E. Mohler, and W. Martienssen. Time-resolved dual-beam two-photon interferences with high visibility. *Phys. Rev. Lett.*, 66:1142–1145, Mar 1991.
- [52] Chaoxuan Ma, Xiaoxi Wang, Vikas Anant, Andrew D. Beyer, Matthew D. Shaw, and Shayan Mookherjea. Silicon photonic entangled photon-pair and heralded single photon generation with  $\text{car} > 12,000$  and  $g(2)(0) < 0.006$ . *Opt. Express*, 25(26):32995–33006, Dec 2017.
- [53] Sunil Mittal. *Topological edge states in silicon photonics*. PhD thesis, University of Maryland, 2014.
- [54] Sunil Mittal, Venkata Vikram Orre, and Mohammad Hafezi. Topologically robust transport of entangled photons in a 2d photonic system. *Optics express*, 24(14):15631–15641, 2016.
- [55] Nicolas Gisin and Rob Thew. Quantum communication. *Nature photonics*, 1(3):165, 2007.
- [56] Jian-Wei Pan, Zeng-Bing Chen, Chao-Yang Lu, Harald Weinfurter, Anton Zeilinger, and Marek Żukowski. Multiphoton entanglement and interferometry. *Rev. Mod. Phys.*, 84:777–838, May 2012.
- [57] Brian H Kolner. Space-time duality and the theory of temporal imaging. *IEEE Journal of Quantum Electronics*, 30(8):1951–1963, 1994.
- [58] John M Donohue, Morgan Mastrovich, and Kevin J Resch. Spectrally engineering photonic entanglement with a time lens. *Phys. Rev. Lett.*, 117(24):243602, 2016.
- [59] Jonathan Lavoie, John M Donohue, Logan G Wright, Alessandro Fedrizzi, and Kevin J Resch. Spectral compression of single photons. *Nature Photonics*, 7(5):363, 2013.
- [60] Onur Kuzucu, Franco NC Wong, Sunao Kurimura, and Sergey Tsvetkov. Joint temporal density measurements for two-photon state characterization. *Phys. Rev. Lett.*, 101(15):153602, 2008.
- [61] Chinmay Belthangady, Shengwang Du, Chih-Sung Chu, Guang-Yu Yin, and Stephen E Harris. Modulation and measurement of time-energy entangled photons. *Phys. Rev. A*, 80(3):031803, 2009.

- [62] Sunil Mittal, Venkata Vikram Orre, Alessandro Restelli, Reza Salem, Elizabeth A. Goldschmidt, and Mohammad Hafezi. Temporal and spectral manipulations of correlated photons using a time lens. *Phys. Rev. A*, 96:043807, Oct 2017.
- [63] S. Ramelow, L. Ratschbacher, A. Fedrizzi, N. K. Langford, and A. Zeilinger. Discrete tunable color entanglement. *Phys. Rev. Lett.*, 103:253601, Dec 2009.
- [64] Andreas Schreiber, Aurél Gábris, Peter P Rohde, Kaisa Laiho, Martin Štefaňák, Václav Potoček, Craig Hamilton, Igor Jex, and Christine Silberhorn. A 2d quantum walk simulation of two-particle dynamics. *Science*, 336(6077):55–58, 2012.
- [65] Yu He, X Ding, Z-E Su, H-L Huang, J Qin, C Wang, S Unsleber, C Chen, H Wang, Y-M He, et al. Time-bin-encoded boson sampling with a single-photon device. *Phys. Rev. Lett.*, 118(19):190501, 2017.
- [66] Mihir Pant and Dirk Englund. High-dimensional unitary transformations and boson sampling on temporal modes using dispersive optics. *Phys. Rev. A*, 93:043803, Apr 2016.
- [67] E. Knill, R. Laflamme, and G. J. Milburn. A scheme for efficient quantum computation with linear optics. *Nature*, 409:46–52, Jan 2001.
- [68] Jacques Carolan, Christopher Harrold, Chris Sparrow, Enrique Martín-López, Nicholas J. Russell, Joshua W. Silverstone, Peter J. Shadbolt, Nobuyuki Matsuda, Manabu Oguma, Mikitaka Itoh, Graham D. Marshall, Mark G. Thompson, Jonathan C. F. Matthews, Toshikazu Hashimoto, Jeremy L. O’Brien, and Anthony Laing. Universal linear optics. *Science*, 349(6249):711–716, 2015.
- [69] T. D. Ladd, F. Jelezko, R. Laflamme, Y. Nakamura, C. Monroe, and J. L. O’Brien. Quantum computers. *Nature*, 464:45–53, Mar 2010.
- [70] Klaus Mattle, Harald Weinfurter, Paul G. Kwiat, and Anton Zeilinger. Dense coding in experimental quantum communication. *Phys. Rev. Lett.*, 76:4656–4659, Jun 1996.
- [71] Hoi-Kwong Lo, Marcos Curty, and Kiyoshi Tamaki. Secure quantum key distribution. *Nature Photonics*, 8:595–604, Jul 2014.
- [72] Gabriela Barreto Lemos, Victoria Borish, Garrett D. Cole, Sven Ramelow, Radek Lapkiewicz, and Anton Zeilinger. Quantum imaging with undetected photons. *Nature*, 512:409–412, Aug 2014.
- [73] Scott Aaronson and Alex Arkhipov. The computational complexity of linear optics. *Theory of Computing*, 9(4):143–252, 2013.

- [74] Y. H. Shih and C. O. Alley. New type of einstein-podolsky-rosen-bohm experiment using pairs of light quanta produced by optical parametric down conversion. *Phys. Rev. Lett.*, 61:2921–2924, Dec 1988.
- [75] T. Legero, T. Wilk, A. Kuhn, and G. Rempe. Time-resolved two-photon quantum interference. *Applied Physics B*, 77(8):797–802, Dec 2003.
- [76] Thomas Legero, Tatjana Wilk, Markus Hennrich, Gerhard Rempe, and Axel Kuhn. Quantum beat of two single photons. *Phys. Rev. Lett.*, 93:070503, Aug 2004.
- [77] Tian-Ming Zhao, Han Zhang, Jian Yang, Zi-Ru Sang, Xiao Jiang, Xiao-Hui Bao, and Jian-Wei Pan. Entangling different-color photons via time-resolved measurement and active feed forward. *Phys. Rev. Lett.*, 112:103602, Mar 2014.
- [78] G. Vittorini, D. Hucul, I. V. Inlek, C. Crocker, and C. Monroe. Entanglement of distinguishable quantum memories. *Phys. Rev. A*, 90:040302, Oct 2014.
- [79] Vincenzo Tamma and Simon Laibacher. Multiboson correlation interferometry with arbitrary single-photon pure states. *Phys. Rev. Lett.*, 114:243601, Jun 2015.
- [80] Simon Laibacher and Vincenzo Tamma. Symmetries and entanglement features of inner-mode-resolved correlations of interfering nonidentical photons. *Phys. Rev. A*, 98:053829, Nov 2018.
- [81] Xu-Jie Wang, Bo Jing, Peng-Fei Sun, Chao-Wei Yang, Yong Yu, Vincenzo Tamma, Xiao-Hui Bao, and Jian-Wei Pan. Experimental time-resolved interference with multiple photons of different colors. *Phys. Rev. Lett.*, 121:080501, Aug 2018.
- [82] T. Gerrits, F. Marsili, V. B. Verma, L. K. Shalm, M. Shaw, R. P. Mirin, and S. W. Nam. Spectral correlation measurements at the hong-ou-mandel interference dip. *Phys. Rev. A*, 91:013830, Jan 2015.
- [83] Rui-Bo Jin, Thomas Gerrits, Mikio Fujiwara, Ryota Wakabayashi, Taro Yamashita, Shigehito Miki, Hirotaka Terai, Ryosuke Shimizu, Masahiro Takeoka, and Masahide Sasaki. Spectrally resolved hong-ou-mandel interference between independent photon sources. *Opt. Express*, 23(22):28836–28848, Nov 2015.
- [84] Simon Laibacher and Vincenzo Tamma. From the physics to the computational complexity of multiboson correlation interference. *Phys. Rev. Lett.*, 115:243605, Dec 2015.
- [85] Vincenzo Tamma and Simon Laibacher. Multi-boson correlation sampling. *Quantum Information Processing*, 15(3):1241–1262, Mar 2016.

- [86] Vincenzo Tamma and Simon Laibacher. Boson sampling with non-identical single photons. *Journal of Modern Optics*, 63(1):41–45, 2016.
- [87] Simon Laibacher and Vincenzo Tamma. Toward quantum computational supremacy of boson sampling with random overlap in the photonic spectra. *arXiv:1801.03832*, 2018.
- [88] Venkata Vikram Orre, Elizabeth A. Goldschmidt, Abhinav Deshpande, Alexey V. Gorshkov, Vincenzo Tamma, Mohammad Hafezi, and Sunil Mittal. Interference of temporally distinguishable photons using frequency-resolved detection. *Phys. Rev. Lett.*, 123:123603, Sep 2019.
- [89] W. P. Grice and I. A. Walmsley. Spectral information and distinguishability in type-ii down-conversion with a broadband pump. *Phys. Rev. A*, 56:1627–1634, Aug 1997.
- [90] Malte Avenhaus, Andreas Eckstein, Peter J. Mosley, and Christine Silberhorn. Fiber-assisted single-photon spectrograph. *Opt. Lett.*, 34(18):2873–2875, Sep 2009.
- [91] Alex O. C. Davis, Paul M. Saulnier, Michał Karpiński, and Brian J. Smith. Pulsed single-photon spectrometer by frequency-to-time mapping using chirped fiber bragg gratings. *Opt. Express*, 25(11):12804–12811, May 2017.
- [92] Vittorio Giovannetti, Lorenzo Maccone, Jeffrey H. Shapiro, and Franco N. C. Wong. Extended phase-matching conditions for improved entanglement generation. *Phys. Rev. A*, 66:043813, Oct 2002.
- [93] Paulina S. Kuo, Thomas Gerrits, Varun B. Verma, and Sae Woo Nam. Spectral correlation and interference in non-degenerate photon pairs at telecom wavelengths. *Opt. Lett.*, 41(21):5074–5077, Nov 2016.
- [94] Sergei Slussarenko, Morgan M. Weston, Helen M. Chrzanowski, Lynden K. Shalm, Varun B Verma, Sae Woo Nam, and Geoff J. Pryde. Measurement of subpicosecond time intervals between two photons by interference. *Nature Photonics*, 11:700–703, Nov 2017.
- [95] Abhinav Deshpande, Bill Fefferman, Minh C. Tran, Michael Foss-Feig, and Alexey V. Gorshkov. Dynamical phase transitions in sampling complexity. *Phys. Rev. Lett.*, 121:030501, Jul 2018.
- [96] Dikla Oren, Maor Mutzafi, Yonina C. Eldar, and Mordechai Segev. Quantum state tomography with a single measurement setup. *Optica*, 4(8):993–999, Aug 2017.
- [97] Kai Wang, Sergey V. Suchkov, James G. Titchener, Alexander Szameit, and Andrey A. Sukhorukov. Inline detection and reconstruction of multiphoton quantum states. *Optica*, 6(1):41–44, Jan 2019.



- [98] David C Burnham and Donald L Weinberg. Observation of simultaneity in parametric production of optical photon pairs. *Phys. Rev. Lett.*, 25(2):84, 1970.
- [99] Timothy E Keller and Morton H Rubin. Theory of two-photon entanglement for spontaneous parametric down-conversion driven by a narrow pump pulse. *Phys. Rev. A*, 56(2):1534, 1997.
- [100] MV Fedorov, Yu M Mikhailova, and PA Volkov. Gaussian modelling and schmidt modes of spdc biphoton states. *Journal of Physics B: Atomic, Molecular and Optical Physics*, 42(17):175503, 2009.
- [101] GD Boyd and DA Kleinman. Parametric interaction of focused gaussian light beams. *Journal of Applied Physics*, 39(8):3597–3639, 1968.
- [102] Alessandro Fedrizzi, Thomas Herbst, Andreas Poppe, Thomas Jennewein, and Anton Zeilinger. A wavelength-tunable fiber-coupled source of narrowband entangled photons. *Optics Express*, 15(23):15377–15386, 2007.